

# **Running-in of Rolling-sliding Contacts**

**Rifky Ismail**

De promotiecommissie is als volgt samengesteld:

prof.dr. G.P.M.R. Dewulf	Universiteit Twente	voorzitter en secretaris
prof.dr.ir. D.J. Schipper	Universiteit Twente	Promotor
dr. ir. J. Jamari	University of Diponegoro	Assistent-Promotor
prof.dr.ir. L.A.M. van Dongen	Universiteit Twente	
prof.dr.ir. T. Tinga	Universiteit Twente	
prof.dr.ir. P. De Baets	University of Gent, Belgie	
prof.dr.ir. R.P.B.J. Dollevoet	Technische Universiteit Delft	

RUNNING-IN OF ROLLING-SLIDING CONTACTS

Ismail, Rifky

Ph.D. Thesis, University of Twente, Enschede, the Netherlands,  
November 2013

ISBN: 978-90-365-1887-1

Keywords: rolling-sliding, contacts, stress, wear, FEM

Printed by Ipskamp Drukkers B.V., Enschede, the Netherlands

Copyright © R. Ismail, Enschede, the Netherlands

All rights reserved

# RUNNING-IN OF ROLLING-SLIDING CONTACTS

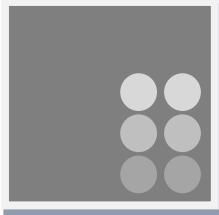
## PROEFSCHRIFT

ter verkrijging van  
de graad van doctor aan de Universiteit Twente,  
op gezag van de rector magnificus,  
prof.dr. H. Brinksma,  
volgens besluit van het College voor Promoties  
in het openbaar te verdedigen  
op woensdag 6 november 2013 om 14.45 uur

door

Rifky Ismail  
geboren op 16 juli 1980  
te Semarang, Indonesia

Dit proefschrift is goedgekeurd door:  
de promotor: prof.dr.ir. D.J. Schipper  
de assistent-promotor: dr.ir. J. Jamari



## Summary

Running-in of two fresh and unworn surfaces in contact is a transient phase where friction and wear vary considerably in time. During running-in the surface properties of the components are adjusted. If the initial surface roughness of the rubbing surfaces is correctly chosen, the running-in changes into the steady-state phase. At this stage, the rubbing surfaces are in general smoother and their wear rate is low and constant. On the other hand, an inappropriate choice of roughness may lead to a rapid deterioration of the rubbing surfaces. The micro-geometry of the surface is an important factor in determining the life of mechanical components. During the running-in phase, the highest asperities are “flattened”, thereby increasing the number of asperities in contact and, as a result, increasing the load-carrying capacity of the surface.

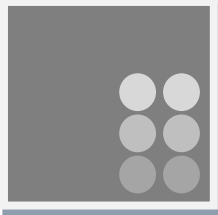
Fundamental studies that attempt to consider the details of running-in phenomena are relatively rare. This research is conducted with the aim of exploring the running-in phase for the rolling, sliding and rolling-sliding contact. Finite element simulations are conducted to calculate the stress distributions for the three types of contact motions during the running-in phase. The evolution of the contact pressure for a certain rolling or sliding distance is studied to unravel the running-in phase.

During running-in of rolling contacts, the change in the surface topography results in the transformation from a rough surface to a smoother surface: the flattening of the high asperities induces a reduction in surface roughness. This flattening of asperities is due to plastic deformation and causes a higher equivalent residual stress at the surface. The transition of the running-in phase to the steady-state phase of a rolling contact is governed by the transition of plastic to elastic deformation on roughness level.

In sliding contacts, the proposed finite element (FE) model combined with the Archard wear equation successfully predicts the contact pressure evolution and change in the topography on a macroscopic point of view. The change in the topography in a sliding contact is mainly caused by wear. A new FE model, with respect to the artificial and real surface roughness, is discussed. It is found that the proposed model is a useful tool to study the running-in of a surface on roughness level.

The changes on macroscopic and on microscopic level of the surface are also discussed in the running-in of rolling-sliding contacts considering two aspects: wear and plastic deformation. The geometrical change of the contacting surface due to wear is predicted using the present FEM model, combined with the Archard wear equation, and has been compared with results from the literature. Calculations are performed to predict the wear of an artificial rough hemisphere in rolling-sliding contact with a smooth cylinder. The model also predicts the change of real rough surfaces which were in good agreement with the experimental results. The change of a rough surface, represented by an arithmetic average surface roughness,  $R_a$ , is predicted for lubricated rolling-sliding contacts using the load-sharing concept. The results obtained are in good agreement with experimental results.

A FEM based model has been developed to study the running-in of rolling, sliding and rolling-sliding contacts on macroscopic level as well as on roughness level. However, the transition between the running-in phase and the steady-state phase for sliding and rolling-sliding contacts cannot be determined by considering only one single parameter; likewise for the rolling contact situation. Wear is an ongoing process.



## Samenvatting

---

Inlopen van twee nieuwe in contact zijnde oppervlakken komt tot uiting in een aanzienlijke verandering in het wrijvings- en slijtagegedrag als gevolg van veranderingen in de micro-geometrie. Als de initiële oppervlakteruwheid correct wordt gekozen zal de inloofase overgaan in een steady-state fase. In deze situatie is in het algemeen de oppervlakteruwheid lager en is de specifieke slijtagegraad lager en constant in de tijd. Als een verkeerde oppervlakteruwheid wordt gekozen leidt dit tot een snelle achteruitgang en verruwing van de oppervlakken. De micro-geometrie van een oppervlak blijkt een belangrijke factor te zijn die de levensduur van mechanische componenten bepaalt. Tijdens het inlopen worden de hoogste ruwheden afgevlakt met als gevolg dat de hoeveelheid in contact zijnde ruwheden toeneemt. Het resultaat is een hoger draagvermogen van de oppervlakken.

Er is niet veel fundamenteel onderzoek uitgevoerd met betrekking tot het inloopp proces. Dit onderzoek is uitgevoerd met als doel om het inlopen van een rollend, glijdend of het rollend/glijdend contact te verkennen. Hiertoe zijn eindige elementen simulaties uitgevoerd om de optredende spanningen in dergelijke contacten tijdens het inlopen te berekenen voor drie typen beweging in het contact. De evolutie van de contactdruk voor een bepaalde rol- of glijafstand is bestudeerd met als doel om het inloopgedrag te analyseren.

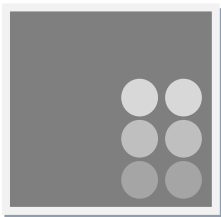
Tijdens het inlopen van rollende contacten verandert de micro-geometrie van het oppervlak van een ruw oppervlak naar een gladder oppervlak, de afvlakking van de ruwheden resulteert in een lagere ruwheid. Deze afvlakking is het gevolg van plastische deformatie heeft een hogere restspanning in het oppervlak tot gevolg. De overgang van de inloofase naar de steady-state fase bij rollend contact wordt bepaald door de overgang van plastische deformatie naar elastische deformatie op ruwheidsniveau.

Voor glijdende contacten wordt door gebruik te maken van het voorgestelde eindige elementen model, gecombineerd met de slijtage vergelijking van Archard, de ontwikkeling van de contactdruk en verandering van de macrogeometrie goed voorspeld. De verandering van de microgeometrie is hoofdzakelijk het gevolg van slijtage. Verder wordt er een nieuw eindige elementen model, voor zowel kunstmatige en gemeten oppervlakteruwheid, bediscussieerd. Uit de resultaten blijkt dat het model goed is te gebruiken om het inloopgedrag op ruwheidsniveau te bestuderen.

De veranderingen van het oppervlak ten gevolge van inlopen op macroscopisch en microscopisch niveau is bestudeerd voor de rollende-glijdende contact situatie, rekening houdend met slijtage en plastische deformatie. De geometrische veranderingen van het contact oppervlak als gevolg van slijtage is voorspeld met het eindige elementen model en de Archard slijtage wet. De resultaten zijn vervolgens vergeleken met resultaten uit de literatuur. Verder zijn er berekeningen uitgevoerd om de slijtage van een kunstmatig ruwe bol in rollend-glijdend contact met een gladde cilinder te voorspellen. Ook de veranderingen van ruwe oppervlakken zijn met het model voorspeld en de resultaten komen goed overeen met de experimentele resultaten. De veranderingen van de ruwheid, aangegeven met de gemiddelde ruwheid  $R_a$ , voor gesmeerde rollende-glijdende contacten, is uitgerekend. Hierbij is gebruik gemaakt van het concept dat de normaalbelasting deels gedragen wordt door de smeefilm en deels door de contact makende oppervlakken. De resultaten komen goed overeen met de experimentele resultaten.

Een op eindige elementen gebaseerd model is ontwikkeld om het inlopen van rollende, glijdende en rollende-glijdende contacten te bestuderen op macroscopisch en op microscopisch niveau. De overgang van inlopen naar de steady-state fase voor glijdende en rollende-glijdende contacten kan echter niet gevangen worden met een enkele parameter zoals bij de rollende contact situatie. Slijtage is een continue proces.





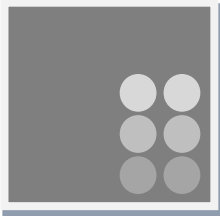
# Contents

<b>Summary</b>	<b>V</b>
<b>Samenvatting</b>	<b>VII</b>
<b>Contents</b>	<b>IX</b>
<b>Nomenclature</b>	<b>XII</b>
<b>1. Introduction</b>	<b>1</b>
1.1. Tribology .....	1
1.2. Running-in .....	2
1.2.1. The running-in to steady state phase .....	2
1.2.2. The effects of contact motion on running-in .....	3
1.2.3. Modelling the running-in phase. ....	4
1.3. The objective of this thesis .....	4
1.4. Outline.....	5
References .....	5
<b>2. Literature</b>	<b>7</b>
2.1. Introduction .....	7
2.2. Running-in .....	8
2.2.1. The definition of running-in.....	8
2.2.2. The significance of running-in .....	8
2.3. Rolling contact.....	10
2.3.1. The definition of a rolling contact.....	10
2.3.2. Rolling contact on a flat surface .....	11
2.3.3. Model of running-in of rolling contact on a rough surface .....	11
2.3.4. Experiments on the running-in of rolling contact .....	13
2.4. Sliding contact .....	15

2.4.1.	The definition of sliding contact .....	15
2.4.2.	General wear model of Archard .....	15
2.4.3.	Finite element based model .....	16
2.4.4.	Global increment wear model .....	17
2.4.5.	Models for running-in of sliding contacts .....	18
2.4.6.	Running-in of sliding contacts, some experiments .....	20
2.5.	Rolling-sliding contact.....	21
2.5.1.	The definition of rolling-sliding contact .....	21
2.5.2.	FEM based wear model on rolling-sliding contacts .....	21
2.5.3.	GIWM based wear model for rolling-sliding contact .....	23
2.5.4.	BEM wear model for a rolling-sliding contact .....	24
2.5.5.	Model for running-in of rolling-sliding contact .....	25
2.5.6.	Rolling-sliding running-in experiments .....	28
2.6.	Concluding Remarks .....	30
	References .....	32
<b>3.</b>	<b>Running-in of Rolling Contacts</b> .....	<b>37</b>
3.1.	Introduction .....	37
3.2.	Simulation of repeated static contact.....	38
3.2.1.	Single static contact model .....	38
3.2.2.	FE contact calculations .....	40
3.2.3.	Repeated static contact on a flat surface .....	44
3.3.	Running-in of a rigid cylinder rolling on a smooth flat surface .....	46
3.3.1.	Contact model and simulation procedures .....	46
3.3.2.	Validation of the FE simulation .....	48
3.3.3.	Results and discussions.....	49
3.4.	Running-in of a rigid cylinder rolling on a rough flat surface.....	52
3.4.1.	Contact model and simulation procedures .....	52
3.4.2.	Single rolling contact .....	54
3.4.3.	Running-in of rolling contact .....	55
3.5.	Running-in of a rigid ball rolling on a rough surface .....	67
3.5.1.	Contact model and simulation procedures .....	68
3.5.2.	Topographical change .....	70
3.5.3.	Stresses .....	71
3.5.4.	Plastic strain.....	74
3.5.5.	Validation of the FE simulation .....	77
3.6.	Concluding remarks .....	78
	References .....	79
<b>4.</b>	<b>Running-in of Sliding Contacts</b> .....	<b>83</b>
4.1.	Introduction .....	83
4.2.	Running-in of sliding contacts, macroscopic wear .....	84
4.2.1.	Simulation procedure .....	84
4.2.2.	Comparison of the model with literature .....	86

4.2.3. Present model simulations and experiments .....	88
4.3. Running-in of sliding rough surfaces, microscopic wear .....	92
4.3.1. Running-in of sliding artificial rough surfaces .....	92
4.3.2. Running-in of sliding real rough surfaces .....	98
4.4. Concluding remarks .....	104
References .....	104
<b>5. Running-in of Rolling-sliding Contacts</b> .....	<b>107</b>
5.1. Introduction .....	107
5.2. Modelling wear in rolling-sliding contacts: a comparison .....	108
5.2.1. Analytical model .....	108
5.2.2. Finite element simulation .....	114
5.3. Running-in of artificial rough rolling-sliding contact .....	122
5.3.1. Simulation procedure .....	122
5.3.2. Contact pressure and wear depth of rough surface .....	123
5.4. Running-in of real rough rolling-sliding contact .....	126
5.4.1. Experiment .....	126
5.4.2. Validation of FE simulation .....	126
5.5. Running-in of lubricated rolling-sliding contacts .....	127
5.5.1. Computational model and procedures .....	128
5.5.2. Results and discussions .....	130
5.6. Concluding remarks .....	131
References .....	132
<b>6. Conclusions and Recommendations</b> .....	<b>135</b>
6.1. Conclusions .....	135
6.2. Discussion and direction for further research .....	136
6.2.1. Abrasion .....	136
6.2.2. Specific wear rate .....	139
References .....	139
<b>Appendix A Measurement of Plastic Deformation of Static Contact between Hemispheres with Different Radii</b> .....	<b>141</b>
<b>Appendix B Modelling and Validation of the Real Rough Surface Contact Using Finite Element Analysis</b> .....	<b>145</b>
<b>List of Publications</b> .....	<b>149</b>
<b>Acknowledgement</b> .....	<b>151</b>





## Nomenclature

---

This section presents the general nomenclature used in this thesis. Certain specialized terminology is defined locally.

### Roman symbol

$A$	contact area	[m <sup>2</sup> ]
$a$	contact radius	[m]
$a_{(x)}$	semi-major axis length of the contact ellipse	[m]
$a_{(y)}$	semi-minor axis length of the contact ellipse	[m]
$b$	contact half width	[m]
$ds$	incremental sliding distance	[m]
$dh$	wear depth	[m]
$E$	Young's modulus	[Pa]
$F_N$	applied normal load	[N]
$F_X$	horizontal reaction force	[N]
$F_Z$	vertical reaction force	[N]
$F_C$	load carried by asperities	[N]
$F_H$	load carried by fluid film	[N]
$H$	hardness	[Pa]
$h_c$	central film thickness	[m]
$h_e$	elastic wear depth	[μm]
$h^w$	wear depth	[μm]
$i$	increment	[-]
$k_e$	elastic wear coefficient	[-]
$k_m$	wear coefficient for rubbing wear	[-]
$k_p$	plastic wear coefficient	[-]

## XIV

$K$	dimensionless wear coefficient	[-]
$K_D$	specific wear rate	[mm <sup>3</sup> /Nm]
$L$	sampling length	[m]
$N$	number of rotations	[-]
$p_H$	hydrodynamic pressure	[N/m <sup>2</sup> or Pa]
$p$	pressure	[Pa]
$p_o$	maximum contact pressure	[Pa]
$R$	radius	[m]
$R'$	equivalent radius of curvature	[m]
$Ra$	arithmetic average of asperity heights	[m]
$Rq$	standard deviation of asperity heights	[m]
$s$	sliding distance	[m]
$t_0$	time of vibration of the adsorbed state	[s]
$T_s$	surface temperature	[K]
$u$	elastic displacement	[m]
$u_{rolling}$	rolling velocity	[m/s]
$U_{slf}$	sliding velocity	[m/s]
$V$	worn volume	[m <sup>3</sup> ]
$V$	linear velocity	[m/s]
$y_s$	distance between mean of asperity heights and mean of surface height	[m]
$Z_{lub}$	viscosity-pressure index of lubricant	[-]
$z$	asperity height	[m]

### Greek symbol

$\alpha$	fractional film defect	[-]
$\beta$	radius of tip of asperity	[m]
$\delta t_i$	increment of time	[s]
$\epsilon$	fraction	[-]
$\theta$	circumferential coordinate	[-]
$\nu$	Poisson's ratio	[-]
$\mu$	coefficient of friction	[-]
$\sigma$	stress	[Pa]
$\omega$	interference	[m]
$\gamma_1$	scaling factor for hydrodynamic part	[-]
$\gamma_2$	scaling factor for asperity contacting part	[-]

### Subscript and superscript

1, 2	surface 1, 2
as	asperity

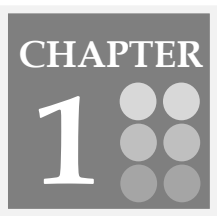
<i>c</i>	critical
<i>cyl</i>	cylinder
<i>D</i>	disc
<i>e</i>	elastic
<i>ep</i>	elastic-plastic
<i>i</i>	load step number
<i>max</i>	maximum
<i>P</i>	pin
<i>p</i>	plastic
<i>res</i>	residual
<i>u</i>	unloading
<i>x</i>	corresponding to horizontal <i>x</i> axis
<i>y</i>	corresponding to horizontal <i>y</i> axis
<i>Y</i>	yield
<i>z</i>	corresponding to vertical <i>z</i> axis
<i>vm</i>	von Mises

### Abbreviations

BEM	Boundary Element Method
EHL	Elasto-Hydrodynamic Lubrication
FEA	Finite Element Analysis
GIWM	Global Increment Wear Model
ML	Mixed Lubrication





A graphic for Chapter 1. It features the word "CHAPTER" in a white serif font at the top. Below it is a large white number "1". To the right of the "1" are six grey circles arranged in a 2x3 grid. The entire graphic is set against a dark grey background with a thin white border.

# CHAPTER 1

## Introduction

---

### 1.1 Tribology

Tribology is the science and technology of friction, wear and lubrication. It studies the interaction of surfaces in relative motion. It concerns the understanding of a wide range of applications, from simple everyday products to complex industrial machinery and also from the artificial human joint to the aerospace journal bearing.

In a highly industrialized country, tribology demonstrates its importance by reducing material use and energy loss in, for instance, power generation systems, manufacturing industry and industrial processes. Already in the late 70s this was recognized by Czichos [1] and Jost [2], who estimated that the dissipated energy due to friction amounts to 30% of the total energy generated. Later Summers-Smith [3] indicated that this number could be higher than predicted before. Recent research in the US states that 57.5% of all generated energy is not only wasted by transport losses, but also by insufficient processes (read: friction losses) [4].

Tribology provides industry with design tools for, for instance, increased product quality, failure analysis and providing beneficial maintenance schedules. An example is given of a small company that produces gears and tribology assisted in increasing the gear quality. Figure 1.1 shows some gears produced by a company in Central Java, Indonesia, used in transmissions for automotive applications. The lifetime of the components in the transmission did not meet the requirements due to wear and local plastic deformation. Better surface characteristics were recommended based on tribological knowledge, e.g. modifying the manufacturing process and the heat treatment of the gears. This is one example of applying tribology science in engineering practice. The

understanding of tribological knowledge is important for Indonesian small and medium sized companies (SMEs) which feel the pressure from foreign products in the domestic market of automotive components.



**Figure 1.1:** Gears manufactured for transmissions in Indonesia.

In designing the surface characteristics of mechanical parts, especially components which are in contact in mechanical systems, such as gears, camshafts and followers, bearings, piston-rings and cylinder liners, comprehensive knowledge of friction and wear affecting the contact pair in the moving contact is required. In the design process, the entire lifespan of the components should be considered. This lifespan can be divided into the running-in phase, the steady-state phase and the wear-out phase. The running-in phase is a critical phase in the functioning of mechanical components, but it is frequently overlooked during the design process.

## **1.2 Running-in**

### **1.2.1 The running-in to steady-state phase**

The running-in phase is a transient phase, where the friction and wear between two fresh and unworn surfaces, which are in contact, vary considerably in time. During this phase, the surface properties of the components are adjusted. If the initial surface roughness of the rubbing surfaces was correctly chosen, the running-in eventually reaches a steady-state phase. At this stage, the rubbing surfaces are in general smoother and their wear rate is low and constant. On the other hand, an inappropriate choice of roughness may lead to a rapid deterioration of the rubbing surfaces [5]. The micro-geometry of the surface is an important factor in determining the life of mechanical components. During the running-in phase, the highest asperities are “flattened”, thereby increasing the number of

asperities in contact and, as a result, increasing the load-carrying capacity of the surface, as reported by Östvik and Christensen [6].

During the running-in phase the surface becomes smoother, where the smoothing mechanism of surfaces should be analysed in terms of wear of the roughness peaks, in terms of filling the surface valleys by the wear debris [7] and also in terms of plastic deformation of the asperities [8].

The running-in phase is followed by a steady-state phase, defined as the condition of a given tribo-system in which the average dynamic coefficient of friction, specific wear rate and other specific parameters have reached and maintain a relatively constant level [9]. At the steady-state phase, the wear of the tribo-system becomes more stable and the system operates at an optimum during the lifetime.

### 1.2.2 The effects of contact motion on running-in

As explained by Kalker [10], there are three main types of motion, namely rolling, sliding and rolling-sliding. Each motion generates a different surface topographical change. For the surface topographical change during the running-in period, there are two dominant mechanisms: plastic deformation and mild wear [11]. These mechanisms occur shortly after the start of a sliding, rolling or rolling-sliding contact between fresh and unworn solid surfaces.

The rolling contact motion induces plastic deformation at the higher asperities when the elastic limit is exceeded, as investigated experimentally by Jamari [8]. In a ball-on-disc system, the rolling contact generates a track on the disc in which the surface topography is modified. In this case, the plastic deformation mechanism due to normal loading is a key factor in truncating the highest asperities, decreasing the centre line average roughness,  $R_a$ , and changing the surface topography [6]. For pure rolling contacts, the effects of wear on the change of the surface topography are usually neglected. In sliding contacts, the change of the surface topography is commonly influenced by (mild) wear, considering wear mechanisms such as abrasive, adhesive and oxidative. Contrary to the rolling contact, many models for predicting the surface topography change during running-in of a sliding contact are proposed ignoring the plastic deformation.

For running-in of rolling contacts with slip, which is a rolling-sliding contact situation, both plastic deformation and wear need to be considered. Recently two models were proposed to predict wear and change in surface topography for rolling-sliding contacts: Wang et al. [12] calculated the wear of an asperity during partial elasto-hydrodynamic lubrication (PEHL) to predict the change of surface roughness, i.e.  $R_a$  as a function of the slide-to-roll ratio and normal load. Akbarzadeh and Khonsari [13] calculated the change of the surface roughness,  $R_a$  using the normal plastic deformation and subsequently predicted the wear as a function of the initial surface roughness, the slide-to-roll ratio and the rolling velocity.

### 1.2.3 Modelling the running-in phase

Based on the literature review, which is discussed intensively in the second chapter, a schematic illustration, presented in Fig. 1.2, is constructed and consists of items related to modelling the running-in phase of rolling, sliding and rolling-sliding contacts. Four aspects are indicated in this figure: the type of lubrication of the contacting bodies, the method of modelling, the type of the contact motion and the parameters to observe.

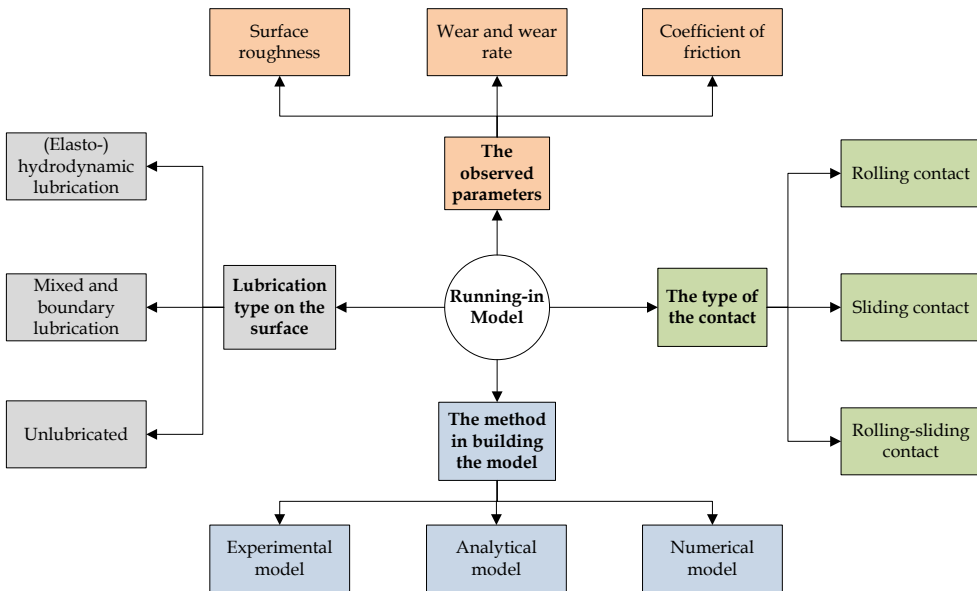


**Figure 1.2:** Modelling the running-in phase.

### 1.3 The objective of this thesis

Based on the parameters mentioned in Fig. 1.2, this research is conducted with the aim of exploring the running-in phase for each type of motion which covers the rolling, sliding and rolling-sliding contact. Finite element simulation is employed to predict the running-in phase using a commercial finite element software package to calculate the stress distributions for the three types of contact motions considered.

The simulation of the contacts using finite element analysis assumes a dry or boundary lubricated contact. The evolution of the contact pressure for a certain rolling or sliding distance is studied to unravel the running-in phase. The originality of this study is that it focuses on the evolution of the micro-geometry within a rolling, sliding and rolling-sliding contact using finite element simulation.

## 1.4 Outline

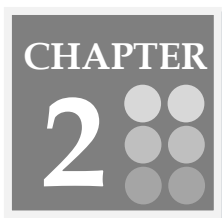
This chapter gives the background and the objective of the thesis. In the second chapter a review of the available literature on running-in is given, covering experiments and numerical and analytical models. Wear and plastic deformation in a sliding, rolling-sliding and rolling contact are studied in depth. In Chapter 3, a rolling contact is simulated using finite elements and the running-in phase is explored by observing the topographical change, the contact stress and the residual stress. Existing analytical models and experimental investigations are used to discuss the results.

Chapter 4 deals with a finite element study of ploughing friction, surface layers and plastic deformation in sliding. This chapter also explores modelling the running-in phase of a sliding contact between a hemisphere and a flat surface using finite element analysis. An experimental investigation and an existing wear model were compared with the present study. Chapter 5 starts with reviewing existing rolling-sliding contact models, which are used to validate the developed finite element model. The running-in of rolling-sliding contacts is researched by observing the contact pressure evolution as a function of the number of overrollings. Then, a micro-scale running-in model for rolling-sliding contacts is developed, covering wear and deformation at asperity level. This model is used to study the running-in of rough surfaces. Finally, conclusions are drawn and recommendations are given in Chapter 6.

## References

- [1] Czichos, H., 1978, *Tribology: A Systems Approach to the Science and Technology of Friction Lubrication and Wear*, Elsevier, Amsterdam, The Netherlands.
- [2] Jost, P., 1976, "Some economic factor of tribology," *Proceeding of JSLE-ASLE International Lubrication Conference* (Ed: T. Sakurai), p 2.
- [3] Summers-smith, D., 1986, "Ten years after Jost: The effect on Industry," *Proceeding of Tribology Convention, Institute of Mechanical Engineering*, p. 21.
- [4] Simon, A.J. and Belles, L., 2011, "Estimated state-level energy flows in 2008," Lawrence Livermore National Laboratory.
- [5] Masouros, G., Dimarogonas, A. and Lefas, K., 1977, "A model for wear and surface roughness transients during running-in of bearings," *Wear*, 45 pp. 375-382.
- [6] Östvik, R. and Christensen, H., 1969, "Changes in surface topography with running-in," *Proceedings of the Tribology Conventions (Part 3P)*, Vol. 183, Institute of Mechanical Engineering, London, pp. 57-65.
- [7] Sreenath, A.V. and Raman, N., 1976, "Mechanism of smoothing of cylinder liner surface during running-in," *Tribol. Int.*, pp. 55-62.

- [8] Jamari, J., 2006, *Running-in of Rolling Contacts*. PhD Thesis, University of Twente, Enschede, The Netherlands.
- [9] Blau, P.J., 1989, *Friction and Wear Transitions of Materials: Break-in, Run-in, Wear-in*, Noyes Publications, Park Ridge, NJ, USA.
- [10] Kalker, J.J., 1990, *Three-dimensional Elastic Body in Rolling Contact*, Kluwer Academic Publishing, Dordrecht, The Netherlands.
- [11] Whitehouse, D.J., 1980, "The effect of surface topography on wear," In: *Fundamentals of Tribology*, Suh and Saka (Ed.), The MIT Press, Massachusetts, USA, pp. 17-52.
- [12] Wang, W., Wong, P.L. and Guo. F., 2004, "Application of partial elasto-hydrodynamic lubrication analysis in dynamic wear study for running-in," *Wear*, 257, pp. 823-832.
- [13] Akbarzadeh, S., and Khonsari, M.M., 2010, "Effect of Surface Pattern on Stribeck Curve," *Tribology Letters*, 37, pp. 477-486.

A square graphic with a dark grey background. The word "CHAPTER" is written in white, uppercase letters at the top. Below it, the number "2" is written in a large, white, serif font. To the right of the number "2" is a 3x3 grid of nine circles, each with a different shade of grey, ranging from light to dark.

## Literature

---

### 2.1 Introduction

Running-in is known as a tribological process that occurs during the initial phase between contacting fresh and unworn solid surfaces. From a macroscopic point of view, for instance, for a new gear transmission in a motorcycle engine, running-in promotes beneficial operating conditions by inducing the proper contact “fit” between the gear teeth. If, however, the proper contact fit is not obtained, the contact stress can increase and cause excessive running temperatures, wear and vibrations. From a microscopic point of view, running-in is important with respect to surface topography adjustment in order to get the required surface condition. By managing a good running-in phase, the surface adjustment promotes an improvement in friction, wear and lubrication behaviour.

Previous research on the running-in phase is reviewed and discussed in this chapter; the focus will be put on the surface topographical change of the contacting bodies, which covers rolling, sliding and rolling-sliding motion. This chapter is divided into six sections, where the first section is meant as an introduction. The second section deals with the definitions and the significance of running-in. The classification of running-in is divided, based on the type of motion, and is discussed in sections 3 to 5, i.e. running-in of rolling contacts, sliding contacts and rolling-sliding contacts, respectively. Each section describes the definition of the contact motion, the surface topographical change, the running-in model and the running-in experiment. Finally, conclusions on running-in of rolling-sliding contacts are made.

## 2.2 Running-in

### 2.2.1 The definition of running-in

Running-in, which is related to the terms breaking-in and wearing-in [1], has been connected to the process by which contacting machine parts improve in conformity, surface topography and frictional compatibility during the initial stage of use. It focuses on the interactions which take place at the contact interface on macro scale and asperity scale and involves a transition in operational conditions. For instance, in gear transmissions, tribologists observe the transition from the unworn to the worn state, from one surface roughness to another surface roughness, from one contact pressure to another contact pressure, from one frictional condition to another, etc. However, the physical change of the contacting surfaces in this phase, which can be categorized as “physical damage” at asperity level, is more beneficial instead of detrimental.

Lin and Cheng [2] distinguished three types of wear-time behaviour. The majority of the wear time curves observed is of type I, in which the wear rate is initially high and then decreases to a lower value. Wear of type II is more usually observed under dry conditions and the wear rate is constant in time, whilst the wear rate of wear type III is increasing continuously with time. Jamari [3] presented the wear-time curve which consists of three wear regimes: running-in, steady state and accelerated wear and finally wear-out as shown in Fig. 2.1. Each regime has different wear behaviour.

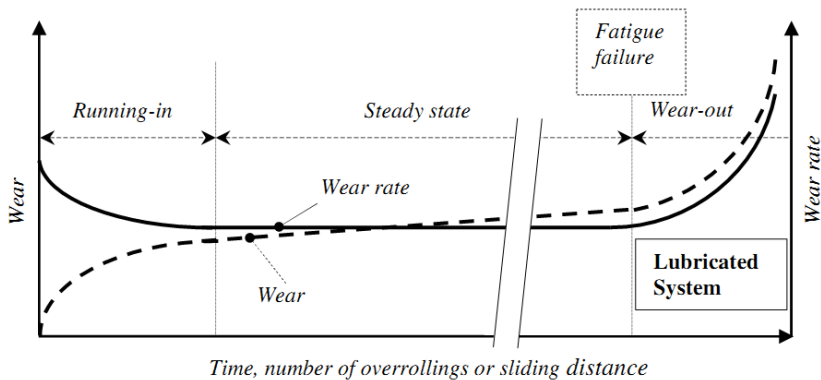


**Figure 2.1:** Schematic representation of the wear behaviour as a function of time, number of overrollings or sliding distance of a contact under constant operating conditions, after Jamari [3].

During running-in, the wear-time curve behaves as wear type I and the surface of the material gets adjusted to the contact condition and the operating environment. Wear regime of type II usually takes place in the steady-state wear process where the wear-time function is nearly linear. In the wear-out regime, the



wear rate increases rapidly because of fatigue wear which occurs on the upper layers of the loaded surface. Dynamic loading causes fatigue of the surface and results in material loss of small fragments associated with either adhesive or abrasive wear mechanisms. Breakdown of lubrication due to temperature increase, lubricant contaminants or environmental factors are other causes of the increase of wear and wear rate in this regime [4].

Figure 2.2 depicts schematically the friction and roughness decrease as a function of time, number of overrollings and/or sliding distance. In the running-in phase, a change in surface roughness is required to adjust or minimize the energy flow between the moving surfaces [5]. Based on Fig. 2.2, phase I of the running-in regime is indicated by a significant decrease of the surface roughness and the coefficient of friction. In phase II of the running-in regime, the repetitive contact causes work hardening, resulting in an increase of the micro-hardness and the residual stresses in the surface [3]. During this phase the decrease in the coefficient of friction and surface roughness is limited. It is desirable, for machine components, to operate as long as possible in the steady-state regime with respect to the component's lifetime or maintenance intervals.

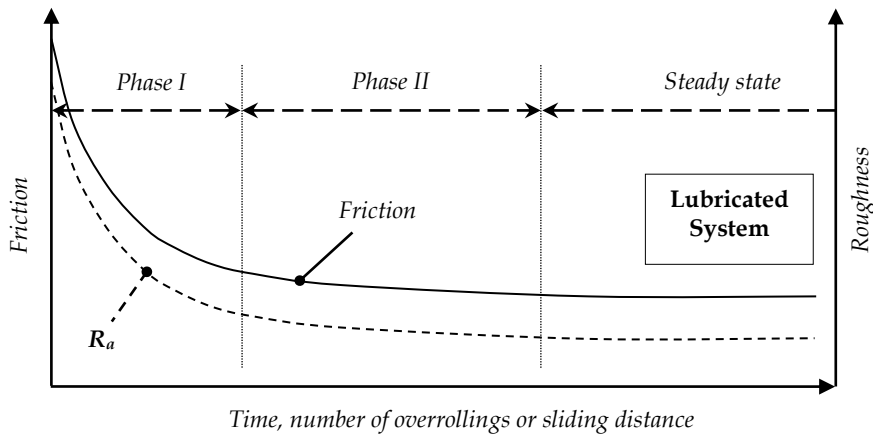


**Figure 2.2:** The change of the coefficient of friction and roughness as a function of time, number of overrollings or sliding distance of a contact under constant operating conditions [3].

### 2.2.2 The significance of running-in

During running-in, the system adjusts to reach a steady-state condition between contact pressure, surface roughness, interface layer, and the establishment of an effective lubricating film at the interface. These adjustments may cover surface conformity, oxide film formation, material transfer, lubricant reaction products,

martensitic phase transformation, and subsurface microstructural reorientation [6]. Then, the running-in phase is followed by a steady-state phase which is defined as the condition of a given tribo-system in which the average dynamic coefficient of friction, specific wear rate, and other specific parameters have reached and maintain a relatively constant level [1].

Summer-Smith [7] summarized the importance of the running-in phase with his statement "If conditions were wrong, piston rings could disappear within 24 h after start up." With a successful run-in and good maintenance, piston ring life could be utilized until 10 years. Kehrwald [8] expressed the impact of the running-in phase by predicting that an optimized running-in procedure has a potency to improve the lifetime of a mechanical system by more than 40% as well as reducing the engine friction without any material modifications. Jamari [3] highlighted that ignoring the running-in aspects means overlooking the important clues to the evolution of conjoint processes, which leads to the final long-term steady-state friction and wear behaviour. Nowadays, with respect to energy efficiency and engine emissions, the understanding of the changes of the surface topography of the piston-ring contact during the running-in phase is one of the important factors in controlling a lower fuel and oil consumption in automotive engines [4].

The quotations above indicate the significance of the running-in phase, which occurs at the beginning of the contact in a mechanical system. The running-in phase is known as a transient phase where many parameters seek their stabilized form.

## **2.3 Rolling contact**

### **2.3.1 The definition of a rolling contact**

When two non-conformal contacting bodies are pressed together so that they touch in a point, elliptical or a line contact, and they are rotated relatively to each other so that the contact moves over the bodies, there are three possibilities of motion. At first, a rolling contact is defined as a motion where the velocities of the contacting bodies are equal at each point along the tangent plane of contact. Secondly, sliding is defined as when one of the bodies is stationary and the other is moving. The third option is a combination of the two aforementioned situations, i.e. rolling with a sliding motion [9]. According to Johnson, a combination of rolling, sliding and spinning can take place during the rolling of two contacting bodies [10].

In the case of rolling friction where the friction takes place in the rolling contact and produces the resistance to motion, Halling [11] classified: (a) Free rolling, (b) Rolling subjected to traction, (c) Rolling in conforming grooves and (d) Rolling around curves. Whenever rolling occurs, free rolling friction must occur, whereas (b), (c) and (d) occur separately or in combination, depending on the particular situation. The tire of a car involves (a) and (b), in a radial ball bearing (a), (b) and (c) are involved, whereas in a thrust ball bearing (a), (b), (c) and (d) occur.

Depending on the forces acting on the contacting bodies, rolling can be classified as free rolling and tractive rolling. Free rolling is used to describe a rolling motion in which there is almost no slip and the tangential force in the contact is nearly zero. The term tractive rolling is used when the tangential force in the contact is significant and slip exists.

### 2.3.2 Rolling contact on a flat surface

Investigations into rolling contact phenomena have been conducted for many decades and cover the analysis of contact pressures, stress distributions and deformations. Three types of analysis methods are often used: analytical, numerical such as the finite element method (FEM), and the semi-analytical method (SAM). The analytical method is used to predict the contact stress and deformation of the rolling contact, Kalker [9]. A number of elastic and elastic-plastic stress analyses of rolling contacts were investigated using FEM. Bhargava et al. [12] and Kulkarni and his co-workers [13-14] started their investigation on rolling contacts using FEM. Jiang et al. [15] developed their model and combined the rolling contact motion with partial slip [16]. The Semi-Analytical approach was introduced by Jacq et al. [17] for the rolling contact situation and was further developed for various contacts and material behaviour [18]. SAM is based on analytic formulae in discrete form, whereas the quantities are obtained by numerical computing.

In the aforementioned articles, the rolling contact was studied by considering the rolling element in contact with a flat surface, where the rolling element can be modelled by a sphere, an ellipsoid or a cylinder. The von Mises contact stress, residual stress, plastic strain, surface displacement and contact pressure can be predicted as a function of the depth from the surface. These parameters act as a key for understanding and predicting fatigue and wear behaviour of a rolling element. The strength and expected life of mechanical components can be influenced by the residual stress due to its effect on contact fatigue and wear.

### 2.3.3 Model of running-in of rolling contact on a rough surface

There are few publications discussing the running-in of rolling contacts dealing with a rough surface. Most of the running-in models available in the literature are devoted to running-in with respect to wear during sliding motion. In this section, the analytical model developed by Jamari and Schipper [19] is discussed, in order to understand the surface topographical change due to running-in of a rolling contact. The discussion of the rolling contact motion at the running-in phase is

focused on the free rolling contact between a rigid body over a flat rough surface and neglecting the tangential force, slip and friction on the contacting bodies.

On the basis of a deterministic elastic-plastic contact model, Jamari and Schipper [19] predicted the change in surface topography during running-in of a rolling contact.

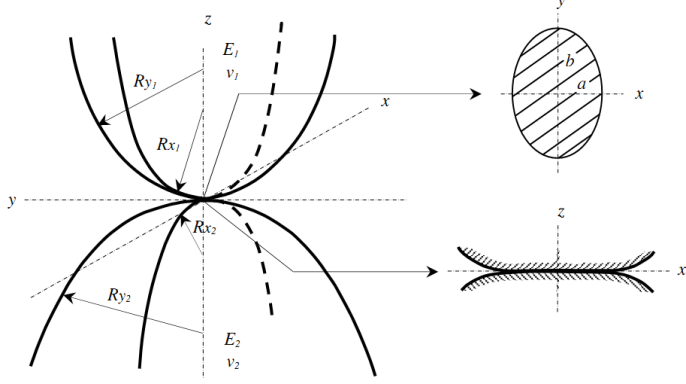


**Figure 2.3:** Geometry of an elliptical contact, after Jamari and Schipper [19].

The model is validated experimentally and good agreement between the model and the experiment results were found. In order to predict the surface topography after running-in of the rolling contact, they modified the elastic-plastic model of Zhao et al. [21] and used the elliptical contact situation to model the elastic-plastic contact between two asperities. Figure 2.3 illustrates the geometrical model of elliptical contact where  $a$  and  $b$  express the semi-minor and semi-major axes of the elliptical contact area. The mean effective radius  $R_m$  is defined as:

$$\frac{1}{R_m} = \frac{1}{R_x} + \frac{1}{R_y} = \frac{1}{R_{x1}} + \frac{1}{R_{x2}} + \frac{1}{R_{y1}} + \frac{1}{R_{y2}} \quad (2.1)$$

$R_x$  and  $R_y$  denote the effective radii of curvature in the principal  $x$  and  $y$  directions and subscripts 1 and 2 indicate body 1 and body 2 respectively. The elliptical based contact model led to modified equations for the elastic-plastic contact area  $A_{ep}$  and the elastic-plastic contact load  $P_{ep}$ , which are defined as follows:

$$A_{ep} = 2\pi R_m \omega \frac{\alpha\beta}{\gamma} + (2\pi \sqrt{R_x R_y} \omega - 2\pi R_m \omega \frac{\alpha\beta}{\gamma}) \left[ 3 \left( \frac{\omega - \omega_1}{\omega_2 - \omega_1} \right)^2 - 2 \left( \frac{\omega - \omega_1}{\omega_2 - \omega_1} \right)^3 \right] \quad (2.2)$$

$$P_{ep} = A_{ep} \left[ c_h H - H \left( c_h - \frac{2}{3} K_v \right) \frac{\ln \omega_2 - \ln \omega}{\ln \omega_2 - \ln \omega_1} \right] \quad (2.3)$$

where  $\omega$  is the interference of an asperity, subscripts 1 and 2 indicate the limit of the first yield interference and the limit of the fully plastic interference respectively,  $a$  and  $\beta$  are the dimensionless semi-axis of the contact ellipse in principal  $x$  and  $y$  direction respectively,  $\gamma$  is dimensionless interference parameter of elliptical contact,  $c_h$  is the hardness factor,  $H$  is the hardness of material and  $K_v$  is the maximum contact pressure factor related to Poisson's ratio  $\nu$ :

$$K_v = 0.4645 + 0.3141\nu + 0.1943\nu^2 \quad (2.4)$$

The change of the surface topography during running-in is analysed deterministically for the pure rolling contact situation. Figure 2.4 shows the proposed model of the repeated contact model performed by Jamari [3]. Here,  $h(x,y)$  is the initial surface topography. The surface topography will deform to  $h'(x,y)$  after running-in. The elastic-plastic contact models in Eq. (2.2) and (2.3) are used to predict the  $h'(x,y)$ . The calculation steps are iterated for a number of overrollings or distance of rolling.

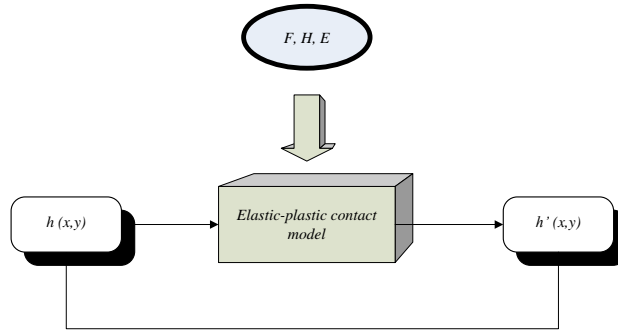


**Figure 2.4:** The model of the surface topography changes due to running-in of a rolling contact proposed by Jamari [3].

### 2.3.4 Experiments on the running-in of rolling contacts

In this section the experiments on running-in of rolling contact by Jamari [3] and Taşan et al. [22] are discussed. These experiments were used to validate the running-in model which has been explored in the previous section. Furthermore, the experiments were employed for exhibiting the change of the surface topography in lateral and longitudinal direction of the rough surface due to running-in of a rolling contact.

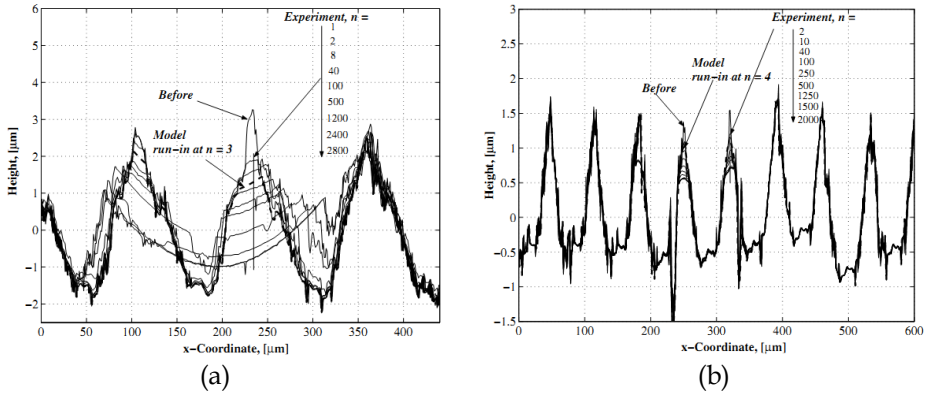


**Figure 2.5:** Profiles across the direction of rolling of (a) aluminium surface and (b) mild-steel surface after Jamari [3].

Experiments on the running-in of rolling contacts are conducted on the measurement setup presented in Jamari [3]. Silicon carbide ceramic balls ( $H = 28$  GPa,  $E = 430$  GPa and  $\nu = 0.17$ ) with a diameter of 6.35 mm were used as hard spherical indenters. The centre line average roughness  $Ra$  of the ceramic ball of  $0.01 \mu\text{m}$  was chosen to comply with the assumption of a perfectly smooth surface. Elastic-perfectly plastic aluminium ( $H = 0.24$  GPa,  $E = 75.2$  GPa and  $\nu = 0.34$ ) and mild-steel ( $H = 3.55$  GPa,  $E = 210$  GPa and  $\nu = 0.3$ ) were used for the rough flat surface specimens. The centre line average roughness of the flat specimens varied from  $0.7$  to  $2 \mu\text{m}$ .

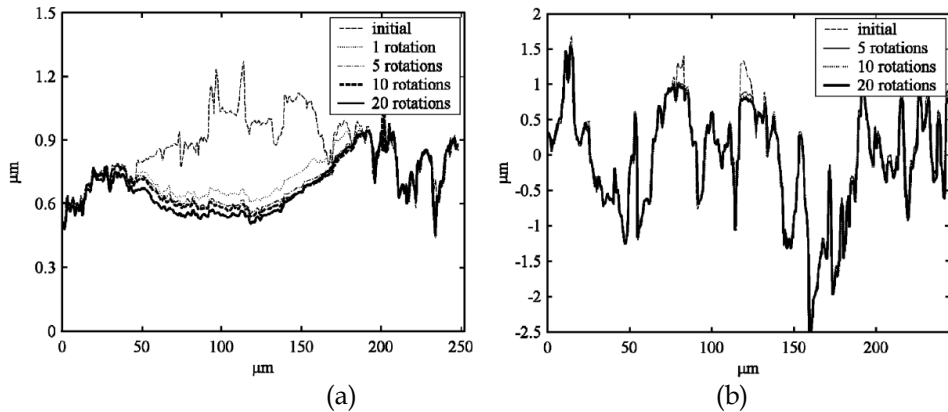


**Figure 2.6:** Profiles across the direction of rolling for (a) lateral and (b) longitudinal roughness as a function of the number of rolling cycles, after Taşan, et al. [22].

Results of the rolling contact experiment, along with the model prediction for the aluminium and mild-steel surfaces, are presented in Figs. 2.5a and 2.5b,

respectively. Another investigation, performed by Taşan et al. [22] on the topographical change of a rolling contact between an SiC ball in contact with a rough mild steel disk (DIN 100MnCrW4), is presented in Fig. 2.6, which depicts the topographical change of the surface in (a) the lateral direction and (b) the longitudinal direction. A complete description of these experiments can be found in Taşan [23].

## 2.4 Sliding contact

### 2.4.1 The definition of sliding contact

Sliding is identified as the relative velocity between the two bodies or surfaces at the contact point in the tangent plane [10]. In a sliding contact, the change of the surface topography is commonly influenced by mild wear, considering several wear mechanisms such as abrasive, adhesive and oxidative. The wear models are discussed in order to analyse literature on wear prediction.

### 2.4.2 General wear model of Archard

Over the years, many researchers have carried out studies in modelling wear, which has resulted in many models for many different situations. The literature is rich with wear equations that correlate with the specific system considered. There are nearly 200 wear equations containing 32 different parameters, involving numerous material properties and operating conditions that have been identified by various authors [24]. There is no simple, universal model available that can predict wear on the basis of mechanical properties and contact information only [25].

A starting point in the analysis of wear was conducted by Holm [26] and continued intensively by Archard [27]. Archard's wear equation postulates that the wear rate, i.e. the volume worn away per unit sliding distance, is proportional to the load and the material combination. Then, the depth of wear,  $h$ , is derived and can be calculated with Eq. (2.5).

$$h = \frac{K}{H} sp \quad (2.5)$$

The wear coefficient is denoted by  $K$ ,  $H$  is the hardness of the worn surface,  $s$  is the sliding distance and  $p$  is the contact pressure. The wear coefficient and the hardness can be replaced by the dimensional wear rate,  $k$ , which is widely used when comparing the wear resistance of materials:

$$h = k s p \quad (2.6)$$

The proportionalities in the Archard model are not always observed in experimental approaches. For example, Dorinson and Broman [28] found a non-linear relation between the load and the amount of wear. Richards [29] obtained higher wear rates for higher hardness and Hirst [30] obtained a wear rate that varies in time. Nevertheless, the Archard wear equation (AWE) still is the most popular and widely used model in recent wear prediction studies. AWE was initially developed on the basis of adhesive wear, but some researchers have shown that the AWE also can be used to accurately predict abrasive and corrosive wear [24-25, 31-41].

### 2.4.3 Finite element based model

Modelling sliding wear, in order to derive predictive governing equations, has been a subject of extensive research in the past decades. Wear models found in the literature can in general be classified into two main categories, (i) mechanistic models, which are based on a material failure mechanism, e.g. the ratcheting theory for predicting wear [42-43] and (ii) phenomenological models, which often involve quantities that have to be computed using principles of contact mechanics, e.g. the wear model of Archard [27].

The Archard-based wear model has been studied extensively using the finite element analysis. The (modified) Archard's wear equation is still widely used, especially for the mild wear situation of the sliding contact, with satisfactory results [31-41]. Podra [31] simulated the sliding wear of a pin-on-disc system using the finite element method, which was further developed by Andersson and his colleagues [32-35]. A numerical simulation of wear of a cylindrical steel roller oscillating against steel was performed by Oqvist [36] with a customized version of finite element program: the simulation was done in steps and the pressure and the sliding distance were recalculated as the surface geometry changed. Other researchers used FE simulations for different wear mechanisms and different materials [37-40]. Mukras et al. [41] introduced a wear prediction model for an oscillatory conforming contact.

Similar to Podra and Andersson [31], Hegadekotte et al. [44-46] and Kanavali [47] proposed a modelling scheme for the wear as obtained using various tribometers. They used a numerical solution based on FEM which is introduced as Wear-Processor. It implements AWE on the local scale. The pin and the disc are modelled as a 3D static contact problem in the commercial FE code ABAQUS. The stress field, the displacement field and the element topology are then extracted from the FE results. The calculated wear from Archard's wear model, where the contact pressure is obtained from the FE solution, is used to update the geometry by repositioning the surface nodes with a re-meshing technique that makes use of the boundary displacement method. The obtained new reference geometry is then



used to calculate the updated stress distribution, which in turn is used to compute the updated contact pressure distribution. This step is repeated until the expected sliding distance is reached. Some results of the contact pressure and tangential stress obtained with the Wear Processor are depicted in Fig. 2.7.

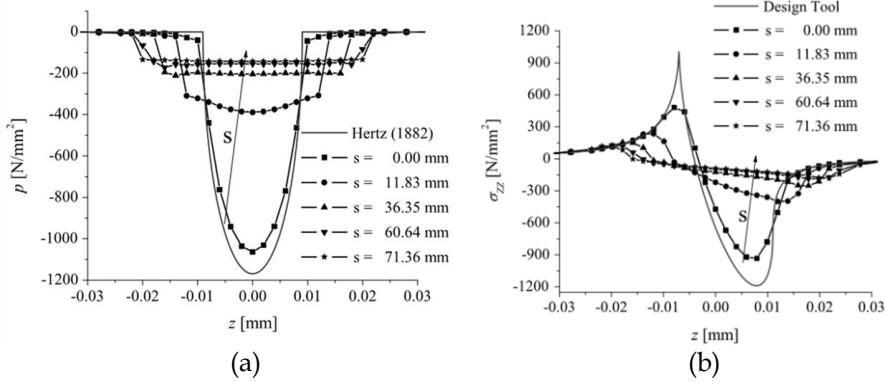


**Figure 2.7:** Contact stresses after various intervals of sliding: (a) contact pressure profile; (b) tangential stress  $r_{zz}$  in direction of sliding, after Hegadekatte [45].

#### 2.4.4 Global increment wear model

An incremental implementation of Archard's wear model on the global scale (Global Incremental Wear Model - GIWM) was proposed by Hegadekatte et al. [45] in predicting the wear depth of both pin and disc in a pin-on-disc tribometer. The equation considers only global quantities such as the average contact pressure, which is computed incrementally by updating the contact pressure at various intervals of sliding. Initially, the contact radius  $a_0$  using the Hertz solution [48] is calculated as follows:

$$a_0 = \sqrt[3]{\frac{3F_N R_p}{4E_C}} \quad (2.7)$$

where  $F_N$  is the applied normal load,  $R_p$  is the radius of the pin and  $E_c$  is the equivalent elastic modulus. The elastic deformation normal to the contact using the relation as proposed by Oliver and Pharr [49]:

$$h_{i+1}^e = \frac{F_N}{2E_C a_{i+1}} \quad (2.8)$$

where  $i$  is the current wear increment number. The linear wear is integrated over the sliding distance using the Euler explicit method:

$$h_{i+1}^w = k_D p_i \Delta s_i + h_i^w \quad (2.9)$$

where  $k_D = K/H$  is the wear rate,  $p$  is the contact pressure and  $\Delta s$  is the interval of the sliding distance.  $h^w$  is the current wear depth as predicted by:

$$h^w = \sqrt{\frac{F_N}{\pi R_p}} k_D s \quad (2.10)$$

Using the GIWM a good agreement was obtained with experimental results at normal loads of 200 and 400 mN. A deviation was found for 800 mN of normal load, see Fig. 2.8a. Figure 2.8b shows the comparison of the GIWM model and the Wear-Processor model for Si<sub>3</sub>N<sub>4</sub> on Si<sub>3</sub>N<sub>4</sub> pin-on-disc test with a 200 mN normal load.

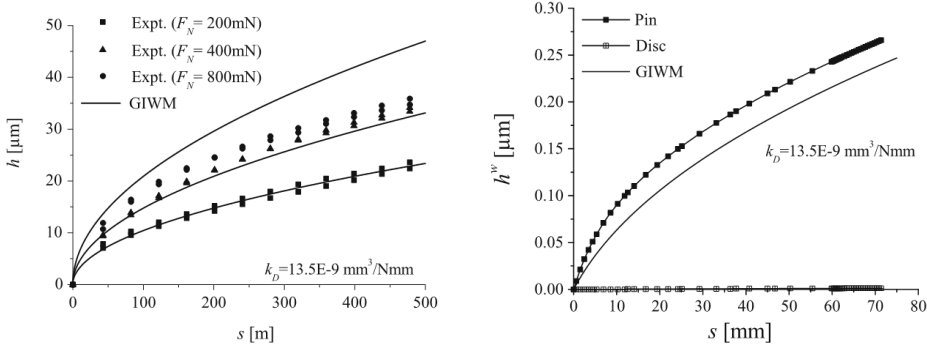


**Figure 2.8:** Wear prediction for Si<sub>3</sub>N<sub>4</sub> on Si<sub>3</sub>N<sub>4</sub> pin-on-disc test: (a) Results from GIWM in comparison with the experimental results from the pin-on-disc tribometer. (b) The comparison of the wear progress over sliding distance for pin and the disc between Wear-Processor and GIWM [45].

#### 2.4.5 Models for running-in of sliding contacts

For sliding contacts, the change of the surface topography is typically the result of mild wear, considering several wear mechanisms such as abrasive, adhesive and oxidative. Many models ignore plastic deformation [50].

The models for predicting the surface topography change due to running-in are most frequently related with the sliding contact situation. Stout et al. [51] and King and his co-workers [52], predict the topographical changes in the running-in phase by considering truncated functions of the Gaussian surface

height distribution to obtain the run-in height distribution. Sugimura et al. [53] continued by proposing a sliding wear model for the running-in process considering abrasive wear and the effects of wear particles. An engineering surface cannot always be described properly by a Gaussian height distribution, therefore also many non-Gaussian height distributions systems have been applied.

Lin and Cheng [54] and Hu et al. [55] used a dynamic system approach in order to develop a model representing all the phases during wear, i.e. running-in, steady state and accelerated wear (wear-out). In the dynamic wear model, Lin and Cheng [54] proposed that the wear rate is proportional to a “forcing” term  $I$ , which is contributed to the normal load and the stress field induced by the frictional force at the asperity contacts. The wear rate is inversely proportional to the wear resisting term,  $S$ , which is related to the material’s anti-wear strength near the surface. Wear rate is calculated by:

$$\dot{W} = cI / S \quad (2.11)$$

where  $\dot{W}$  is the “wear rate”,  $c$  is a dimensionless constant that can be determined experimentally or theoretically. A statistical approach was used to describe the wear rate, anti-wear strength and the average of the shear force. The model developed was compared with experiments conducted by Ruff et al. [56] and Stout et al. [57] and also compared with the statistical running-in wear model of Sugimura et al. [54].

Hu et al. [55] proposed the effect of the surface roughness in determining the dynamic wear rate by considering the linear velocity between two mating surfaces,  $V$ . The equation was expressed as follows:

$$\dot{W} = \frac{F_N V}{H} F(R_\sigma) \quad (2.12)$$

where  $\dot{W} = dW/dt$  and  $F(R_\sigma)$  denotes a function representing the effect of the root mean square of the composite roughness of two mating surfaces. In the running-in phase, where the wear behaves non-linear, Hu et al. summarized that the wear rate will rise as the amplitude of the surface roughness increases [55].

Shirong and Gouan [58] used scale-independent fractal parameters and Zhu et al. [59] predicted the running-in process by the change of the fractal dimension of frictional signals. Liang et al. [60] used a numerical approach based on the elastic contact stress distribution of a three-dimensional real rough surface while Liu et al. [61] used an elastic-perfectly plastic contact model. It is shown that in the running-in of a sliding contact, parameters such as load, sliding velocity, initial surface roughness, lubricant, and temperature have certain effects.

Wang et al. [62] proposed a wear model that was derived from the relation between the wear volume and the change of the average surface roughness under “zero-wear”. Zero wear (on asperity level) is a terminology where the contact

components run under partial elasto-hydrodynamic lubrication (PEHL), with the result that the wear occurs within the original surface topography. A Gaussian height distribution was adopted to generate a rough surface. By assuming PEHL, wear occurs at the rough surface and contact takes place at the summits of the asperities, leading to the flattening of the asperities. The relation between the non-dimensional wear volume  $\bar{W}$  and the non-dimensional change of surface roughness  $\Delta R_a$  was described as a second order polynomial as:

$$\bar{W} = a_1 \Delta R_a^2 + a_2 \Delta R_a \quad (2.13)$$

where  $a_1 = 0.5$  and  $a_2 = 1.02$  which are determined by curve fitting from twenty independently generated surfaces. The wear model has been validated by experiments. Specimens with a higher initial roughness show a rather good agreement with the model but specimens with lower initial roughness deviated from the model. This model is purely based on geometrical relationships and statistics.

Kumar et al. [63] explained that with the increase of load, roughness and temperature, the running-in wear rate of a sliding contact will increase. The experiment was conducted by sliding an En 31 steel ball over the disc made from the same material (hardened) in a reciprocating tester. From the results of the experiments, they developed an empirical relation for the running-in wear rate, running-in period and steady-state wear rate.

Nelias et al. [64] developed the SAM, introduced by Jacq et al. [17], in predicting the surface topographical change due to running-in of a sliding system. Wear prediction is based on a threshold criterion of surface failure. The threshold criterion was determined by 0.2 % maximum equivalent plastic strain where the surface will tear as observed by Oila and Bull [65]. The wear is a result of subsurface cracks which run along the plastic volume when the critical plastic strain value was reached. The SAM based running-in wear model was improved by Bosman and Schipper [66] who studied the wear of a sliding system under boundary lubrication. The investigation was performed for a system that consists of three layers, namely, a physically/chemically adsorbed layer, a chemical reaction layer and a nano-crystalline layer on top of the bulk material. It was found that the contribution of the nano-crystalline layer is significant to the wear and the frictional behaviour of a boundary lubricated system.

#### 2.4.6 Running-in of sliding contacts, some experiments

The work of Blau [67] is considered to be a fundamental model for running-in of sliding contacts based on experiments. He collected numerous examples of running-in experiments from literature and conducted laboratory experiments,

which resulted in sliding coefficient of friction versus time graphs, in order to develop a physical realistic and useful running-in model. This survey revealed eight common forms of coefficient of friction versus sliding time curves. Blau also discusses the causes related to each type of friction-time curve [67]. Each type is not uniquely ascribed to a single process or a unique combination of processes, but has to be analysed in the context of the given tribosystem.

Dienwiebel and Pohlman [68] studied nano-crystalline layers in lubricated sliding contacts during running-in by means of on-line measurements using the radionuclide technique (RNT). The contribution of anti-wear additives was described for high, moderate and low stress conditions, especially on the transient friction and wear of lubricated metal surfaces during the running-in phase. The running-in phase was analysed based on the idea of Umeda et al., [69] which exhibits the correlation between the wear particles characteristics and the generation process of the surface morphology. A method for analysing running-in wear particles was developed by Yuan et al. [70]. In the running-in phase, wear debris is dominantly generated by the interaction between the asperities of the contacting surfaces, resulting in rough surfaces as well as scratches. Smooth plate-like wear particles were formed in the steady-state phase.

## 2.5 Rolling-sliding contact

### 2.5.1 The definition of rolling-sliding contact

When two rotating bodies, such as gears, come into contact with each other and they have the same velocity at the point of contact then they represent a pure rolling contact, where no slip or sliding occurs along the contact [9]. For gears, the pure rolling contact only occurs at the pitch points of the involute profiles of the teeth. Slip or sliding is found for the other contact situations along the path of contact and, therefore, most rolling contacts are in essence rolling-sliding contacts. Such contacts are often experimentally studied with a two-disc machine.

### 2.5.2 FEM based wear model on rolling-sliding contacts

Hegadekotte et al. [46] introduced two types of FEM based wear models which are known as the Wear-Processor and UMESHMOTIONS. Both methods use the same finite element software package ABAQUS. The Wear-Processor has been discussed in the previous section on sliding contacts to predict the contact pressure coupled with the Archard wear model [27] to calculate the material loss.

In the case of a two-disc machine, as shown schematically in Fig 2.9a where the upper disc has a crown radius and the bottom disc is cylindrical, the apparent contact area is elliptical. At the outermost circumference, the two discs rotate with velocities  $V_1$  and  $V_2$ , where  $V_1 \neq V_2$ . The existence of slip between the discs together

with a normal load acting on them, results in sliding wear, for which Archard's wear law is known to be applicable. Such a system is similar to the one shown on the right-hand side in Fig. 2.9b, in which the bottom disc is fixed and the top disc rotates at the slip velocity  $V = |V_1 - V_2|$ . With this assumption, the problem can be reduced from a rolling-sliding contact to a quasi-static sliding contact. However, this assumption is only valid when the bottom flat surfaced disc does not wear.

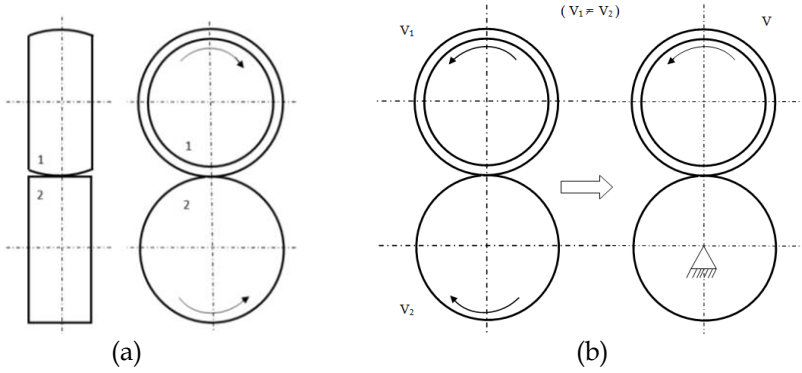


**Figure 2.9:** (a) Schematic of the two-disc machine, and (b) model simplification of rolling-sliding contact with defined slip to sliding contact in the two-disc tribometer [46].

UMESHMOTION is a user-defined subroutine in the commercial FE code ABAQUS which is intended for defining the motion of nodes in an adaptive mesh constraint node set. By defining the contact surface nodes in the adaptive mesh constraint node set, UMESHMOTION can be coded to shift the surface nodes in the direction of the local normal by an amount equal to the corresponding local wear. The new contact pressure is updated by transferring the material quantities from the old location to the new location. The procedure is repeated till a pre-defined maximum sliding distance is reached.

Employing both of UMESHMOTION and Wear-Processor on the rolling-sliding contact, the increment of wear depth was predicted using the Archard's wear model. However, the Euler equation, as it was used in sliding contacts, was adopted for the case of a two-disc machine and was re-written, see Eq. (2.14). A point wears only when it experiences pressure while passing through the contact interface. Therefore, pressures acting on this point were integrated along the sliding direction, corresponding to one rotation for the computation of the local wear increment. For each rotation of the disc, the wear prediction was calculated as follows:

$$h_{j+1} = k_D \int_{\phi=0}^{\phi=2\pi} p r d\phi + h_j \quad (2.14)$$

where  $r = r(y)$  is the radius of the disc at the location of contact (as the top disc surface is curved),  $p$  is the contact pressure and  $\phi$  is the angle of rotation. The calculation of the wear depth using Eq. (2.14) will hold for all the nodes lying along the same circumference (streamline). For a given time increment  $\Delta t_j$ , the wear depth can then be written as:

$$h_{j+1} = k_D \frac{\Delta t_j |V_1 - V_2|}{2\pi R} \int_{\phi=0}^{\phi=2\pi} p r d\phi + h_j \quad (2.15)$$

### 2.5.3 GIWM based wear model for rolling-sliding contact

The GIWM for predicting the wear of a rolling-sliding contact was derived in the same way as GIWM for a sliding contact [46]. Employing the same model as discussed for the FEM based model of sliding contact, the modelling scheme starts with the computation of the initial semi-axis lengths of the contact ellipse using the Hertz solution [48] for an elliptical contact area. Then, the initial normal elastic deformation,  $\delta$ , due to normal load,  $F_N$ , proposed by Oliver and Pharr [49] is corrected for the elliptical contact area.

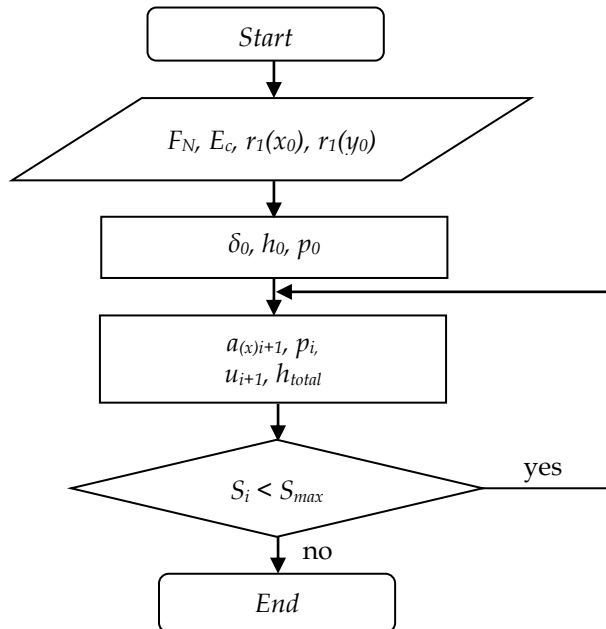


**Figure 2.10:** The simplification of GIWM for a rolling-sliding contact situation [46].

For one rotation of the disc, the sliding distance increment over which wear takes place is given by the axis length of the contact ellipse in sliding direction. The current semi-major axis length of the contact ellipse,  $a_{(y)}$ , and the radius of the top disc,  $R_l$ , is calculated from the geometry of the contact which changes due to wear.

$$a_{(x)i+1} = k \sqrt{\frac{4(F_N / 2a_{(y)i+1})R_{i+1}}{\pi E_c}} \quad (2.16)$$

and

$$p_i = \frac{\pi}{4} \sqrt{\frac{4(F_N / 2a_{(y)i+1})E_c}{\pi R'_{i+1}}} \quad (2.17)$$

The complete structure of the GIWM for wear prediction of a rolling-sliding contact is shown in Fig. 2.10. A comparison between the GIWM model, the UMESHMOTION and the Wear-Processor in predicting the wear of rolling-sliding contact can be seen in Fig. 2.11 [46].

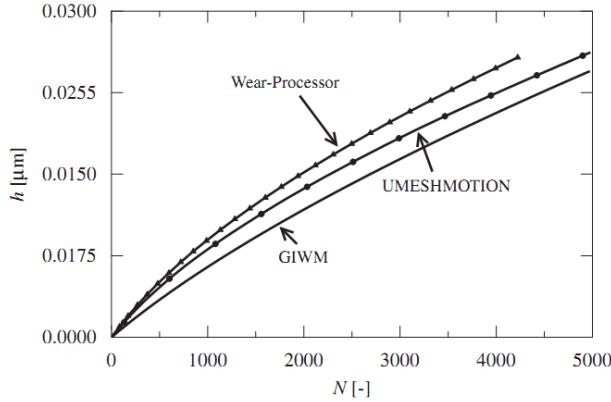


**Figure 2.11:** Wear depth as a function of number of overrollings. Comparison between GIWM model, UMESHMOTION and Wear-Processor, from Hegadekatte et al. [46].

#### 2.5.4 BEM wear model for a rolling-sliding contact

A wear simulation of 3D rolling-contact problems based on the boundary element method (BEM), was proposed by Rodríguez-Tembleque et al. [71].



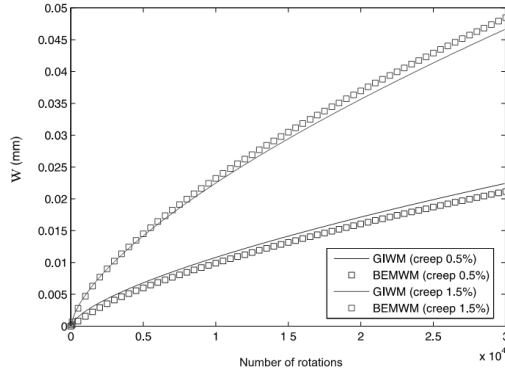


**Figure 2.12:** Wear depth as a function of the number of rotations. Comparison between BEM model and GIWM model, from Rodríguez-Tembleque et al. [71].

As constitutive equations of the potential contact zone Signorini's contact conditions were used, as well as Coulomb's law of friction, see also Aliabadi [72]. The material loss of the contacting bodies was predicted using the Archard's linear wear law. The methodology was applied to predict wear of different contact situations and compared with the GIWM results of Hegadekatte et al. [46]. A good agreement was obtained between the numerical calculations based on BEM and GIWM as shown in Fig. 2.12.

### 2.5.5 Model for running-in of rolling-sliding contact

Akbarzadeh and Khonsari proposed an analytical model using the load-sharing concept [73] and employed the model to investigate the running-in and the steady-state wear of rolling-sliding contacts for the mixed-EHL line contact problem [74]. In order to verify the model, they designed an experimental apparatus to investigate the transient wear process during the initial stage of contact. Seven experiments were conducted with five running-in experiments on fresh rollers and two steady-state experiments on run-in rollers. The results of the experiments are in good agreement with their model [76].

The load-sharing concept considers the total load on the contacting bodies to be carried partly by the hydrodynamic film  $F_H$  and partly by the asperities  $F_C$  as follows:

$$F_N = F_H + F_C \quad (2.18)$$

The contribution of each part is represented by scaling factors  $\gamma_1$  and  $\gamma_2$  so that

$$F_N = \frac{F_N}{\gamma_1} + \frac{F_N}{\gamma_2} \text{ and } 1 = \frac{1}{\gamma_1} + \frac{1}{\gamma_2} \quad (2.19)$$

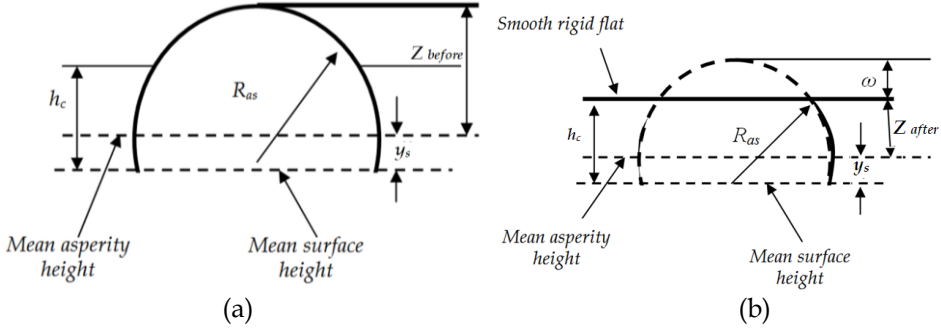


**Figure 2.13:** The plastic contact situation: (a) before contact and (b) after contact [21].

The load carried by the lubricant film determines the lubricant film thickness whereas the load carried by asperities determines the contribution to asperity deformation as schematically shown in Fig. 2.13. The indentation is defined by, Fig. 2.13b:

$$w = z - h_c + y_s \quad (2.20)$$

where  $z$  denotes the height of asperity,  $h_c$  is the central film thickness, and  $y_s$  is the distance between the mean of the asperity heights and the mean of the surface heights. The load carried by asperities,  $F_c$  is predicted by summing the contact load of elastic, elastic-plastic and fully-plastic deforming surfaces based on the contact model of Zhao et al. [21] as follows:

$$F_c = \sum_{i=1}^n F_{ei} + \sum_{i=1}^m F_{epi} + \sum_{i=1}^k F_{pi} \quad (2.21)$$

In which  $F_{ei}$ ,  $F_{epi}$  and  $F_{pi}$  are the loads carried by elastic, elastic-plastic and plastic deforming asperities  $i$  respectively.

Akbarzadeh and Khonsari [73] compared their simulation with the experimental investigation of Wang [75], as shown in Fig. 2.14. Comparison between Case 1 and Case 2 revealed that in Case 1, where the surfaces were smooth, steady state was reached faster and the drop in arithmetic average of asperity heights was smaller. Case 2, however, corresponded to the contact of rough surfaces, and larger changes in variation of  $Ra$  were observed. Figure 2.14

shows the proposed method by Akbarzadeh and Khonsari [73] in predicting the change in surface roughness by normal deformation only.

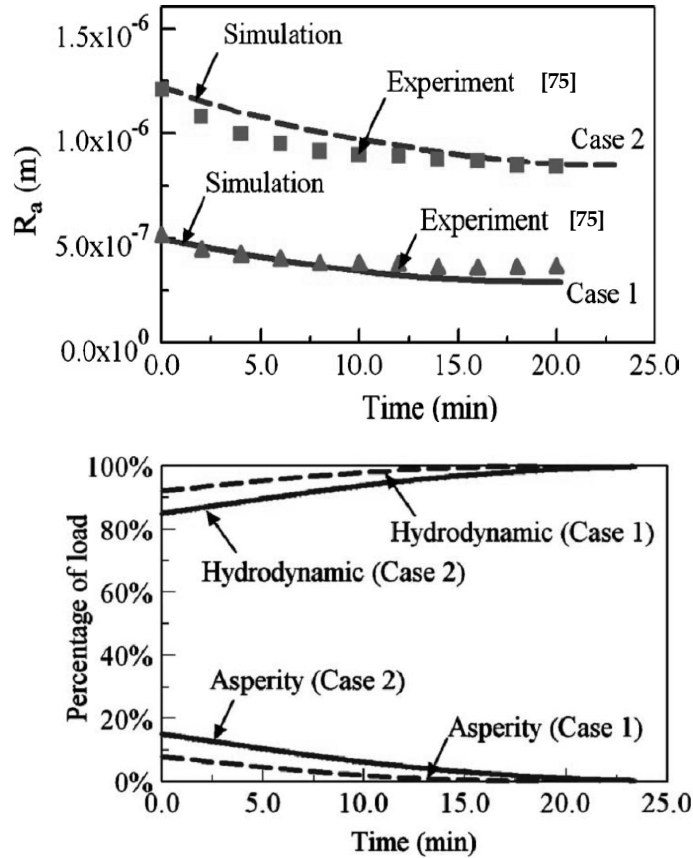


Figure 2.14: The comparison of Akbarzadeh and Khonsari's [73] model and experimental investigation of Wang [75].

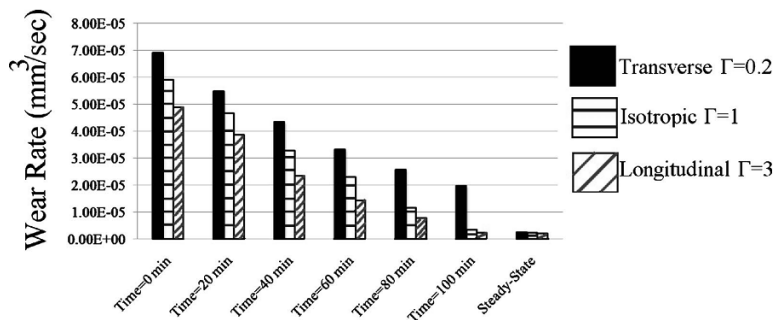
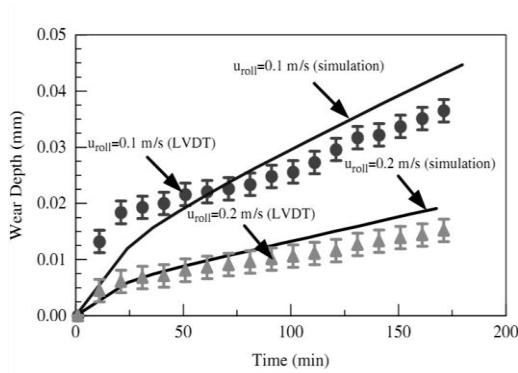
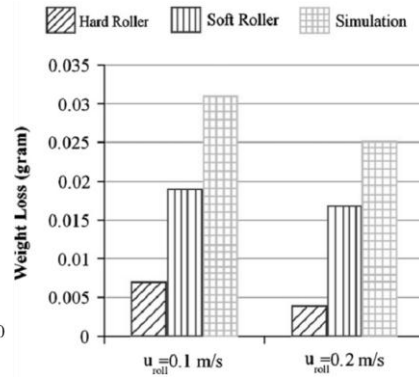


Figure 2.15: The evolution of wear rate on the running-in phase to the steady-state phase for three different surface patterns [73].

They also studied the evolution of wear for textured surfaces (transverse, isotropic and longitudinal oriented asperities in sliding direction) during running-in as plotted in Fig. 2.15. Initially, the wear volume per unit time shows a high value and as the running-in time proceeds it decreases until its variation with time becomes nil and the system attains a steady state. It was found that the transverse surface pattern has the highest wear rate.



**Figure 2.16:** The rolling velocity effect along running-in progress on wear depth [74].



**Figure 2.17:** The comparison of weight loss of the hard roller, soft roller and simulations [74].

Akbarzadeh and Khonsari [74] discussed the effect of the slide-to-roll ratio and the hardness of the material on the running-in of rolling-sliding contacts. It was found that an increase of the rolling velocity reduced the material losses and that the soft roller showed a higher wear compared to the hard roller as depicted in Figs. 2.16 and 2.17.

## 2.5.6 Rolling-sliding running-in experiments

Akbarzadeh and Khonsari [74] conducted a series of rolling-sliding running-in experiments where two of the running-in experiments were conducted on two pairs of rollers which have a clear distinction in terms of hardness (hard roller vs. soft roller), whereas the other two experiments were conducted with rollers which have only a slight difference in hardness (hard roller vs. hard roller). These running-in experiments showed the effect of material hardness and rolling velocity,  $u_{roll}$ , on the running-in behaviour of the contacting rollers. Another running-in experiment was performed which was stopped every 10 minutes. The soft roller was then cleaned with acetone and the weight and surface roughness of the roller were recorded. Then, the roller was again mounted and the test was continued for another 10 minutes. The weight loss and the change of the surface

roughness ( $R_a$ ) of the hard and soft roller varied as a function of the rolling speed and are depicted in Figs. 2.18 and 2.19. The figures show that most of the wear occurs at the soft roller. A better lubricant film was obtained with the higher rolling speed  $u_{roll} = 0.2$  m/s and therefore the amount of weight loss is lower, compared to the lower rolling speed,  $u_{roll} = 0.1$  m/s. A comparison of the surface roughness before and after an experiment is shown in Fig. 2.19.

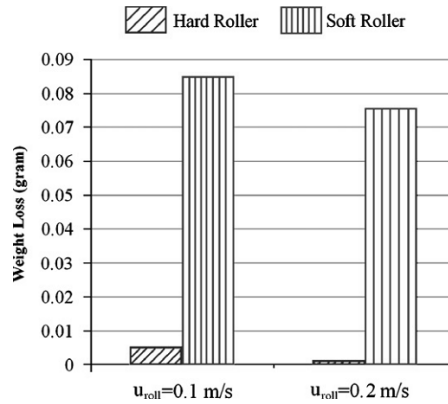


**Figure 2.18:** Weight loss as a function of rolling velocity, after [74].

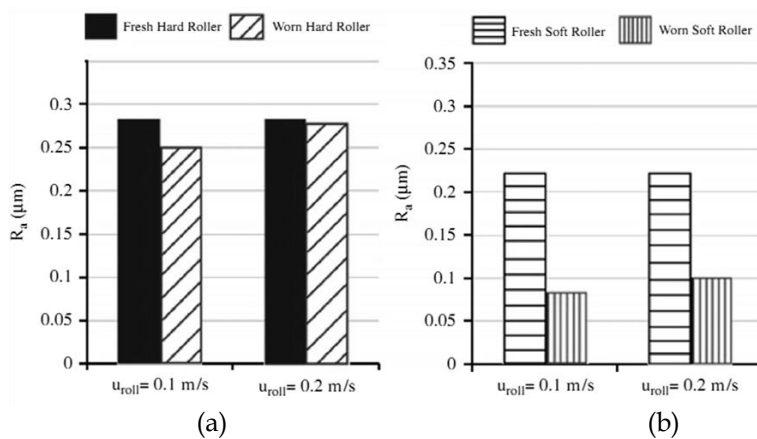


**Figure 2.19:** Surface roughness as a function of rolling velocity for (a) hard roller (b) soft roller before and after an experiment [74].

All tests showed a similar trend, with a higher material loss on the (slightly) softer rollers. The last experiment showed a striking increase in wear and a significant decrease in roughness at the initial stage of the experiment followed by a smaller decrease of surface roughness until the running-in process is completed and the steady-state regime starts. The simulations predicted the final value for surface

roughness fairly accurately. The evolution of surface roughness during running-in is shown in Fig. 2.20 whereas the evolution of wear (weight) is shown in Fig. 2.21.

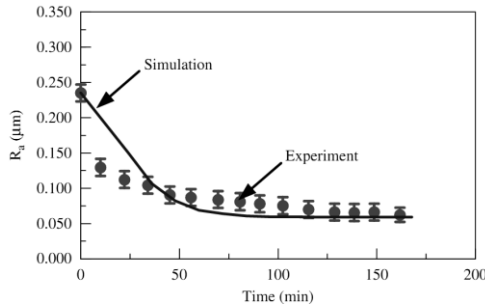


**Figure 2.20:** Surface roughness evolution during running-in. Comparison of experiment and model [74].

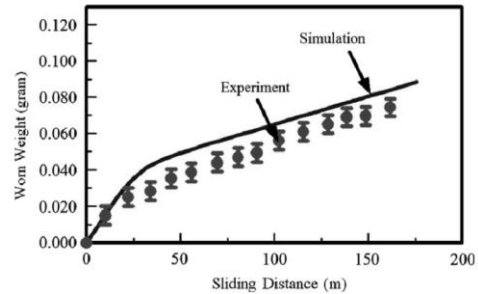


**Figure 2.21:** The worn weight comparison of experiment and simulation during running-in [74].

## 2.6 Concluding Remarks

A literature review of the running-in phenomena in various contact situations (sliding contact, rolling contact and rolling-sliding contact) has been conducted. The following have been observed:

1. The running-in phase of a rolling-sliding contact is usually studied analytically, numerically, statistically and experimentally, where the studied parameters mainly focus on material loss or wear depth, the change in surface roughness, coefficient of friction and contact pressure. The transition of the running-in phase to the steady-state phase is determined based on the parameters mentioned.
2. For the sliding contact situation, the models of running-in were most frequently derived on the basis of the well-known Archard's wear equation.
3. The models for running-in of sliding contacts were dominated by statistically based analysis e.g. using a Gaussian distribution of the surface roughness. Recently, a new model based on the equivalent plastic strain and the von Mises yield stress criterion was proposed [17].
4. The prediction of running-in phenomena of a rolling contact was proposed by considering the ellipsoid contact model and a deterministic description of a rough surface. Surface topographical changes during running-in of a rolling contact were predicted fairly accurately
5. The running-in of lubricated rolling-sliding contacts can be modelled by applying a load sharing concept: splitting the applied load into the load carried by the interacting asperities and the load carried by the lubricant. The parameters for running-in of a rolling-sliding contact, such as the

effect of material hardness, rolling speed, slide-to-roll ratio and initial surface roughness, have been discussed and compared with experiments. It is found that the running-in model has a reasonable fit with the conducted experiments. However, the change in surface topography obtained is based on deformation in normal direction only, no wear is taken into account.

The literature discussed above on running-in focussed on the macroscopic change of rolling and sliding contacts, i.e. mass loss and wear depth. Further, a statistical approach is used to predict the change in  $R_a$  of the surface topography. Systems become smaller and therefore the change in surface geometry and in particular the change in micro-geometry become of importance. Therefore, to study the running-in of rolling/sliding contacts a deterministic model approach, rather than a statistical approach, has to be followed as Jamari did for the rolling contact situation [3]. For the rolling/sliding contact situation this has not been done yet.

In order to study the running-in of rolling-sliding contacts, a FEM based model will be developed to be able to study the running-in phase on roughness level as well as the transition of the running-in phase to the steady-state phase by investigating the geometrical changes and the contact stresses for the rolling contact, sliding contact and rolling-sliding contact situation, as shown in Fig. 2.22.

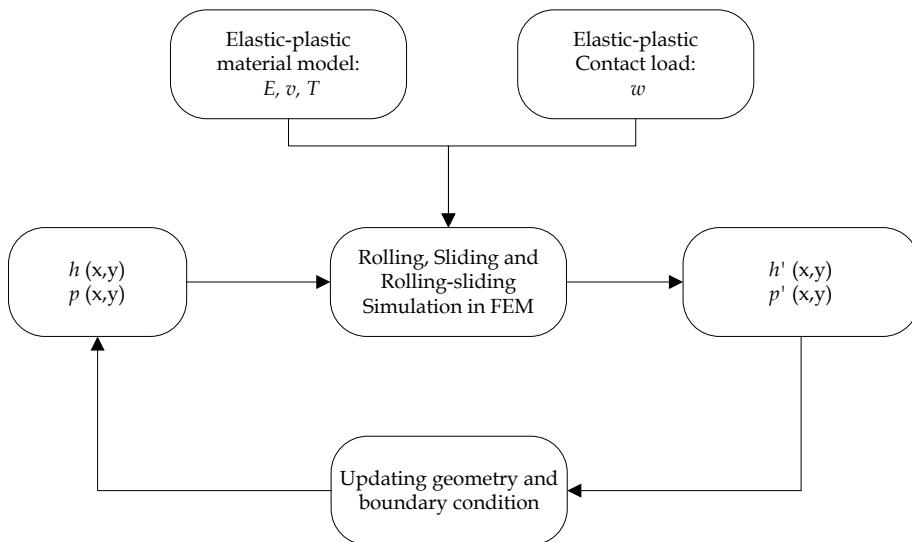


**Figure 2.22:** Proposed research on running-in of rolling-sliding contacts using FEM,  $h(x,y)$  is the initial surface geometry and  $h'(x,y)$  is the run-in surface geometry whilst  $p(x,y)$  is the initial contact pressure and  $p'(x,y)$  the contact pressure of the run-in surface.

## References

- [1] Blau, P.J., 1989, *Friction and Wear Transitions of Materials: Break-in, Run-in, Wear-in*, Noyes Publications, Park Ridge, NJ, USA.
- [2] Lin, J.Y. and Cheng, H.S., 1989, "An analytical model for dynamic wear," *ASME Journal of Tribology*, 111, pp. 468-474.
- [3] Jamari, J., 2006, *Running-in of Rolling Contacts*. PhD Thesis, University of Twente, Enschede, The Netherlands.
- [4] Johansson, S., Nilsson, P.H., Ohlsson, R., Anderberg, C. and Rosen, B-G., 2008, "New cylinder liner surfaces for low oil consumption," *Tribology International*, 41, pp. 854-859.
- [5] Whitehouse, D.J., 1980, "The effect of surface topography on wear," In: *Fundamentals of Tribology*, Suh and Saka (Ed.), The MIT Press, Massachusetts, USA, pp. 17-52.
- [6] Hsu, S.M., Munro, R.G., Shen, M.C. and Gate, R.S., 2005, "Boundary lubricated wear," In: *Wear, Materials, Mechanisms & Practice*, G.W. Stachowiak (Ed.), John Wiley & Sons Inc., London, UK, pp. 37-69.
- [7] Summer-smith, J.D., 1997, *A Tribology Casebook*, Mechanical Engineering Publications Limited, London, UK.
- [8] Kehrwald, B., 1998, *Einlauf Tribologischer Systeme*, Ph.D. Thesis, University of Karlsruhe. (in German).
- [9] Kalker, J.J., 1990, *Three-dimensional Elastic Body in Rolling Contact*, Kluwer Academic Publishing, Dordrecht, The Netherlands.
- [10] Johnson, K.L., 1985, *Contact Mechanics*, Cambridge University Press, Cambridge, UK.
- [11] Halling, J., 1976, *Introduction to Tribology*, Wykeham Publication Ltd., London. UK.
- [12] Bhargava, V., Hahn, G.T. and Rubin, C.A., 1985, "An elastic plastic finite element model of rolling contact, part 1: analysis of single contacts," *ASME Journal of Applied Mechanics*, 52, pp. 67-74.
- [13] Kulkarni, S., Hahn, G.T., Rubin, C.A. and Bhargarva, V., 1990, "Elasto-plastic finite element analysis of three-dimensional pure rolling contact above the shakedown limit," *Journal of Applied Mechanics*, 58, pp. 347-353.
- [14] Kulkarni, S., Hahn, G. T., Rubin, C. A., and Bhargarva, V., 1991, "Elasto-plastic finite element analysis of repeated three-dimensional, elliptical rolling contact with rail wheel properties," *ASME Journal of Tribology*, 113, pp. 434-441.
- [15] Jiang, Y., Xu, B. and Sehitoglu, H., 2002, "Three-dimensional elastic-plastic stress analysis of rolling contact," *ASME Journal of Tribology*, 124, pp. 699-708.
- [16] Xu, B. and Jiang, Y., 2002, "Elastic-plastic finite element analysis of partial slip rolling contact," *ASME Journal of Tribology*, 124, pp. 20-26.




- [17] Jacq, C., Nélias, D., Lormand, G. and Girodin, D., 2002, "Development of a three-dimensional semi-analytical elastic-plastic contact code", *ASME Journal of Tribology*, 124, pp. 653-667.
- [18] Nelias D., Antaluca E. and Boucly, V., 2007, "Rolling of an elastic ellipsoid upon an elastic-plastic flat," *ASME Journal of Tribology*, 129, pp. 791-800.
- [19] Jamari, J. and Schipper, D.J., 2006, "An elastic-plastic contact model of ellipsoid bodies," *Tribology Letters*, 21 (3), pp. 262-271.
- [20] Jamari, J. and Schipper, D.J., 2008, "Deterministic repeated contact of rough surfaces," *Wear*, 264, pp. 349-358.
- [21] Zhao, Y., Maietta, D.M. and Chang, L., 2000, "An asperity microcontact model incorporating the transition from elastic deformation to fully plastic flow *ASME Journal of Tribology*, 122, pp. 86-93.
- [22] Taşan, Y.C., de Rooij, M.B. and Schipper, D.J., 2007, "Changes in the microgeometry of a rolling contact," *Tribology International*, 40, pp. 672-679.
- [23] Taşan, Y.C., 2005, *Measurement of Deformation in Rolling and Sliding Contacts*, PhD Thesis, University of Twente, Enschede, The Netherlands.
- [24] Meng, H.C. and Ludema, K.C., 1995, "Wear models and predictive equation, their form and content," *Wear*, 443, pp. 181-183.
- [25] Hsu, S.M., Shen, M.C. and Ruff, A.W., "Wear prediction for metal," *Tribology International*, 30, pp. 377-383.
- [26] Holm, R., 1938, "The friction force over the real area of contact", *Wiss. Veroff. Siemens-Werk*, 17 (4), pp. 38-42. (in German).
- [27] Archard, J.F., 1953, "Contact and rubbing of flat surfaces," *Journal of Applied Physics*, 24, pp. 981-988.
- [28] Dorinson, A. and Broman, V.E., 1961, "Contact stress and load as parameter in metallic wear," *Wear*, 4, pp. 93-110.
- [29] Richard, R.C.D., 1967, "The maximum hardness of strained surface and the abrasive wear of metals and alloys," *Wear*, 10, pp. 353-382.
- [30] Hirst, W. and Lancaster, J.K., 1956, "Surface film formation and metallic wear," *Journal of Applied Physics*, 27, pp. 1057-1065.
- [31] Podra, P., 1997, *FE Wear Simulation of Sliding Contacts*, PhD thesis, Royal Institute of Technology (KTH), Stockholm, Sweden.
- [32] Flodin, A. and Andersson, S., 1997, "Simulation of mild wear in spur gears," *Wear*, 207, pp. 16-23.
- [33] Podra, P. and Andersson, S., 1999, "Simulating sliding wear with finite element method," *Tribology International*, 32, pp. 71-81.
- [34] Olofsson, U., Andersson, S. and Bjorklund, S., 2000, "Simulation of mild wear in boundary lubricated spherical roller thrust bearings," *Wear*, 241, pp. 180-185.
- [35] Flodin, A. and Andersson, S., 2000, "Simulation of mild wear in helical gears," *Wear*, 241, pp. 123-128.
- [36] Oqvist, M., 2001, "Numerical simulations of mild wear using updated geometry with different step size approaches," *Wear*, 249, pp. 6-11.

- [37] Ko, D.C., Kim, D.H. and Kim, B.M., 2002, "Finite element analysis for the wear of Ti-N coated punch in the piercing process," *Wear*, 252, pp. 859-69.
- [38] McColl, I.R., Ding J. and Leen S., 2004 "Finite element simulation and experimental validation of fretting wear," *Wear*, 256, pp. 1114-27.
- [39] Ding, J., Leen, S.B. and McColl I., 2004, "The effect of slip regime on fretting wear-induced stress evolution," *International Journal of Fatigue*, 26, pp. 521-531.
- [40] Gonzalez C., Martin, A., Garrido, M.A., Gomez, M.T., Rico, A. and Rodriguez J., 2005, "Numerical analysis of pin on disc tests on Al-Li/SiC composites," *Wear*, 259, pp. 609-612.
- [41] Mukras, S., Kim, N.H., Sawyer, W.G., Jackson, D.B. and Bergquist, L.W., 2009, "Numerical integration schemes and parallel computation for wear prediction using finite element method," *Wear*, 266, pp. 822-831.
- [42] Johnson, K.L. and Shercliff, H.R., 1992, "Shakedown of 2-D asperities in sliding contact," *Int. Journal of Mech. Sci.* 34, pp. 375-394.
- [43] Kapoor, A. and Johnson, K.L., 1994, "Plastic ratcheting as a mechanism of metallic wear," *Proc. R. Soc. London A*, 445, pp. 367-381.
- [44] Hegadekatte, V., 2006, *Modeling and Simulation of Dry Sliding Wear for Micro-machine Applications*, PhD thesis, University of Karlsruhe, Karlsruhe, Germany.
- [45] Hegadekatte, V., Huber, N. and Kraft, O., 2006, "Modeling and simulation of wear in a pin on disc tribometer," *Tribology Letters*, 24, pp. 51-60.
- [46] Hegadekatte, V., Kurzenhauser, S., Huber, N. and Kraft, O., 2008, "A predictive modeling scheme for wear in tribometers," *Tribology International*, 41, pp. 1020-1031.
- [47] Kanavalli B., 2006, *Application of user defined subroutine UMESHMOTION in ABAQUS to simulate dry rolling/sliding wear*. Master thesis, Royal Institute of Technology (KTH), Stockholm, Sweden.
- [48] Hertz, H., 1882, "Ueber die beruehrung fester elastischer koerper," *J Reine Angew. Math.*, 92, pp. 156-71. (in German).
- [49] Oliver, W.C. and Pharr, G.M., 1992, "An improved technique for determining hardness and elastic modulus using load and displacement sensing indentation experiments," *J. Mater. Res.*, 7, pp. 1564-83.
- [50] Jeng, Y.R., Lin, Z.W. and Shyu, S.H., 2004, "Changes of surface topography during running-in process," *ASME Journal of Tribology*, 126, pp. 620-625.
- [51] Stout, K.J., Whitehouse, D.J. and King, T.G., 1977, "Analytical techniques in surface topography and their application to a running-in experiment," *Wear*, 43, pp. 99 - 115.
- [52] King, T.G., Watson, W. and Stout, K.J., 1978, "Modelling the micro-geometry of lubricated wear," *Proc. 4th Leeds-Lyon Symposium*, pp. 333-343, London, UK.
- [53] Sugimura, J., Kimura, Y. and Amino, K., 1987, "Analysis of the topography changes due to wear-geometry of the running-in process," *JSLE*, 31 (11), pp. 813-820.

- [54] Lin, J.-Y. and Cheng, H.S., 1989, "An analytical model for dynamic wear," *ASME Journal of Tribology*, 111, pp. 468-474.
- [55] Hu, Y.Z., Li, N. and Tonder, K., 1991, "A dynamic system model for lubricated sliding wear and running-in," *ASME Journal of Tribology*, 113, No. 3, pp. 499-505.
- [56] Ruff, A.W., Ivest, L.K. and Glaeser, W.A., 1981, "Characterization of wear surface and wear debris," In: *Fundamentals of Friction and Wear of Materials*, Rigney, D.A. (Ed.), ASM, pp. 235-289.
- [57] Stout, K.J., Watson, W. and King, T.G., 1980, "The micro-geometry of lubricated wear-classification and modeling," In: *Fundamentals of Tribology*, Suh and Saka (Ed.), MIT press, pp. 83-99.
- [58] Shirong, G. and Gouan, C., 1999, "Fractal prediction models of sliding wear during the running-in process," *Wear*, 231, pp. 249-255.
- [59] Zhu, H., Ge, S., Cao, X. and Tang W., 2007, "The change of fractal dimension of frictional signals in the running-in wear process," *Wear*, 263, pp. 1502-1507.
- [60] Liang, X., Kaiyuan, J., Yongqing, J. and Darong, C., 1993, "Variations in contact stress distribution of real rough surfaces during running-in," *ASME Journal of Tribology*, 115, pp. 602-606.
- [61] Liu, Z., Neville, A. and Reuben, R.L., 2001, "Analyzing elastic-plastic real rough surface contact in running-in," *Tribology Transactions*, 44, pp. 428-436.
- [62] Wang, W., Wong, P.L. and Zhang, Z., 2000, "Experimental study of the real time in surface roughness during running-in for PEHL contacts," *Wear*, 244, pp. 140-146.
- [63] Kumar, R., Prakash, B. and Sethuramiah, A., 2002, "A systematic methodology to characterize the running-in and steady-state processes," *Wear*, 252, pp. 445-453.
- [64] Nélías, D., Bounicy, V. and Brunet, M., 2006, "Elastic-plastic contact between rough surface: proposal for a wear or running-in model," *ASME Journal of Tribology*, 128, pp. 236-243.
- [65] Oila, A. and Bull, S.J., 2005, "Assessment of the factors influencing micropitting in rolling/sliding contacts," *Wear*, 258, pp. 1510-1524.
- [66] Bosman, R. and Schipper, D.J., 2010, "Running-in of systems protected by additive-rich oils", *Tribology Letters*, 41, pp. 263-282.
- [67] Blau, P.J., 1981, "Interpretations of the friction and wear break-in behaviour of metal in sliding contact," *Wear*, 71, pp. 29-43.
- [68] Dienwiebel, M. and Pohlmann, K., 2007, "Nanoscale evolution of sliding metal surface during running-in," *Tribology Letters*, 27, pp. 255-260.
- [69] Umeda, A., Sugimura, J. and Yamamoto, Y., 1998, "Characterization of wear particles and their relationship with sliding conditions," *Wear*, 216, pp. 220-228.
- [70] Yuan, C.Q., Peng, Z., Yan, X.P. and Zhou, X.C., 2008, "Surface evolutions in sliding wear process," *Wear*, 265, pp. 341-348.

- [71] Rodríguez-Tembleque, L., Abascal, R. and Aliabadi, M.H., 2010, "A boundary element formulation for wear modeling on 3D contact and rolling-contact problems," *Int. Journal of Solids and Structures*, 47, pp. 2600–2612.
- [72] Aliabadi, M.H., 2002, "*The Boundary Element Method, Applications in Solids and Structures 2*," John Wiley & Sons, USA.
- [73] Akbarzadeh, S. and Khonsari, M.M., 2010, "On the prediction of running-in behaviour in mixed-lubrication line contact, *ASME Journal of Tribology*, 132, pp. 1-11.
- [74] Akbarzadeh, S. and Khonsari, M.M., 2011, "Experimental and theoretical investigation of running-in, *Tribology International*, 44, pp. 92-100.
- [75] Wang, W., Wong, P. L. and Guo, F., 2004, "Application of partial elastohydrodynamic lubrication analysis in dynamic wear study for running-in," *Wear*, 257, pp. 823–832.

CHAPTER  
3



## Running-in of Rolling Contacts

---

### 3.1 Introduction

The running-in phase is a transient phase where many parameters seek their stabilized form. During running-in the system adjusts to reach a steady-state condition between contact pressure, surface roughness, interface layers and the establishment of an effective lubricating film at the interface. These adjustments may cover surface conformity, oxide film formation, material transfer, lubricant reaction products, martensitic phase transformations and subsurface microstructure reorientation [1]. The running-in phase is followed by a steady-state phase which is defined as the condition of a given tribo-system in which the average dynamic coefficient of friction, the specific wear rate, and other specific parameters have reached and are maintaining a relatively constant level [2].

Running-in takes place during the initial use of rolling components such as gears and bearings. A successful running-in phase contributes to enhancing the degree of conformity so that the performance of the contacting components improves whereas the failure of the running-in phase, indicated by the failure in attaining the degree of conformity, causes failure of the contacting components during initial usage. The significance of running-in has been discussed in the previous chapter.

Considering the aforementioned significance of the running-in phase, the study of the running-in of rolling contacts becomes important due to the wide application of rolling contact elements such as gears and bearings. Jamari [3] researched the running-in of rolling contacts by modelling (local) elastic-plastic deformation, which results in a topographical change of an engineering surface. He proposed a deterministic model [4] based on the elastic-plastic ellipsoid contact model [5] to predict the plastic deformation of the higher asperities, decreasing the

centre line average roughness,  $R_a$  and change in surface topography [3]. The analytical model has been validated with a number of experiments, where good agreements were obtained.

This chapter is based on the work of Jamari on the running-in of rolling contacts [3]. A finite element simulation was carried out to model the topographical change of a two dimensional rough surface when a rigid cylinder repeatedly rolls over it. The modelling of the geometry (plastic deformation), contact stress and residual stress were used as indicators of the end of the running-in phase and the early stage of the steady-state phase.

This chapter contains six sections. Section 3.2 deals with the repeated static contact simulation. Before starting the simulation on rough surfaces, a validation of the contact model was conducted by comparing finite element results of the contact model with the analytical calculations. Then the discussion is continued on the rolling contact of a cylinder on a flat surface in Section 3.3. This section discusses plastic deformation, contact stresses and residual stresses of the deformable flat surface when a rigid cylinder rolls over the surface at various contact loads. Section 3.4 explores the model of the running-in phase of the repeated rolling contact between a cylinder and a rough surface. Section 3.5 studies the FE model on the running-in of a rigid ball rolling on a real rough surface. The chapter closes with some concluding remarks on the findings obtained with finite element simulations on the running-in of rolling contacts.

## 3.2 Simulation of repeated static contact

As reported in the literature study, only a limited number of publications discuss the use of finite element simulations in modelling running-in of rolling contacts. Therefore, some initial investigations should be conducted in order to check whether the finite element model and its procedures are such that the simulation is able to address the running-in problem of rolling contacts. In this section, both a single static contact and a repeated static contact were simulated to check the contact model, the simulation procedure, and the element sensitivity by comparing the present simulation with previous works on finite element analysis as well as analytical solutions.

### 3.2.1 Single static contact model

The finite element analysis was initiated by simulating a single static contact between a two dimensional rigid indenter and an elastic flat surface, using the commercial finite element software ABAQUS. A non-deformable cylinder, with a cylinder radius,  $R_{cyl}$ , of 4.76 mm, was pressed with a normal force per unit length ( $F_N/l$ ) of 27 N/mm against an elastic deforming flat body with a size of 10 x 20 mm

in  $x$  and  $z$  direction as depicted in Fig. 3.1. Both the cylinder and the flat body were assumed to show plane strain behaviour. The material of the flat surface is aluminium with an elastic modulus ( $E$ ) of 70 GPa and a Poisson's ratio ( $\nu$ ) of 0.32.

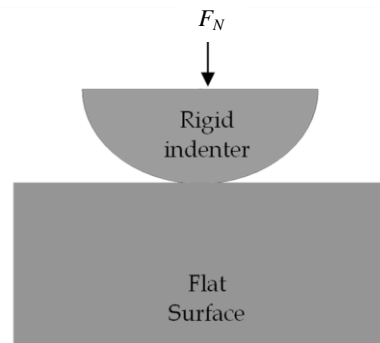


**Figure 3.1:** Single static contact between a cylinder and a flat surface.

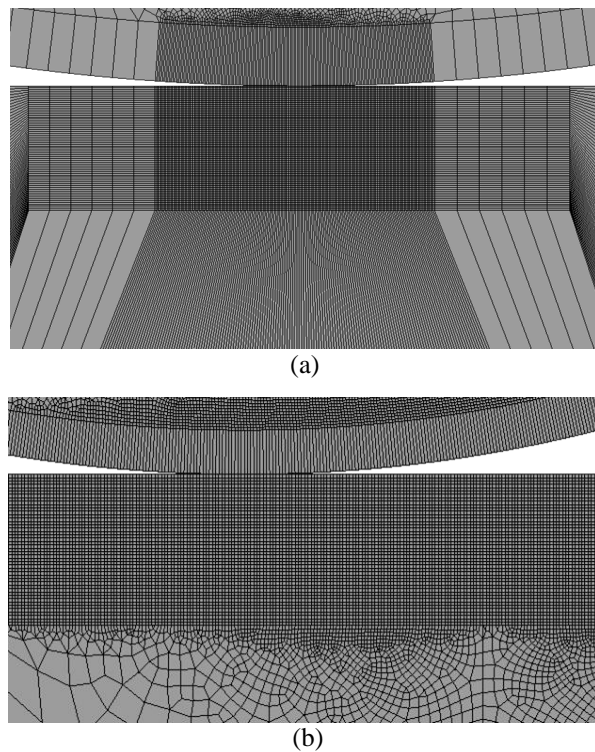


**Figure 3.2:** The mesh: (a) mesh type 1: arranged manually and (b) mesh type 2: generated automatically by the FE software.

A four nodes element was used in the FE model and a refined mesh was applied in and near the contact. For the flat surface, two types of mesh arrangements, as seen in Fig. 3.2, were generated to check the mesh sensitivity during contact and the error within the results. The first mesh (Fig. 3.2a) was generated manually by managing the mesh distribution and controlling the element length. The second mesh (Fig. 3.2b) was generated automatically by the software, the arrangement of the mesh was managed by ABAQUS whilst the limitation was designed by determining the element length and the location of the mesh refinement. Both mesh types have the same element length in and near the contact.

### 3.2.2 FE contact calculations

#### 3.2.2.1 Elastic contact on a flat surface

For the proposed static contact model, the results of the FEA of the elastic contact situation were validated with the analytical solution of Hertz [6] by comparing the maximum contact pressure ( $p_0$ ), the contact half width ( $b$ ) and the contact pressure distribution. A series of simulations, applying the previous 2D contact model, have been conducted for determining the accuracy of the numerical results by considering the mesh length. The static contact model employed several mesh lengths, namely  $0.5 R_{cyl}$ ,  $0.1 R_{cyl}$ ,  $0.05 R_{cyl}$ ,  $0.01 R_{cyl}$  and  $0.005 R_{cyl}$  where  $R_{cyl}$  is the cylinder radius. The contact pressure and the contact half width were obtained from the FEA results when the maximum contact load was applied. A deviation above 5 % was found for the mesh lengths of  $0.5 R_{cyl}$ ,  $0.1 R_{cyl}$  and  $0.05 R_{cyl}$  while the mesh lengths of  $0.01 R_{cyl}$ , and  $0.005 R_{cyl}$  show an error below 5%. The results did not give a clear distinction for the last two mesh lengths and then, with regard to computational time for a FE simulation, the mesh length of  $0.01 R_{cyl}$  was chosen. This mesh length will be utilized in the next finite element simulations for validating the arrangement of the mesh.

**Table 3.1:** Comparison between the analytical and numerical simulation using two types of mesh.

Name of parameters	Analytic (Hertz)	Mesh 1 (Manual)	Mesh 2 (Automatic)
$b_c$ (mm)	0.0463	0.0469	0.0469
$p_o$ (MPa)	382.16	381.77	381.52

After checking the element length, the next FE model validation is conducted for two mesh types (type 1 and type 2). The two mesh types as explained previously were applied to the flat surface of the FE contact model and a static simulation was conducted. Figure 3.3 and Table 3.1 describe the comparison between the analytical model with FEA-mesh 1 and FEA-mesh 2 where the mesh



length is  $0.01 R_{cyl}$ . A good agreement was found between the analytical solution and the FEA.

The conclusion reached by the model verification is that the present finite element model, mesh generation and simulation procedure is in good agreement with the Hertz analytical model for describing elastic contact. The manually managed mesh and the automatically generated mesh show no significant deviations. The results exhibit that both mesh types can be employed in simulations where the mesh length and mesh distribution should be taken into proper consideration. A larger mesh size produces a higher error while a too fine mesh size increases the computational time dramatically. Both mesh types are used in this chapter. Based on the investigation on the static contact and the rolling contact the manual mesh arrangement (mesh type 1) is suitable for the contact simulation with the flat surface, however, the automatically generated mesh (mesh type 2) is found to be more stable for the contact simulation with a rough surface (see section 3.5).

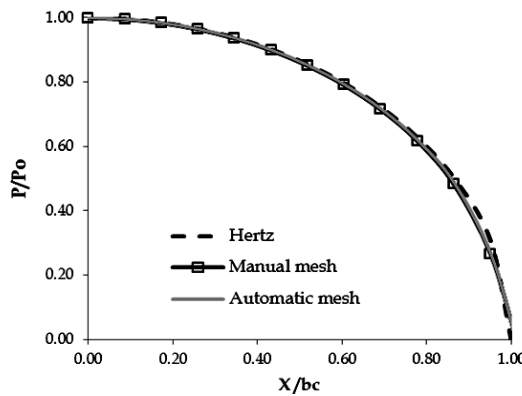


**Figure 3.3:** Comparison between analytical and numerical solution of the two mesh types on the normalized contact pressure  $p/p_0$  as a function of normalized distance  $x/b_c$ .

### 3.2.2.2 Elastic-plastic contact

After the validation of FEA for the elastic contact, the finite element contact model is also checked on the elastic-plastic contact situation. The critical interference,  $\omega_c$ , and the critical contact width  $b_c$  proposed by [7] for determining the yielding limit between the elastic and the elastic-plastic deformation of a line contact was used to verify the model. These equations, derived by using the distortion energy yield criterion of maximum von Mises stress, are defined as [7]:

$$\omega_c = R' \left( \frac{C\sigma_Y}{E'} \right)^2 \left[ 2 \ln \left( \frac{2E'}{C\sigma_Y} \right) - 1 \right] \quad (3.1)$$

$$b_c = \frac{2R'(C\sigma_Y)}{E'} \quad (3.2)$$

where  $C = 1.164 + 2.975\nu - 2.906\nu^2$ ,  $\sigma_Y$  is the yield stress of the material,  $R'$  is the equivalent radius of the contacting bodies,  $E'$  is the equivalent elastic modulus and  $\nu$  is the Poisson's ratio.

The 2D FE model of a cylinder versus a flat surface, as described in the previous section with mesh type 1, was used in this simulation with elastic-plastic material behaviour showing strain hardening. This material model is preferred over an elastic-perfectly plastic model, as the latter has been found to deviate from experimental results, see Bijak-Zachowski and Marek [8].

The elastic-plastic material behaviour with strain hardening for the flat surface was modelled based on the investigation of Bhowmik [9] on aluminium where the mechanical properties i.e. the elastic modulus ( $E$ ), yield stress ( $\sigma_Y$ ), and Poisson's ratio ( $\nu$ ) were 70 GPa, 270 MPa and 0.32, respectively. The cylinder was modelled as a rigid body where no deformation occurs during static contact.

In simulating the contact problem, two methods of input were used. The first applies a force to one body and then computes the resulting displacement. The second applies a displacement and then computes the resulting contact force. In both methods, the displacement, stress and strain in the elastic and elastic-plastic deforming body can be determined as well as the contact pressure. The simulations performed showed that the convergence of the displacement controlled method was much faster and therefore the interference is used in modelling the contact load [4, 10-11].

The critical interference,  $\omega_c$ , calculated with Eq. (3.1), was applied as input into the FEA of a cylinder on a flat surface. The finite element simulation produces the contact half width which can be compared with the analytical solution (Eq. 3.2) and the equivalent von Mises stress from the FEA can be compared with the yield stress in predicting the transition limit of the elastic to elastic-plastic deformation situation.

Table 3.2 shows the comparison between the prediction of the analytical model and the numerical simulation of a single static contact. The analytical result of the critical interference and contact width in this case are  $5.98 \times 10^{-2}$  mm and  $5.99 \times 10^{-2}$  mm, respectively. By applying the critical interference of the analytical solution, the deviation of the FE calculated contact width and the maximum von Mises stress are 0.13% and 2.93%, respectively.

**Table 3.2:** Comparison between the analytical model and the numerical simulation of the present FE model.

Contacting Bodies	$b_c$ analytically (mm)	$b_c$ numerical (mm)	Yield stress of material model (MPa)	Max von Mises stress numeric (MPa)
Cylinder vs flat surface	$5.99 \times 10^{-2}$	$5.98 \times 10^{-2}$	270	262.1
Difference in the results	0.13 %		2.93 %	

The conclusion is that the present finite element model, mesh generation, and simulation procedure are in good agreement with the analytical model in predicting the critical contact half-width and the maximum von Mises stress. The contact model of the rigid cylinder against a flat has been validated for elastic deformation and elastic-plastic deformation for a single normal loaded static contact. This contact model will be used in simulating the repeated static contact and will also be used in simulating the repeated rolling contact in the next section.

### 3.2.2.3 Elastic-plastic contact between two hemispheres

A three-dimensional FE simulation was conducted on the static contact between two hemispheres with a variety of radii. Figure 3.4 shows the general static contact situation. The purpose of the finite element simulation is observing the phenomena of the contact between two hemispheres with a high ratio of radii. This is because for rough surfaces, the local contact does not occur between asperities of the same size. The understanding of a realistic contact is required for developing a better contact model. Jamari [3] argued that the plastic deformation for sets of two contacting hemispheres with a different ratio of radii does not follow the hypothesis of Johnson and Shercliff [12] that when two contacting asperities have the same hardness, the depth of plastic deformation is expected to be the same for each body, independent of the geometries used.

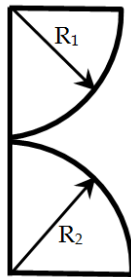


**Figure 3.4:** Variation in the ratio of radii  $R_1/R_2$  ranging from 1 to 7.

A number of finite element simulations and experiments (see appendix A) were conducted by contacting hemispheres with different ratio of radii. The result of the finite element simulations and the experiments are shown in Fig 3.5. It was found that the ratio of the amount of plastic deformation of the bodies in contact  $\omega_{p1}/\omega_{p2}$  decreases as the ratio of the radii of the bodies  $R_1/R_2$  increases. The body with a higher radius shows less plastic deformation than the body with a lower radius. Jamari [3] assumed that this is caused by material flow of the contacting bodies, where the body that has “free space” to transfer the material (laterally in this case) will show more plastic deformation. The results are explained further in appendix A. The calculation of the normalized contact pressure as a function of the normalized interference based on FEM also shows that by maintaining the normal load, an increase of the ratio of radii results in an increase of the contact pressure.

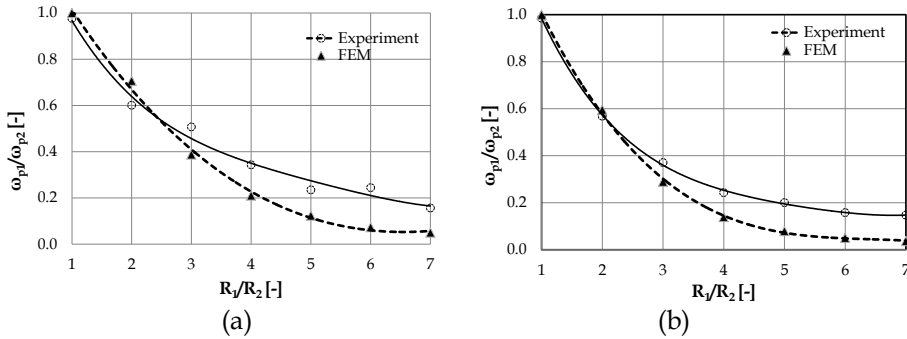


**Figure 3.5:** The comparison of the experimental investigation and finite element simulation of two contacting bodies with different ratio of the radii: (a) static normal force = 8000 N and (b) static normal force = 11000 N.

### 3.2.3 Repeated static contact on a flat surface

The static contact used previously, i.e. a cylinder against a flat, will now be used for investigating the effect of repeated loading on the plastic deformation, contact stress and residual stress. In the loading phase, the cylinder is pressed normally for a specific interference on a flat surface, followed by the unloading phase where the cylinder is pulled back to its original position. The loading-unloading phase is repeated for five cycles. The material of the flat surface is assumed to behave elastic-plastic with strain hardening based on the Bhowmik [9] investigation, whilst the cylinder is assumed to be rigid. In this simulation, mesh type 1 with four node elements was used.

The normalized interference,  $\omega^*$ , is introduced to indicate the “severity of deformation” of the contact, which is defined as follows:

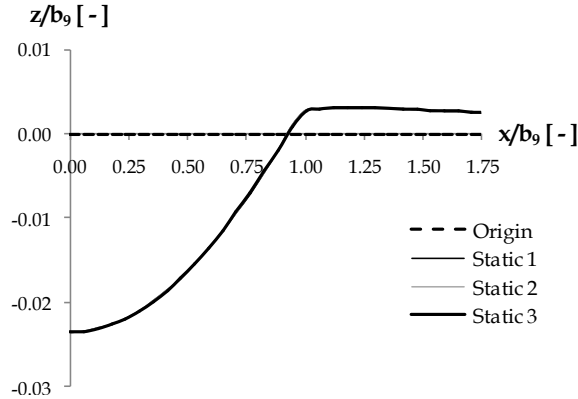
$$\omega^* = \frac{\omega}{\omega_c} \quad (3.3)$$

where  $\omega$  is the applied interference and the  $\omega_c$  is critical interference, calculated by Eq. (3.1). The normalized interference basically describes the degree of the elastic-plastic deformation. Zhao et al. [11] stated that elastic deformation occurred when  $\omega^* < 1$ , elastic-plastic deformation takes place when  $1 < \omega^* < 54$  and full plastic deformation when  $\omega^* > 54$ .

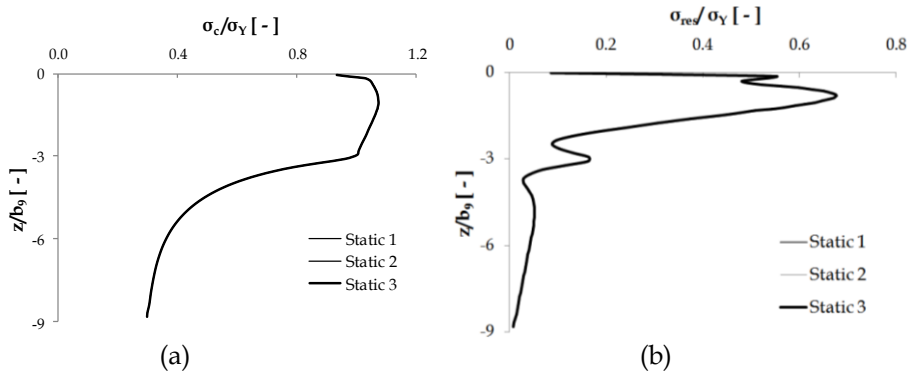
A value of  $\omega^* = 9$  was taken and five repetitions of static contact simulations, with the same interference, were performed. The results are depicted in Figs. 3.6 and 3.7. The result of the plastic deformation of the flat surface can be seen in Fig 3.6 where the normalized plastic deformation of the flat surface ( $z$  direction) is plotted as a function of the normalized  $x$  direction. The half contact width,  $b_9$ , calculated analytically using Eq. (3.2) for  $\omega^* = 9$ , is used to depict the non-dimensional deformation. Only the right half of the created indentation is shown, as it is symmetrical. It was found that the final contour of the indentation is obtained within the first three indentations. Pile-up arises on the edge of the contact area due to material flow.

Figure 3.7a depicts the normalized von Mises contact stress ( $\sigma_c / \sigma_Y$ ) as a function of the normalized depth in  $z$  direction ( $z/b_9$ ) while Fig. 3.7b depicts the normalized von Mises residual stress ( $\sigma_{res} / \sigma_Y$ ) as a function the normalized depth in  $z$  direction ( $z/b_9$ ). The von Mises contact stress,  $\sigma_c$ , was calculated during the maximum contact loading while the von Mises residual stress,  $\sigma_{res}$ , was calculated after unloading the contact. The von Mises yield stress criterion,  $\sigma_Y$ , is used to normalize the non-dimensional stress. These figures show that the first up until the third repeated static contact does not show a remarkable difference for the contact stress and residual stress. This fact shows that in elastic-plastic static contact, the first contact acts as the dominant factor in surface deformation. The modelling phase of the deformation and stress are found after the first contact. Kadin et al. [13] also found in their investigation on contact stress of a loaded and unloaded contact, in this case a rigid flat versus a deformable hemisphere, that the final deformation profile already occurred in the first or second loading cycle.

Next, a simulation of repeated static contact with the same model is conducted, however, using a different method of the input, i.e. the normal force input. The applied normal force has been calculated and is equivalent to  $\omega^* = 9$ . The simulation investigates the effect of the input on the finite element simulation by using the same model and numerical simulation procedure. The results of the topographical change, the contact stress and residual stress coincide for all repeated contacts from first to third repetition, similar to the behaviour shown in Figs. 3.6 and 3.7. The stability of the iteration and the convergence speed were better for the interference input so that the simulations on rolling contact are performed using the interference as input.



**Figure 3.6:** Deformation of the flat surface due to repeated static contact for  $\omega^* = 9$ .



**Figure 3.7:** Repeated static contact for  $\omega^* = 9$ : (a) normalized contact stress and (b) normalized residual stress.

### 3.3 Running-in of a rigid cylinder rolling on a smooth flat surface

#### 3.3.1 Contact model and simulation procedures

This section discusses the running-in of the rolling contact of a rigid cylinder over a smooth flat surface using the plain strain assumption. A free and frictionless rolling contact situation was assumed in this model. The rolling contact was repeated three times on the flat surface with a rolling distance of 15 mm. The dimensions and material properties of the cylinder and flat body are the same as those used for the repeated static contact and the aluminium behaves as an elastic-plastic. The cylinder was modelled as a non-deformable roller.

The simulation steps in the FE analysis, shown in Fig. 3.8, were conducted as follows: (a) the normal static contact was applied on the flat surface for interference  $\omega$ ; (b) by maintaining the vertical interference, the cylinder rolled

incrementally towards the right hand side until the final location on the flat surface is reached. The cylinder was then pulled up for unloading; (c) the rolling contact of the cylinder over the flat surface was repeated for three cycles in order to observe the transition of the running-in phase to the steady-state situation.

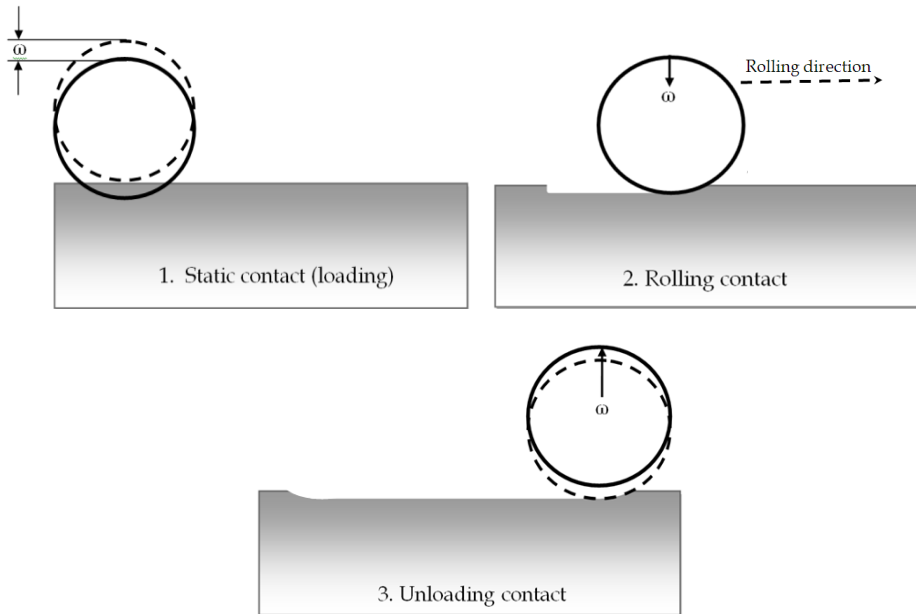


**Figure 3.8:** The schematic rolling contact simulation of a cylinder against a smooth flat.

The investigation of the rolling contact of a cylinder over a flat surface was conducted for four different interferences, i.e. at different loads. In order to demonstrate the effect of the interference on a rolling contact on the deformation of the flat surface, the interferences in this simulation are set larger than the critical interference, namely  $\omega^* = 1, 3, 6$  and  $9$  respectively, see Table 3.3. The critical interference was calculated using Eq. (3.1) for the contact of a cylindrical roller against a flat surface.

**Table 3.3:** The applied interference,  $\omega$  and the contact half width,  $b$ .

$\omega^*$	$\omega^* = 1$	$\omega^* = 3$	$\omega^* = 6$	$\omega^* = 9$
$\omega$ [mm]	0.00198	0.00594	0.01188	0.01782
$b$ [mm]	0.0698	0.1497	0.2499	0.3303

### 3.3.2 Validation of the FE simulation

Before conducting the simulations on running-in of a rolling contact on a flat surface, some initial simulations are performed to check the contact model and the simulation procedure. First, a comparison was made with the rolling contact model of Bhargava et al. [14-15]. The normalized contact pressure,  $p_0/k$  was used as input in the rolling contact simulation, where  $p_0$  is the maximum contact pressure, and  $k$  the yield shear strength of the softer material. Figures 3.9 and 3.10 depict the comparison of the present numerical simulation method and the results of Bhargava et al. [14]. The overall results agree, the minor differences between the two results are caused by limitations to the quasi-static approach of Bhargava et al. [14].

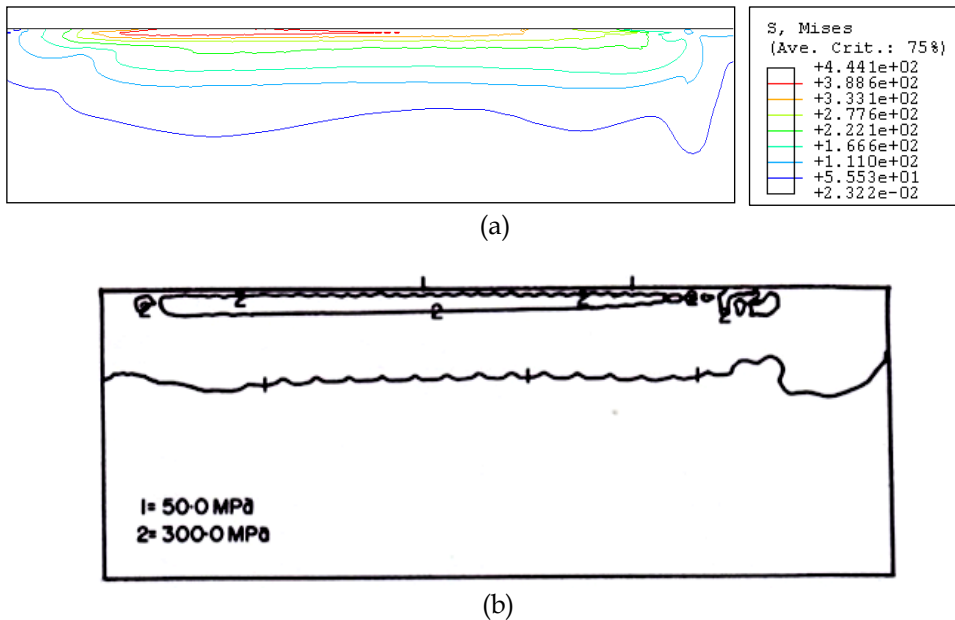


**Figure 3.9:** Comparison of the residual von Mises equivalent stress for  $p_0/k = 5$ .  
 (a) Present model and (b) Bhargava, et al. [14].



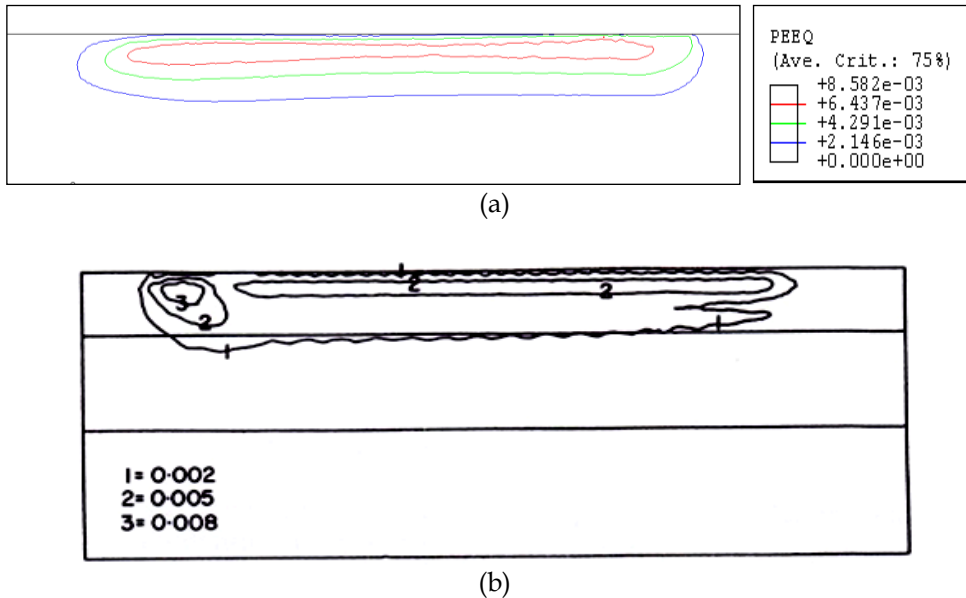


**Figure 3.10:** Comparison of the residual equivalent plastic strain for  $p_0/k = 5$ .  
 (a) Present model and (b) Bhargava, et al. [14].

### 3.3.3 Results and discussions

In contrast to Bhargava et al. [14-15], Nelias et al. [16], Kulkarni et al. [17] and Bijak-Zachowski and Marek [8] who used the contact pressure ( $p$ ) as input parameter, the present simulation uses the interference,  $\omega$ , as input to conduct the simulation. The critical interference,  $\omega_c$ , is used to normalize the results.

The results of these simulations are the von Mises contact stress distribution, the residual stress distribution and the plastic deformation of the flat surface for three overrollings. Figure 3.11a depicts the contact stress during initial static contact for  $\omega^* = 9$ . The highest interference is selected to show the stress distribution. The contact stress indicates that the deformation has reached the elastic-plastic regime, because the maximum von Mises stress arises at the contact surface. In the elastic deformation regime the maximum von Mises stress is located below the surface. Figure 3.11b describes the von Mises contact stress as the cylinder rolls over the flat. The von Mises residual stresses are visible on the left side of the contact where the contact has just passed that location. The von Mises contact stress and von Mises residual stress distribution as a function of depth will be discussed using the graphs calculated and presented in Fig. 3.12.

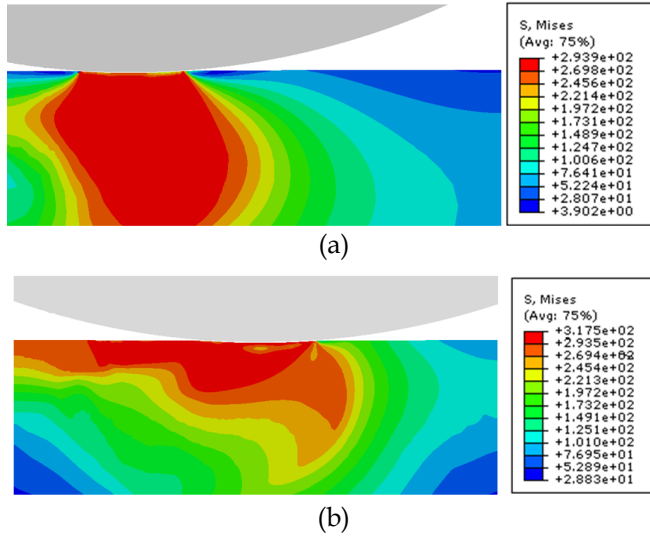


**Figure 3.11:** The contact stress of a rolling contact simulation for  $\omega^* = 9$ : (a) at the end of the static contact; (b) at rolling contact.

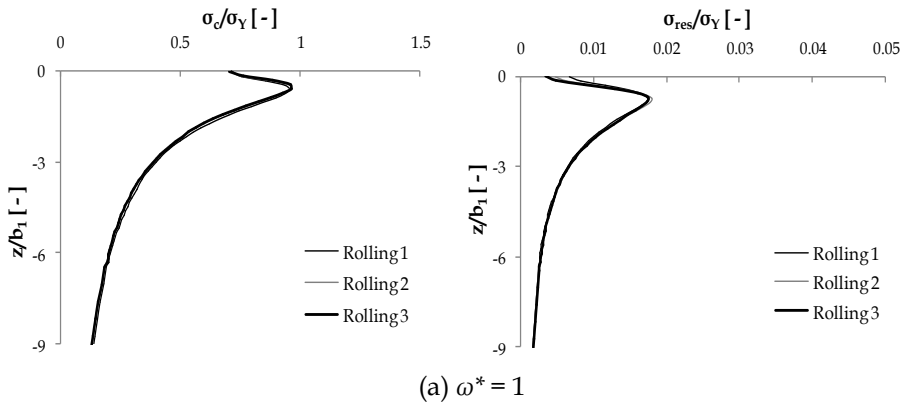


**Figure 3.12:** The normalized contact stress (left side) and residual stress (right side) of the rolling contact simulation versus the normalized distance in z direction: (a) for  $\omega^* = 1$ , (b) for  $\omega^* = 3$ , (c) for  $\omega^* = 6$  and (d) for  $\omega^* = 9$  (cont. ...).

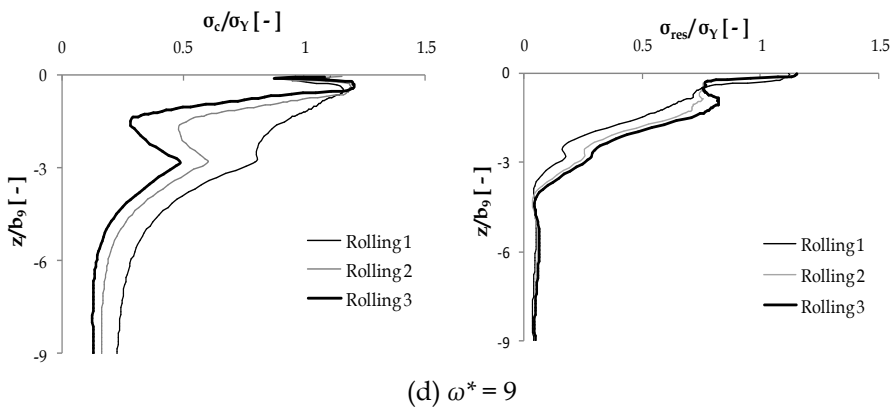
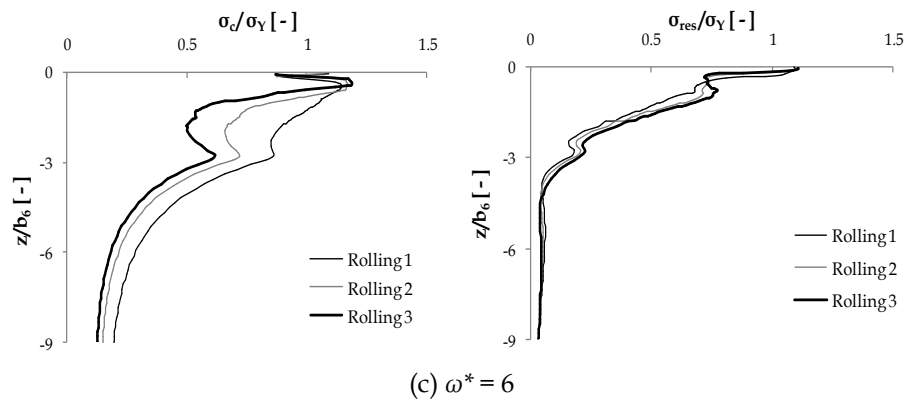
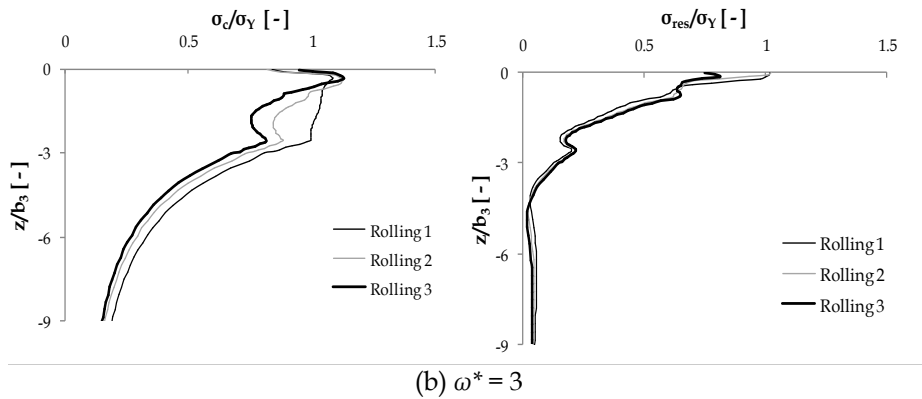


**Figure 3.12:** The normalized contact stress (left side) and residual stress (right side) of the rolling contact simulation versus the normalized distance in z direction: (a) for  $\omega^* = 1$ , (b) for  $\omega^* = 3$ , (c) for  $\omega^* = 6$  and (d) for  $\omega^* = 9$ .

The normalized contact stress ( $\sigma_c$ ) and the residual stress ( $\sigma_{res}$ ) of the rolling contact simulation versus normalized distance in  $z$  direction are depicted for  $\omega^* = 1, 3, 6$  and  $9$  in Figs. 3.12a-3.12d. The normalized contact stress is depicted at the left side whereas the normalized residual stress is depicted on the right side. The stress is normalized with the initial yield stress ( $\sigma_Y$ ) and the  $z$  distance is normalized with the contact width for each interference, as listed in Table 3.3.

Figure 3.13 depicts the plastic deformation of the flat surface, calculated in the middle of the rolling track after the load was released, for  $\omega^* = 1, 3, 6$  and  $9$ . For  $\omega^* = 1$ , very low plastic deformation was found and it increases with the increase of the interference. For  $\omega^* = 3, 6$  and  $9$ , the plastic deformation increases significantly from the first rolling to the second rolling but after the second rolling the increase in plastic deformation reduces. The deformation starts to achieve its steady-state form, i.e. with the next passing of the rolling cylinder deformation hardly changes.

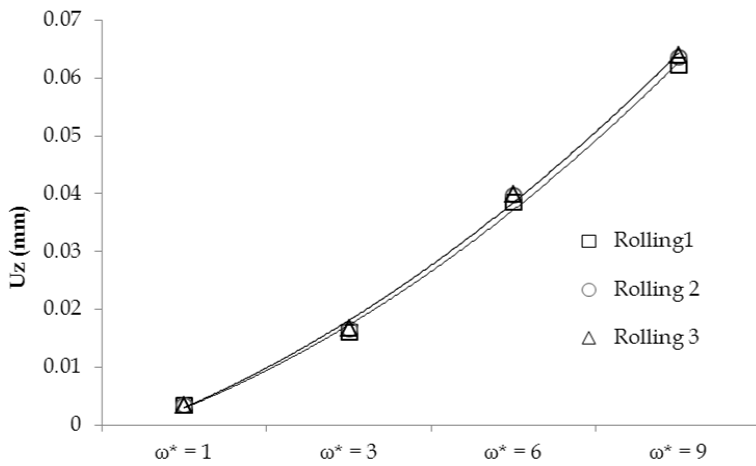


**Figure 3.13:** Plastic deformation of a flat surface in  $z$  direction in the middle of the rolling track for all interferences for a repeated rolling contact.

### 3.4 Running-in of a rigid cylinder rolling on a rough flat surface

#### 3.4.1 Contact model and simulation procedure

A rigid cylinder with the same dimensions as in the previous section was rolled over an artificial rough surface whilst again assuming plain strain. The cylinder was 4.76 mm in diameter ( $R_c$ ) while the asperity height of the rough surface,  $Z_{as}$ , was 0.2 mm, the radius of the asperity,  $R_{as}$ , was 0.24 mm and the pitch of the rough surface,  $P$  was 0.5 mm. Figure 3.14 depicts the details of the contact and the dimensions.

As in the previous section, the rough surface material was aluminium, with the elastic modulus ( $E$ ), yield stress ( $\sigma_Y$ ) and Poisson's ratio ( $\nu$ ) 70 GPa, 270 MPa and 0.32 respectively. The rough surface is also considered to behave elastic-plastic with strain hardening behaviour, see Bhowmik [9]. The cylinder is modelled as a rigid body.

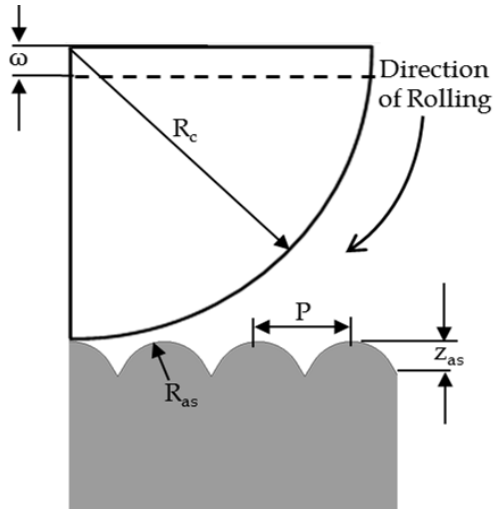


**Figure 3.14:** Details of the 2D rough surface contact and parameters.

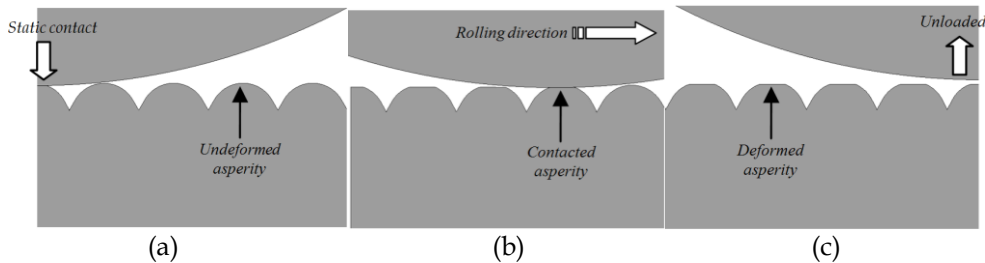


**Figure 3.15:** The rolling contact simulation for  $\omega_2 = 1.1 \times 10^{-4}$  mm: (a) start, the static contact; (b) continued by rolling; and (c) unloading.

Four-nodes-element with the plain strain assumption is applied to model the rough surface and a refined mesh was applied at the top of the rough surface. The mesh generated is of mesh type 2 as explained in Section 3.2, where an automatic mesh was arranged by ABAQUS. For one of the asperities also a subsurface mesh refinement was made, in order to be able to analyse the contact stresses and residual stresses in more detail.

The simulation steps, as shown in Fig. 3.15, were conducted as follows: (a) static contact between cylinder and rough surface for an interference,  $\omega$ ; (b) by maintaining the vertical interference, the cylinder rolled incrementally until it reached the end of the track and the cylinder was pulled up for unloading; (c) the

rolling contact of the cylinder over the rough surface was repeated three times in order to observe the changes in topography and stress distributions during the running-in phase. A free and frictionless rolling contact was assumed.

### 3.4.2 Single rolling contact

This section discusses the results of the single rolling contact for  $\omega^* = 1, 3, 6$  and  $9$  with respect to the topographical change of one of the asperities. The contact stress and the residual stress are analysed.

The surface topographical change of an asperity after a single overrolling is presented in Fig. 3.16. The normalized asperity deformation in  $z$  direction ( $z/R_{as}$ ) is plotted versus the normalized lateral direction ( $x/R_{as}$ ). For  $\omega^* = 1$ , the asperity did not change because the applied interference is still at the transition between elastic to elastic-plastic deformation. As the interference increases, a truncation of the asperity becomes more apparent and material displaces in lateral direction. For  $\omega^* = 9$  a flat area at the summit of the asperity is clearly visible.

The normalized contact stress, plotted against the normalized distance in  $z$  direction, is captured in Fig 3.17a. The surface stress is slightly higher than the yield stress for  $\omega^* = 1$  and increases as the interference increases. After reaching the highest stress level (sub-surface), the contact stress decreases significantly with increasing depth. The same behaviour occurs for the other interferences,  $\omega^* = 3, 6$  and  $9$ , whilst a higher stress level was found for a higher interference.

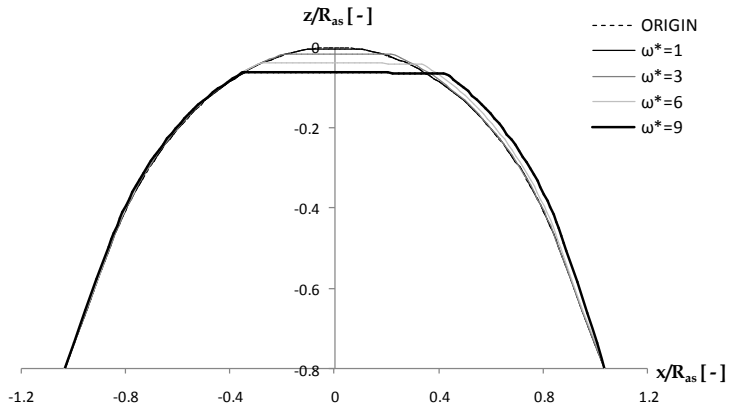


**Figure 3.16:** Topographical change of a single asperity due to rolling contact.

The normalized resultant of the residual stress, based on von Mises, is plotted as a function of the normalized distance in  $z$  direction in Fig. 3.17b. For all applied interferences, the highest residual stress is located at the surface of the asperity and the values calculated are lower than the yield stress of the material. The increase of the residual stress around  $z/R_{as} = 1/2$  is found as the response of the

highest contact stress in the asperity when the asperity is in contact with the cylinder. The small increase of the residual stress around  $z/R_{as} = 1$  is caused by the effect of the transition of the asperity to the bulk material. A stress concentration is found at the root of the asperity due to the geometry of the sharp edge at the valleys in between the asperities.

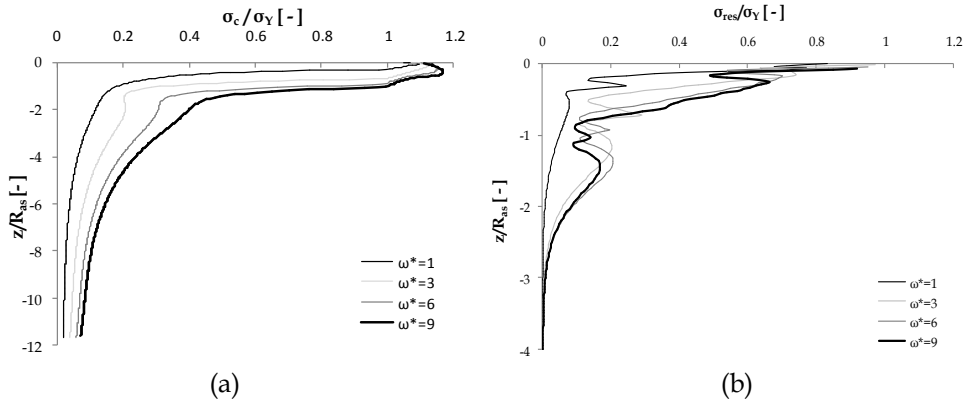


**Figure 3.17:** Results of a single rolling contact between cylinder and rough surface: (a) the normalized von Mises contact stress as a function of the normalized depth and (b) the normalized residual stress as a function of the normalized depth.

### 3.4.3 Running-in of rolling contact

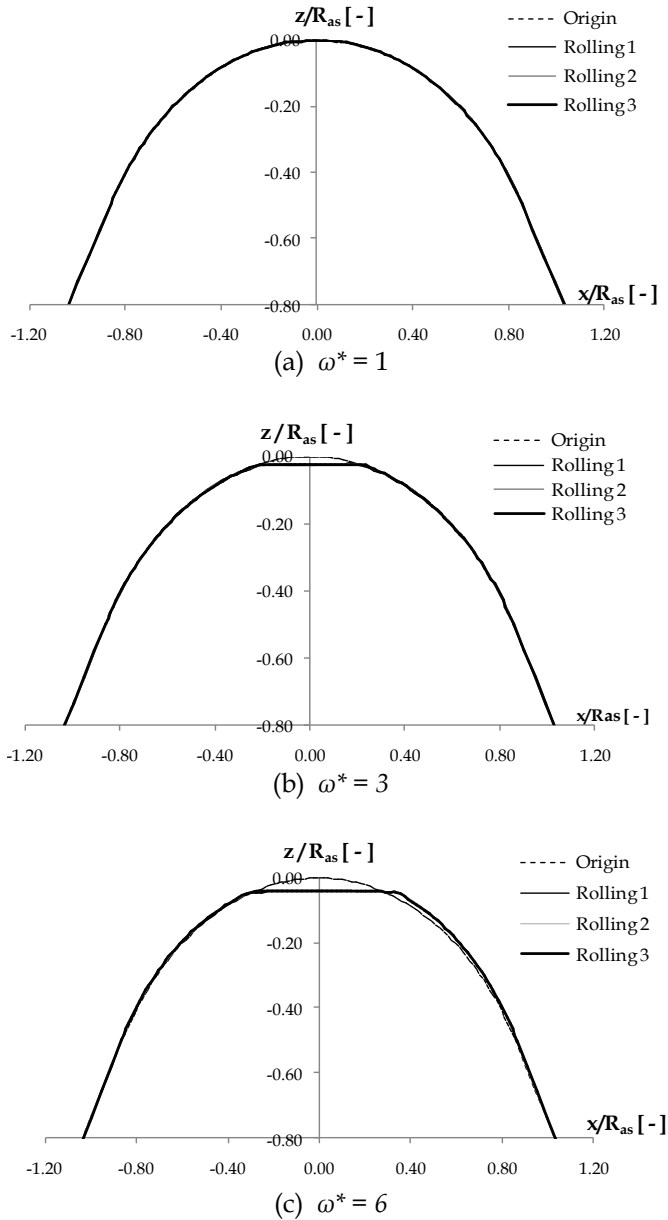
The previous simulation on a single rolling pass was continued by repeating the rolling contact several times. It is found that the modelling of the topographical change, contact stress, residual stress and plastic strain of the repeated rolling contact was reached after the third overrolling.

#### 3.4.3.1 Topographical change

The effects of repeated rolling for different interferences on the asperity topographical change are shown in Fig. 3.18a-3.18d. The dashed and solid lines show the situation before and after the rolling contact deformation, respectively. The deformation was captured after unloading of each rolling cycle.

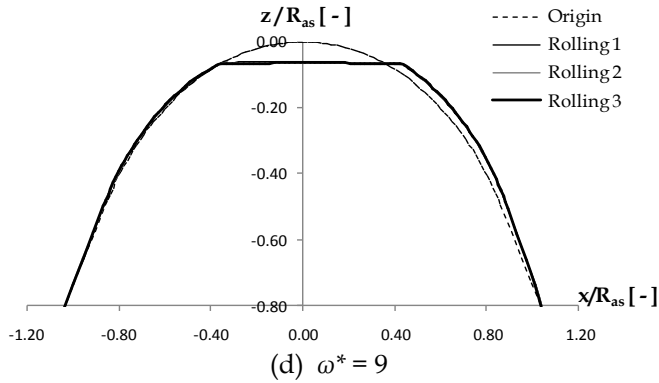
The surface topography change of the asperity summits for  $\omega^* = 1$  do not alter by the repeated rolling contact due to its elastic deformation, as shown in Fig. 3.18a. The change of the asperity due to rolling contact can be observed clearly in Figs. 3.18b-3.18d for  $\omega^* = 3, 6$  and  $9$ . The figures show that the first cycle causes the highest deformation and it is followed by only a slight increase in deformation at the second cycle. There is almost no difference in the asperity shape after the

second cycle, which implies that in this case the steady-state shape is reached. The transition of the running-in to the steady-state phase of a rolling contact occurs in this case within two cycles.



**Figure 3.18:** Topographical change of a single asperity for: (a)  $\omega^* = 1$ , (b)  $\omega^* = 3$ , (c)  $\omega^* = 6$  and (d)  $\omega^* = 9$  (cont. ...)

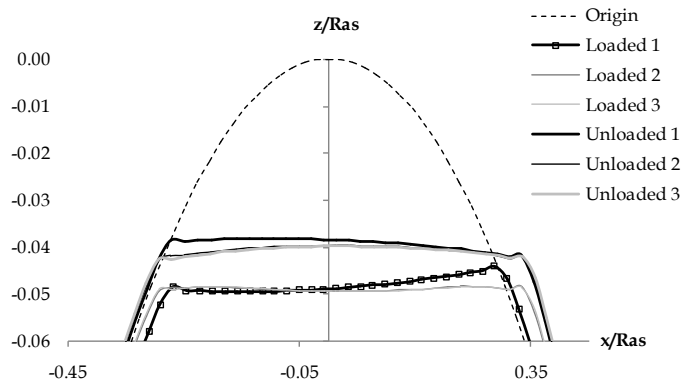




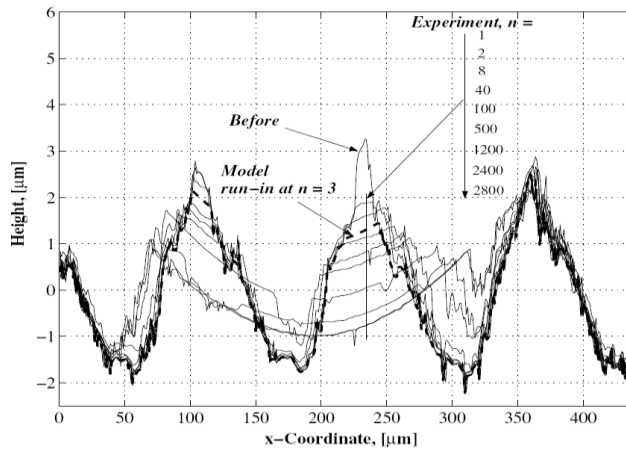
**Figure 3.18:** Topographical change of a single asperity for: (a)  $\omega^* = 1$ , (b)  $\omega^* = 3$ , (c)  $\omega^* = 6$  and (d)  $\omega^* = 9$ .

Figure 3.19 shows the details of the surface topographical change on the asperity summits where  $\omega^* = 6$  is selected as an example. It depicts the elastic recovery and indicates that the deformation takes place in the elastic-plastic regime. During the first rolling contact (denoted as Loaded 1), the normalized deformation of the asperity reaches a maximum value around -0.05. Elastic spring back takes place when the asperity was unloaded (denoted as Unloaded 1) and the maximum deformation of the asperity reduced to -0.04. The same behaviour of the elastic spring back occurs for Loaded 2 to Unloaded 2 and Loaded 3 to Unloaded 3 contact situation. The final topographical change of the asperity after repeated rolling is clearly visible in Fig. 3.19.

In their FEA of a rolling cylinder over a deformable flat, Bijak-Zachowski and Marek [8] also found that the steady-state deformation was usually attained within the first two cycles of repeated rolling contact. The deformation for the next overrollings is small. Jamari [3] reported that the flattening of the asperities of a rough surface is initially high in the first ten rolling cycles while Taşan et al. [19] found that the first rolling contact has the highest deformation, followed by only a slight deformation in the next cycles.



**Figure 3.19:** Topographical change of a single asperity for  $\omega^* = 6$  during rolling contact (loaded) and unloaded situation.



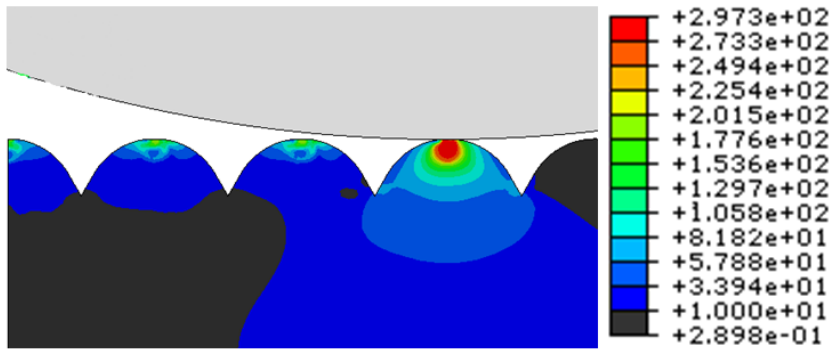
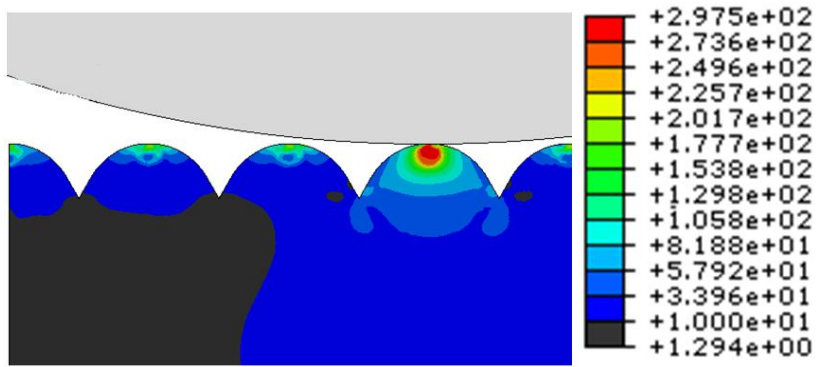
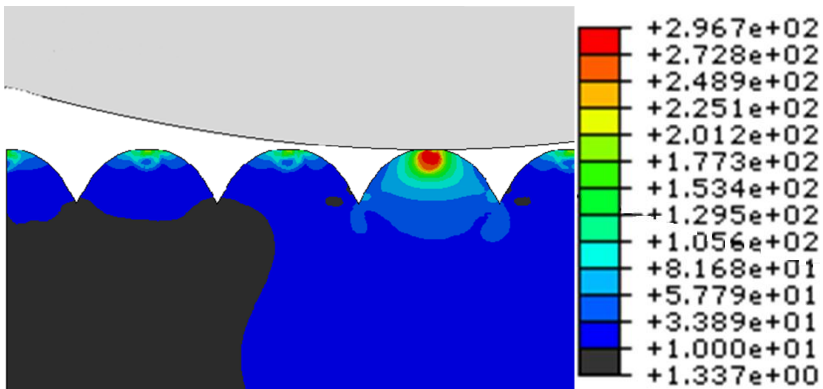
**Figure 3.20:** Topographical change of a rough surface of aluminium during running-in of a rolling contact, in which  $n$  is the number of overrollings. Note the material flow [3].

The flattening of the asperities in the first rolling cycle means that the conformity of the contact increases due to plastic deformation. With the increase in conformity of the contact, the contact area starts to increase and the contact stress becomes more homogeneously distributed. The increasing conformity and contact area induce stability of the shape of the asperities. The material of the summit of the asperity is displaced laterally in the direction of rolling. The material flow of the asperity increases as the applied interference is increased. The space between asperities allows the material of the asperity to be displaced freely. The displacement of the material was also captured in the experiments of Jamari [3] as depicted in Fig. 3.20. The transfer of the material reduces the (residual) stress at the summit of the asperity, as will be discussed in the next section.

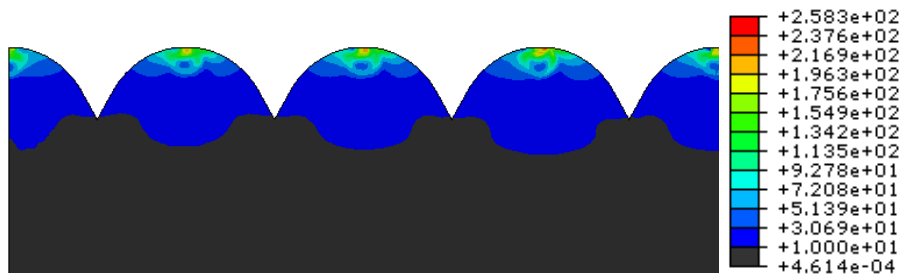
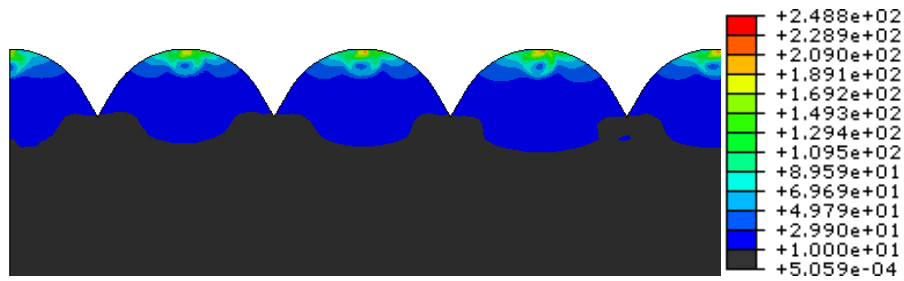
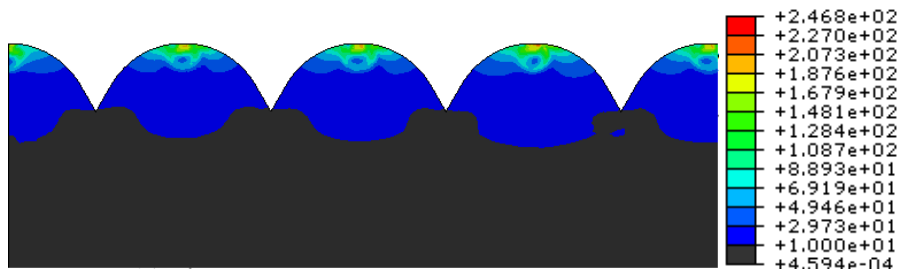
### 3.4.3.2 Stresses

The contact stress and the residual stress of a repeated rolling contact for  $\omega^* = 1$  and 9 are depicted in Figs. 3.21-3.24, respectively. Figures 3.21 and 3.23 depict the situation when the rigid cylinder is located at the centre of the contacted asperity, which is marked with the highlighted equivalent von Mises contact stress distribution, while Figures 3.22 and 3.24 show the equivalent residual stress after the first and consecutive overrollings. Plastic deformation can be noticed on the summit of the asperity. The maximum von Mises stress reaches the surface, as was seen by Jackson and Green [10] who modelled an elastic-plastic static contact between a hemisphere and a rigid flat.

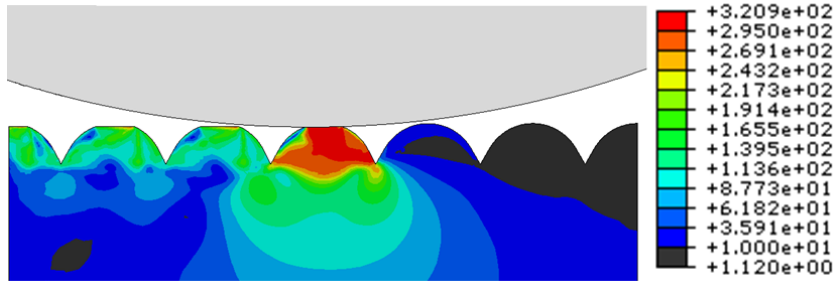
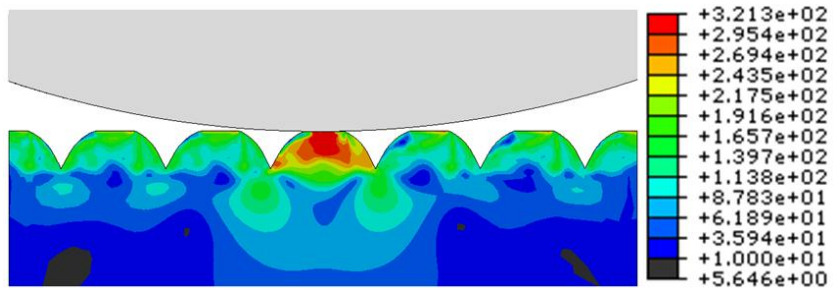
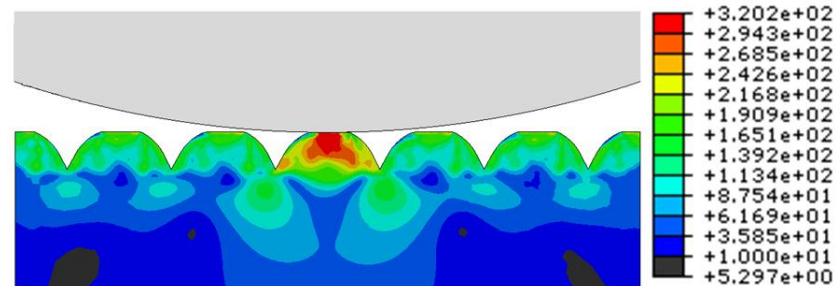
The impact of the repeated rolling contact on the distributions of the equivalent contact stress and residual stress is depicted in Figs. 3.23-3.24 for  $\omega^* = 9$ . During the first rolling contact, it can be seen in Fig. 3.23 that the highest contact stress takes place on the right-hand side of the asperity, due to plastic flow of the material. The free space on the right side of the asperity allows material flow, causing the stress to release and thus reducing the residual stress.

(a) 1<sup>st</sup> Rolling(b) 2<sup>nd</sup> Rolling(c) 3<sup>rd</sup> Rolling

**Figure 3.21:** The von Mises contact stress (MPa) for  $\omega^* = 1$ : (a) first; (b) second; and (c) third rolling.

(a) 1<sup>st</sup> Rolling(b) 2<sup>nd</sup> Rolling(c) 3<sup>rd</sup> Rolling

**Figure 3.22:** The von Mises residual stress (MPa) for  $\omega^* = 1$ : (a) first; (b) second; and (c) third rolling.

(a) 1<sup>st</sup> Rolling(b) 2<sup>nd</sup> Rolling(b) 3<sup>rd</sup> Rolling

**Figure 3.23:** The von Mises contact stress (MPa) for  $\omega^* = 9$ : (a) first; (b) second; and (c) third rolling.

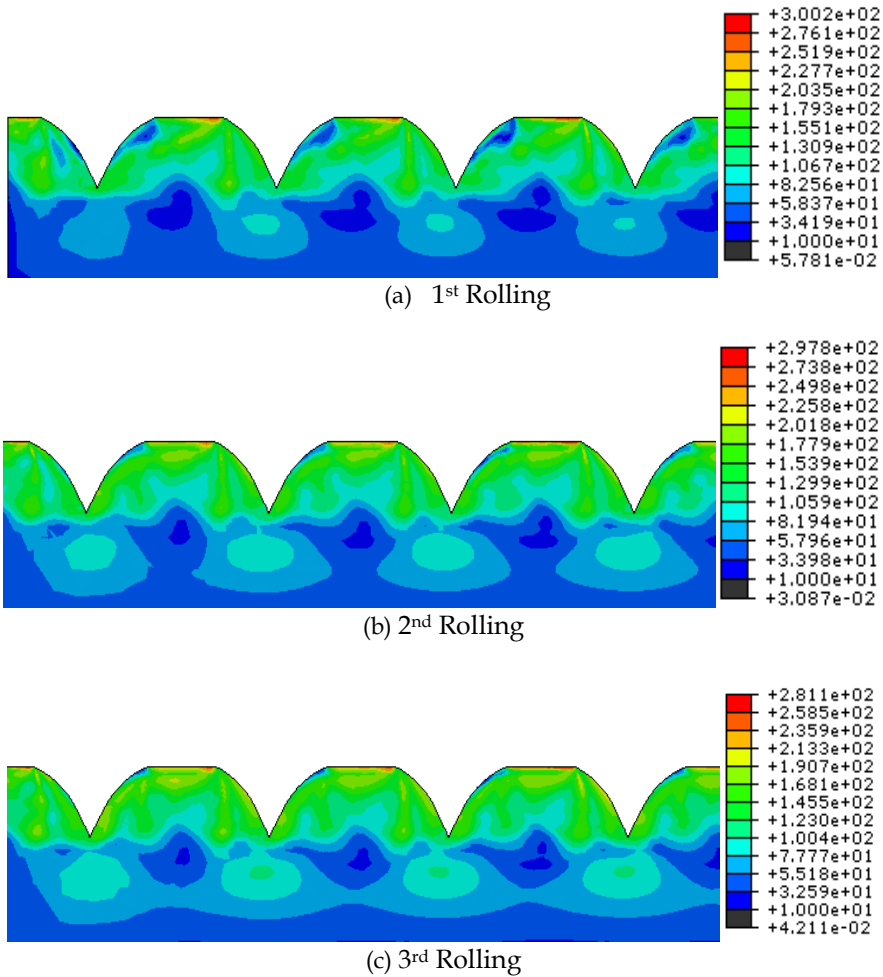


**Figure 3.24:** The von Mises residual stress (MPa) for  $\omega^* = 9$ : (a) first; (b) second; and (c) third rolling.

The normalized von Mises contact stress ( $\sigma_c$ ) and the residual stress ( $\sigma_{res}$ ) are plotted as a function of the normalized depth of the rough surface for three repeated rollings as seen in Figure 3.25a-3.25d. The stress is normalized with the yield stress ( $\sigma_Y$ ) and the  $z$  distance is normalized with the asperity radius,  $R_{as}$ . In Fig. 3.25a for  $\omega^* = 1$ , the behaviour of the contact and residual stress distributions does not show a difference between the first and third rolling contact.

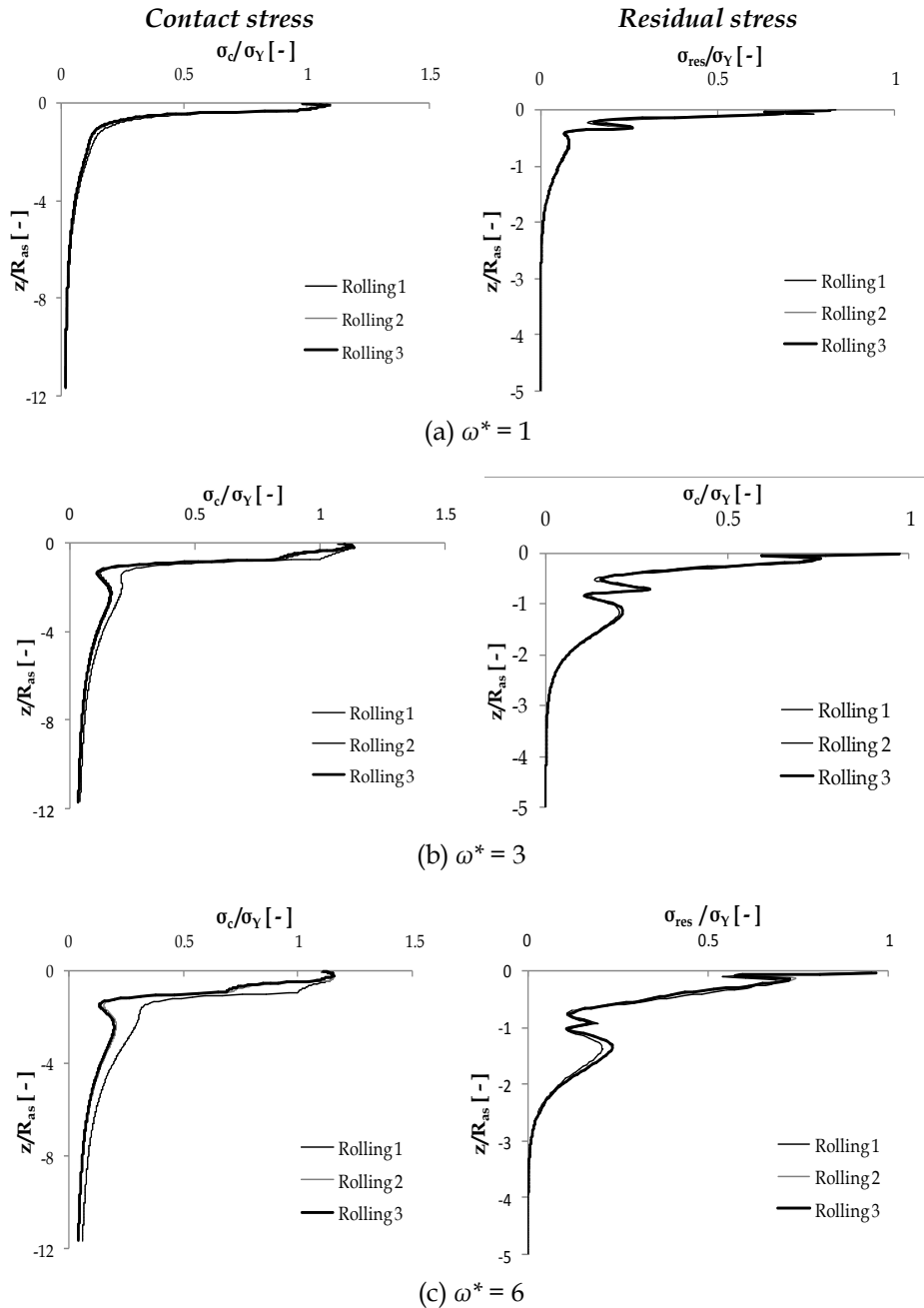


**Figure 3.25:** Results of repeated overrollings of a rough surface: the normalized von Mises contact stress (left side) as a function of normalized depth in the  $z$  direction and the normalized residual stress (right side) as a function of normalized depth in the  $z$  direction (cont. ...).



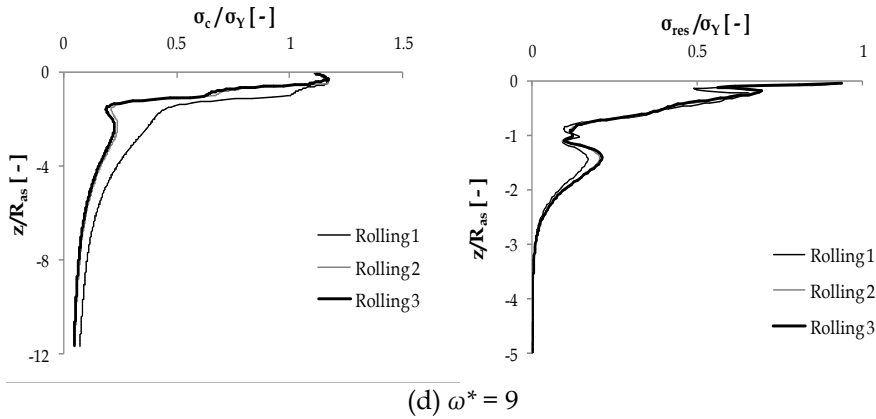


**Figure 3.25:** Results of repeated overrollings of a rough surface: the normalized von Mises contact stress (left side) as a function of normalized depth in the  $z$  direction and the normalized residual stress (right side) as a function of normalized depth in the  $z$  direction.

In Fig. 3.25b-3.25d for  $\omega^* = 3, 6$  and  $9$ , the difference between the first and the second rolling contact becomes more apparent for both the contact stress and the residual stress. However, the distribution curve of the second and the third rolling contact coincides, which implies that the steady-state contact stress and residual stress distribution takes place in the first two cycles. Bijak-Zachowski and Marek [8], who studied the rolling contact of a flat including friction, also indicated that the stabilized residual stress distribution occurred after the first two cycles. Kadin, et al. [13] studied the multiple loading-unloading of a spherical contact and reported a stability of the stress distribution after the second loading-unloading contact. They pointed out that strain hardening mechanism induces this behaviour. However, in the case of contact on asperity level, the cause of stabilization of the contact and residual stress in the first two cycles is not only affected by strain hardening behaviour but also by the flattening of the asperity, i.e. a larger contact area. The contact load is homogeneously distributed over the truncated asperity and results in a decrease of the contact stress and residual stress.

Figure 3.25 shows that the residual stress distributions on asperity level of the artificial rough surface for all interferences do not exceed the initial yield stress. This is different than was observed for a rolling contact on flat surface as shown in Fig. 3.12. It can be concluded that a repeated rolling contact on a rough surface results in a lower equivalent residual stress than when overrolling a smooth surface, at the same interference.

## 3.4.3.3 Plastic Strain

The evolution of the equivalent plastic strain after unloading of the repeated rolling contact on a rough surface is depicted in Fig. 3.26 and 3.27 for  $\omega^* = 1$  and  $\omega^* = 9$ , respectively. A small area of plastic strain is found for  $\omega^* = 1$  where the value of the strain does not result in a topographical change. On the other hand, large plastic strains are found for  $\omega^* = 9$ , where the direction of the plastic strain is in the rolling contact direction. The plastic strain reaches the surface and is able to induce detachment of material or initiate cracks [20]. The topographical change of the rough surface due to repeated rolling causes flattening of the asperities and hence results in a smoother surface.

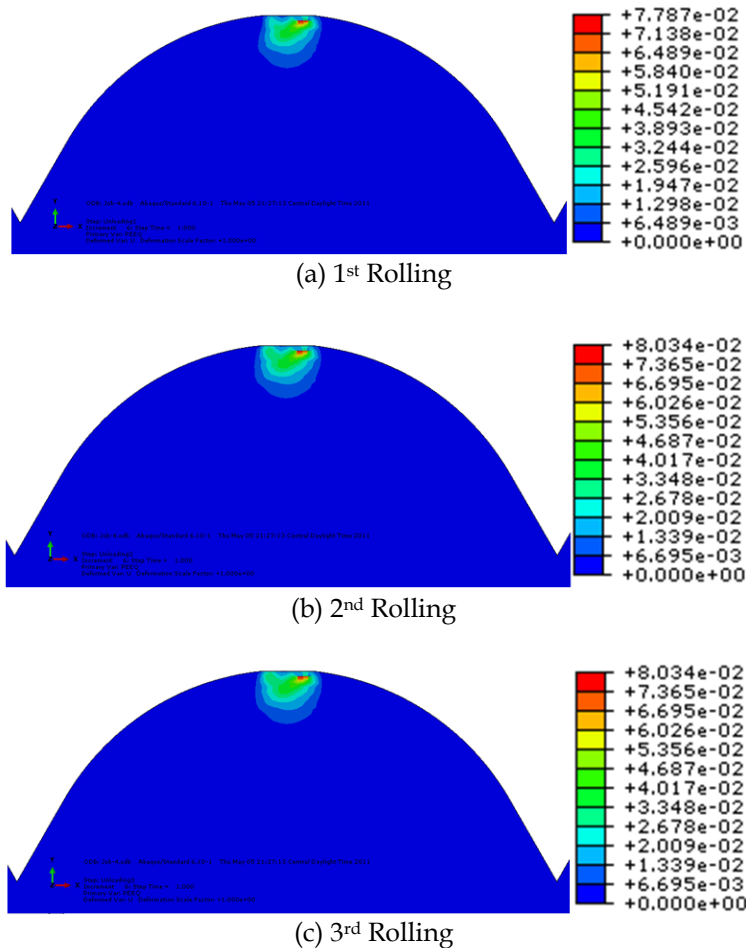


**Figure 3.26:** The equivalent plastic strain of repeated rolling contact after unloading for  $\omega^* = 1$ : (a) first; (b) second; and (c) third overrolling.

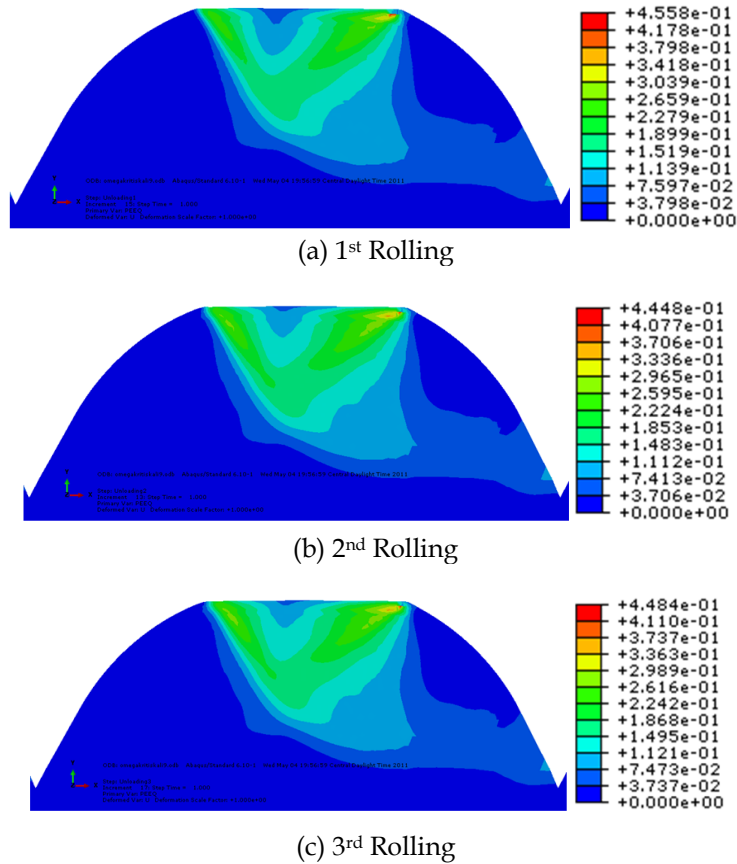


**Figure 3.27:** The equivalent plastic strain of repeated rolling contact after unloading for  $\omega^* = 9$ : (a) first; (b) second; and (c) third overrolling.

### 3.5 Running-in of a rigid ball rolling on a rough surface

The simulation of the running-in of a rigid ball on a rough flat surface is studied. Taşan [18] and Jamari [3] experimentally and analytically investigated the rolling contact situation using a hard ball rolling over a deformable rough surface on a pin-on-disc tribometer. Taşan [18] reported a change of the micro geometry of the disc on asperity level in both lateral and longitudinal direction. The change in surface topography, which is caused by plastic deformation, mainly took place in the first two cycles, after which the amount of deformation decreased and the surface topography started to reach its final form [19].

Jamari's experiments [3] confirmed that the initial cycles of the rolling contact act as the key factor in changing the surface topography on asperity level.

Jamari focused his work on asperity level and compared the surface topographical change with an analytical model. Jamari and Schipper [4, 5] developed an ellipsoid static contact model to predict elastic, elastic-plastic and fully plastic deformation. The model successfully predicted the change of the surface topography and had a good agreement with the experimentally obtained results on running-in, in particular for the first ten cycles. Based on the experimental and analytical work of the aforementioned investigations, the finite element approach is proposed for determining the change in the surface topography in order to study the rolling-sliding contact situation at a later date.

This section describes an elastic-plastic finite element analysis of rolling contacts between a rigid ball and a rough surface. The method in generating the rough surface is described further in Appendix B.

### 3.5.1 Contact model and simulation procedures

The schematic illustration of the rolling contact studied is depicted in Fig. 3.28. A rigid ball, with  $R = 5$  mm, is rolled over a rough aluminium surface with elastic-perfectly plastic material behaviour. The mechanical properties of the aluminium in the simulations follow the experimental research on repeated static contact of Jamari [3] where the elastic modulus ( $E$ ), yield stress ( $\sigma_Y$ ), and Poisson's ratio ( $\nu$ ) are 75.2 GPa, 85.72 MPa and 0.34 respectively. Detail of the mesh for the finite element model is depicted in Fig. 3.29. The refined mesh is located along the rolling path of contact for increasing the accuracy of the parameters studied.

The simulation procedure of the rolling contact is the same as explained in Section 3.4.1. In the previous section, however, the rolling contact was modelled as a cylinder and a two-dimensional rough surface and the interference was used to model the contact load. In this simulation, the rolling contact is modelled as a ball and a three-dimensional rough surface and a range of normal forces are used to simulate the severity of the contact. The ball is pressed normally on the rough surface with 0.05 N, 0.5 N and 5 N followed by rolling along the rolling path while maintaining the contact load. The ball is unloaded after reaching the end of the track.

The rolling contact simulation is repeated three times in order to investigate the running-in phase. The topographical change of the rough surface, the residual stress as well as the equivalent plastic strain are calculated to show the final strain after the contact is unloaded.

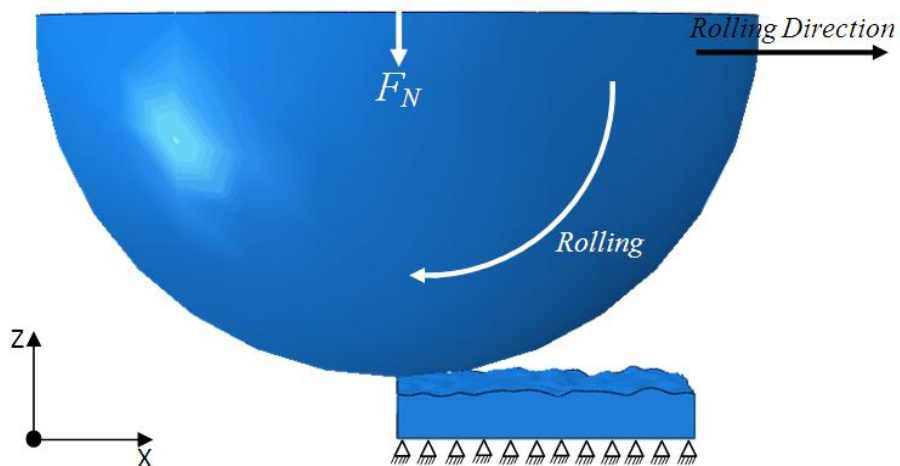


**Figure 3.28:** The schematic illustration of the rolling contact simulation of a rigid hemisphere on a rough surface.

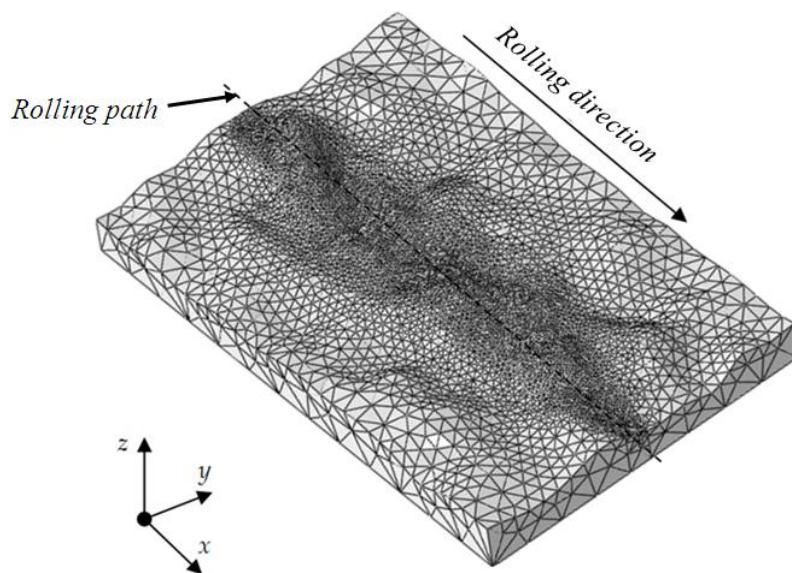


**Figure 3.29:** The mesh on the rough surface model.

### 3.5.2 Topographical change

The topographical change of the rough surface due to plastic deformation is discussed in this section. Figures 3.30, 3.31 and 3.32 depict the height of the rough surface along the rolling path for  $F_N = 0.05$  N, 0.5 N and 5 N, respectively. The surface topographical change in these figures is given after each overrolling. The number of overrollings is indicated as  $n$ . The original surface topography is marked with a dash line and the deformed surface topography due to rolling are marked with a solid line.

In Fig. 3.30 where a contact load of 0.05 N was applied no significant deformation is observed along the rolling path. The final surface topography does not alter after the three overrollings. It indicates that the surface deforms elastically. In Fig. 3.31 where a contact load of 0.5 N was applied, some plastic deformation occurred on the last asperity while on the two previous asperities, no significant plastic deformation took place.

Figure 3.32 shows that plastic deformation is observed for the three high asperities. It can be seen that most of the plastic deformation takes place during the first overrolling followed by some additional plastic deformation due to the second and third overrolling. This was also found in the two-dimensional simulation in Section 3.4.3.1. The results found imply that the steady-state plastic deformation is reached and the transition of the running-in phase to the steady-state phase of the rolling contact occurs within two to three cycles.

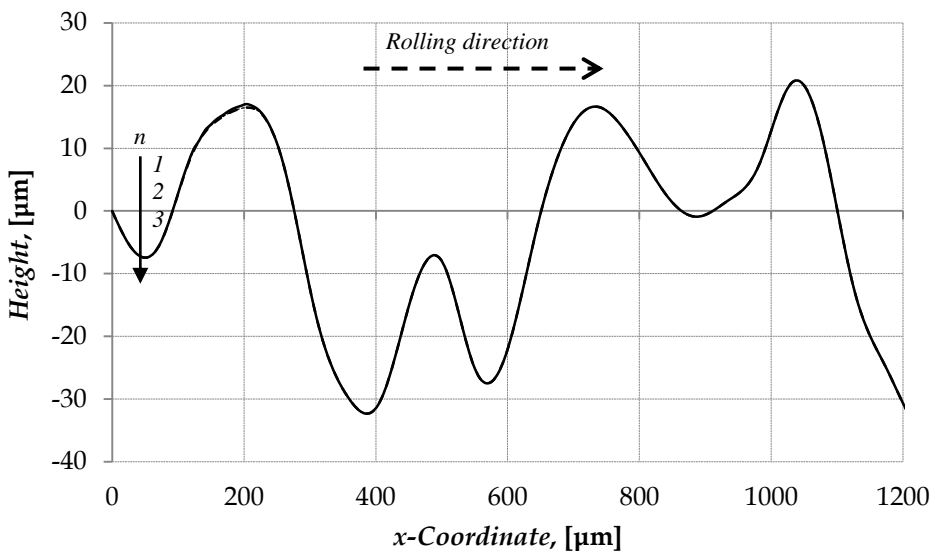


**Figure 3.30:** Surface topographical change of the rough surface for  $F_N = 0.05$  N.

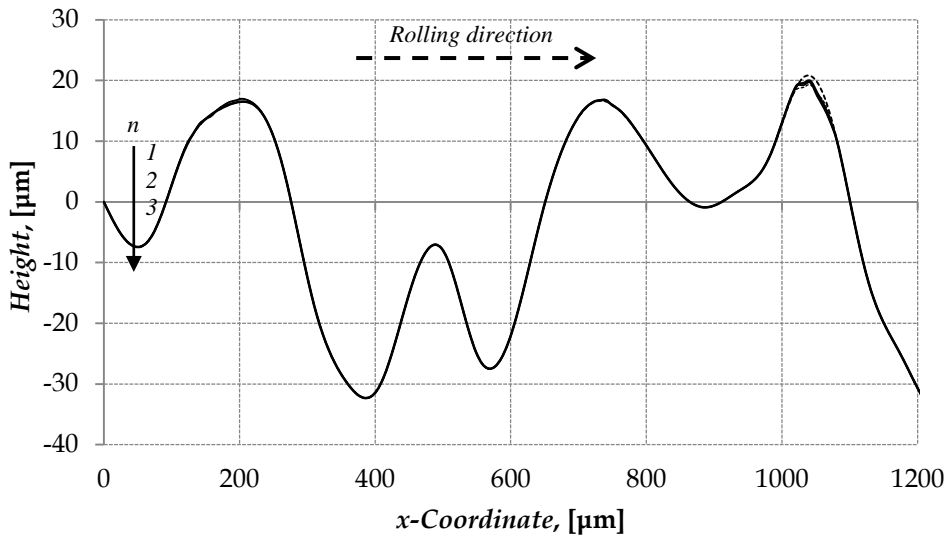


**Figure 3.31:** Surface topographical change of the rough surface for  $F_N = 0.5$  N.

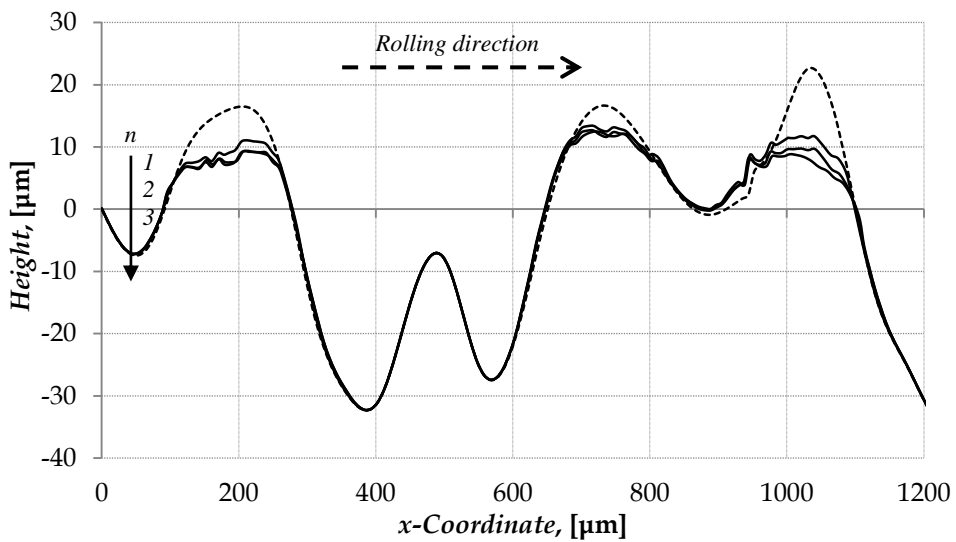


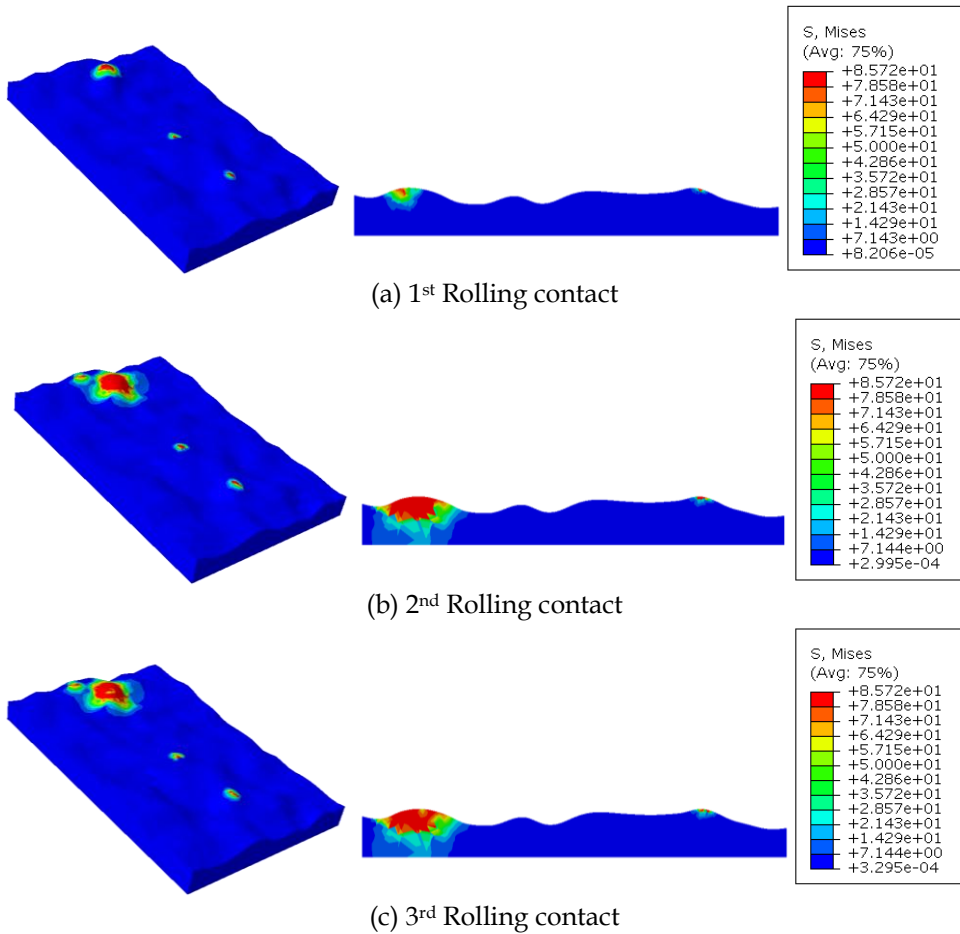
**Figure 3.32:** Surface topographical change of the rough surface for  $F_N = 5$  N.

### 3.5.3 Stresses

The calculated von Mises residual stress distribution is presented in this section to analyse the residual stress after the contact is unloaded. In order to have a detailed observation of the stress distribution, the rough surface is cut along the rolling path

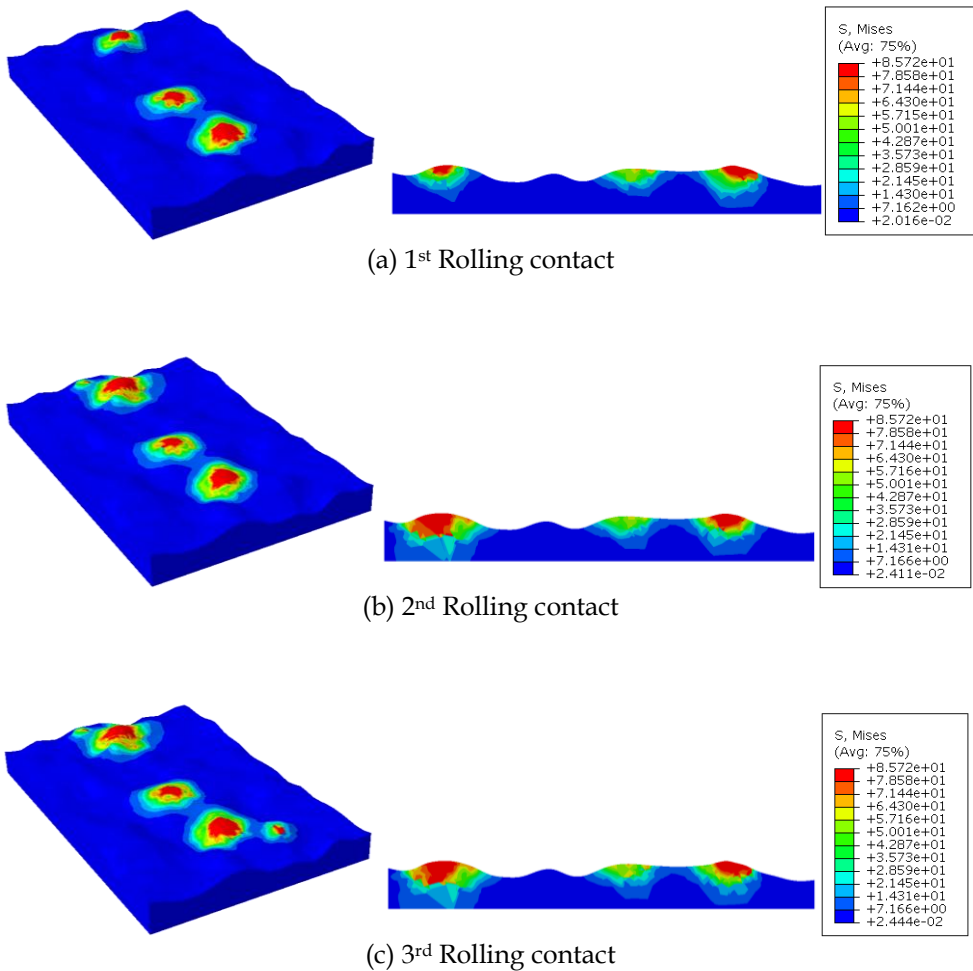
in the X-Z plane, at the same location of the observed surface topographical change. The von Mises residual stresses of the rough surface, for  $F_N = 0.05\text{ N}$ ,  $0.5\text{ N}$  and  $5\text{ N}$ , are depicted in Figs. 3.33, 3.34 and 3.35, respectively.

The von Mises residual stress for a contact load of  $0.05\text{ N}$  for the first, second and third cycle of rolling contact, as depicted in Fig. 3.33 (a-c), show that the residual stress field is getting larger as the number of overrollings increases. However, the rolling contact is rather located and contributes only to a small residual stress field.



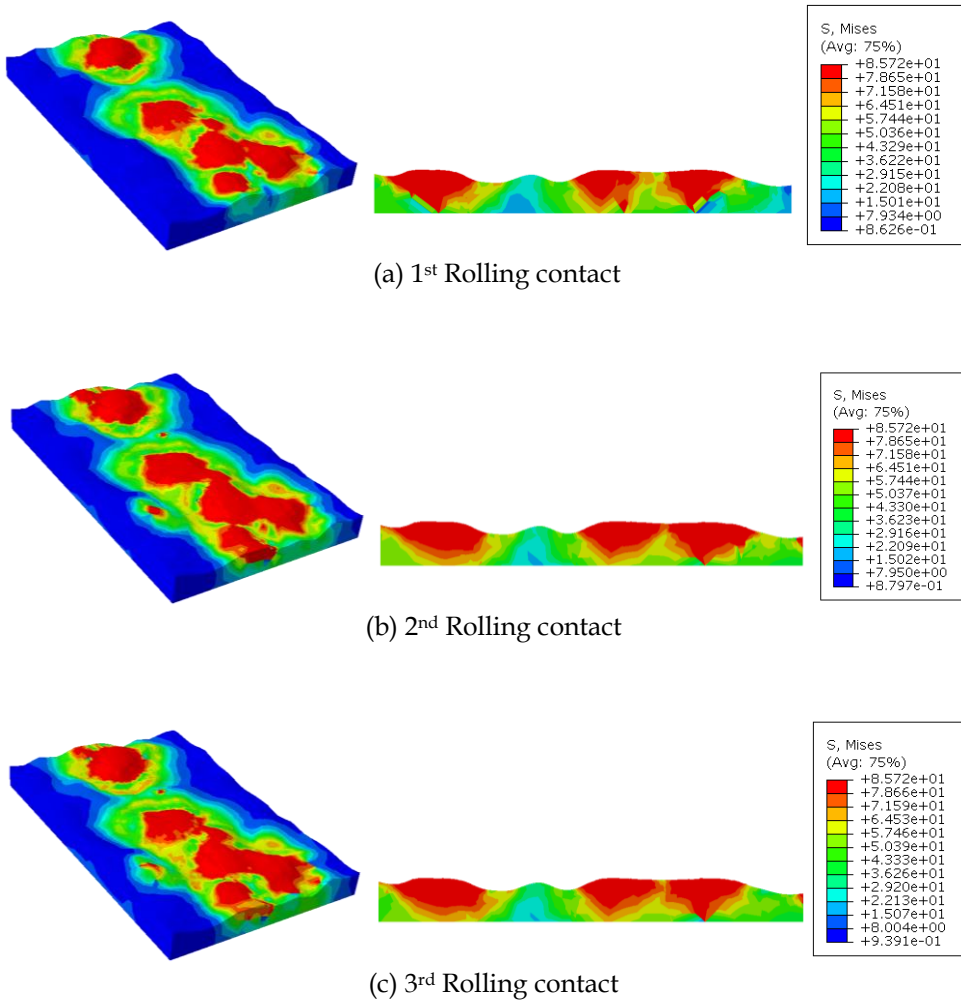
**Figure 3.33:** The von Mises residual stress (MPa) of repeated rolling contact after unloading for  $F_N = 0.05\text{ N}$ : (a) first; (b) second; and (c) third overrolling.





**Figure 3.34:** The von Mises residual stress (MPa) of repeated rolling contact after unloading for  $F_N = 0.5$  N: (a) first; (b) second; and (c) third overrolling.

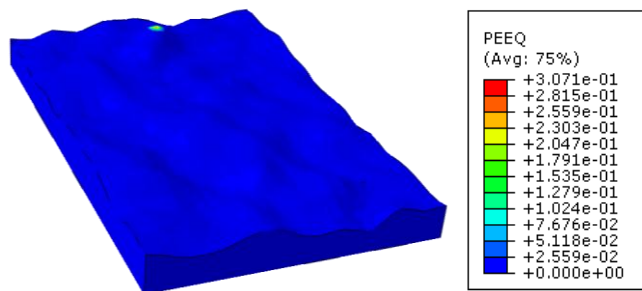
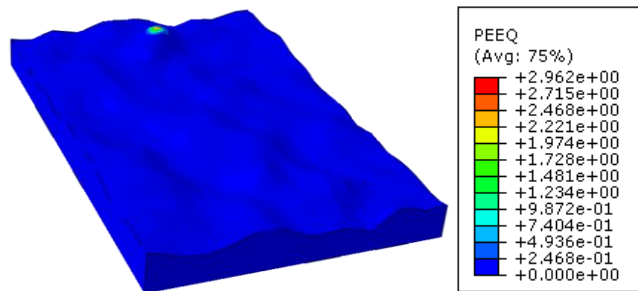
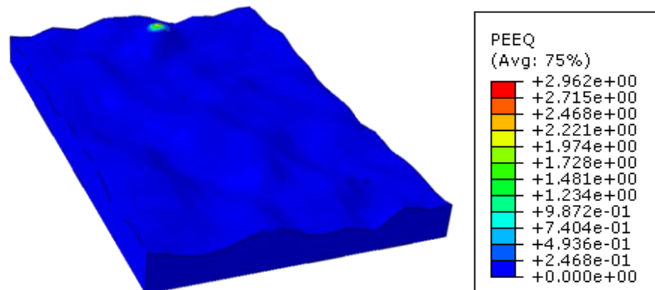
The increase of the contact load affects the area of the von Mises residual stress on the surface and subsurface and also the number of the interacting asperities as depicted in Fig. 3.34 and 3.35 for a contact load of 0.5 N and 5 N, respectively. As expected the residual stress field increases as the normal load applied to the ball-rough surface contact increases.



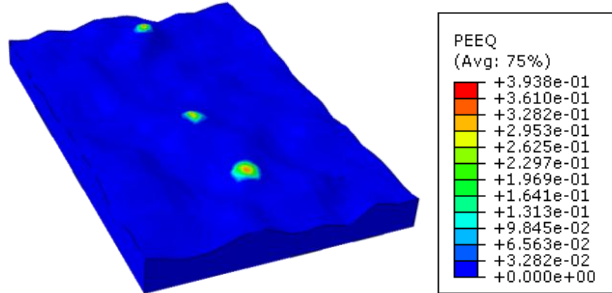
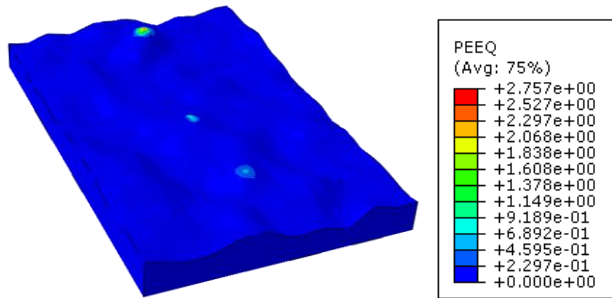
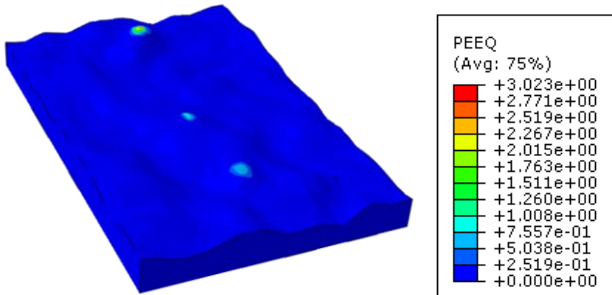
**Figure 3.35:** The von Mises residual stress (MPa) of repeated rolling contact after unloading for  $F_N = 5$  N: (a) first; (b) second; and (c) third overrolling.

### 3.5.4 Plastic strain

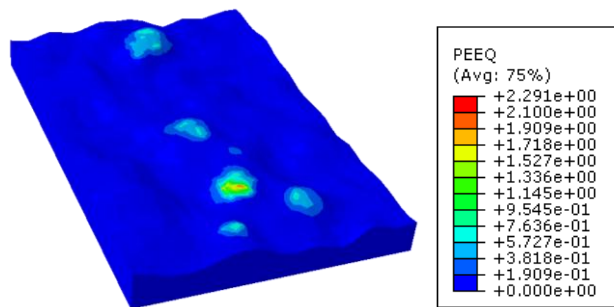
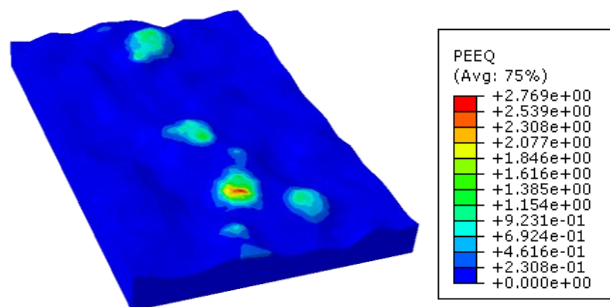
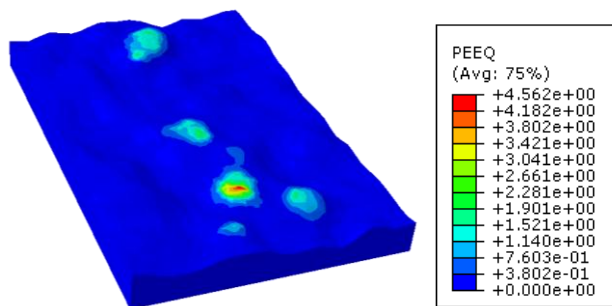
The evolution of the equivalent plastic strain (after unloading of the repeated rolling contact) of the rough surface is depicted in Fig. 3.36, 3.37 and 3.38 for  $F_N = 0.05$  N, 0.5 N and 5 N, respectively. The equivalent plastic strain is captured after the third cycle. A small area of plastic strain is found for the rough surface for  $F_N = 0.05$  N and 0.5 N where the value of the strain is rather low and hardly changes the topography of the surface.

(a) 1<sup>st</sup> Rolling contact(b) 2<sup>nd</sup> Rolling contact(c) 3<sup>rd</sup> Rolling contact

**Figure 3.36:** The equivalent plastic strain of repeated rolling contact after unloading for  $F_N = 0.05$ : (a) first; (b) second; and (c) third overrolling.

(a) 1<sup>st</sup> Rolling contact(b) 2<sup>nd</sup> Rolling contact(c) 3<sup>rd</sup> Rolling contact

**Figure 3.37:** The equivalent plastic strain of repeated rolling contact after unloading for  $F_N = 0.5$ : (a) first; (b) second; and (c) third overrolling.

(a) 1<sup>st</sup> Rolling contact(b) 2<sup>nd</sup> Rolling contact(c) 3<sup>rd</sup> Rolling contact

**Figure 3.38:** The von Mises residual stress of repeated rolling contact after unloading for  $F_N = 5$  N: (a) first; (b) second; and (c) third overrolling.

### 3.5.5 Validation of the FE simulation

Validation of the FE simulation for running-in of a rigid ball rolling on a rough surface is presented by comparing the surface topographical change of Jamari's experiment [3] with the present FE simulation model. Repeated moving

contact of a silicon carbide ceramic ball ( $H = 28$  GPa,  $E = 430$  GPa and  $\nu = 0.17$ ) with a diameter of 6.35 mm on a mild steel rough surface ( $H = 3.55$  GPa,  $E = 210$  GPa and  $\nu = 0.3$ ) was conducted to mimic the pure rolling contact.

The present FE simulation of frictionless rolling contact of a rigid ball on a rough surface, where the schematic illustration is the same as depicted on Fig. 3.28, was carried out. The method in generating the mild steel rough surface, as used by Jamari [3], is described in Appendix B. The mechanical properties of the mild steel model in this simulation follow the experimental research of Jamari [3] and the yield stress ( $\sigma_Y$ ) is assumed as 1.183 GPa.

The comparison of the experiment [3] and the present FE model for the fifth overrolling is depicted in Fig. 3.39. The FE model has good agreement in predicting the surface topographical change due to rolling contact. Jamari [3] reported in his experiment that there is no significant change on the surface topography due to rolling contact after the fifth cycle and exhibits an equilibrium state of the plastic deformation. This implies that the running-in phase is finished and the contacting surface starts to operate in the steady state phase.

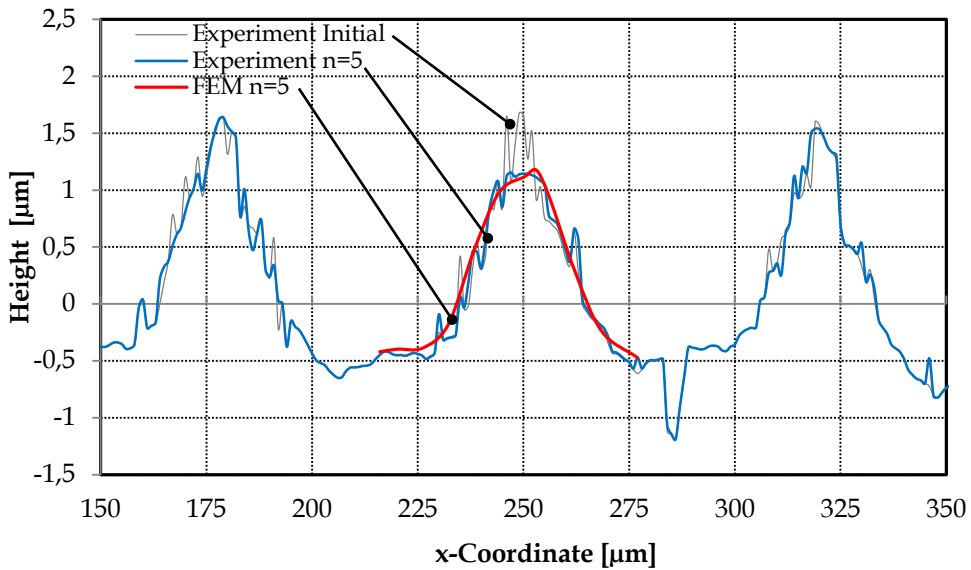


Figure 3.39: Profile of the mild-steel surface after 5 cycles, Jamari [3].

### 3.6 Concluding remarks

With the developed FE models running-in of rolling contacts are studied. The results obtained for a single static contact, repeated static contact and the repeated

rolling contact of a rigid cylinder on a flat smooth surface are in good agreement with results reported in the literature.

Next, the developed model was applied to a repeated rolling contact on a flat rough surface in two cases. First, with the two-dimensional finite element model the running-in of an artificial rough surface overrolled by a rigid cylinder is simulated. The simulations used the critical interference,  $\omega^*$ , as criterion for determining the severity of contact loading. Four values of  $\omega^*$  were used in the rolling contact simulations, which resulted in output related to plastic deformation, contact stress and residual stress. For  $\omega^* = 1$ , a negligible topographical change of the asperities was obtained, as expected, because the contact stress did not exceed the yield stress. For  $\omega^* = 3, 6$  and  $9$ , i.e. an increased contact load, plastic deformation of the asperities occurs, as the contact stress exceeds the yield stress and a high residual stress remains at the surface.

Secondly, with the three-dimensional finite element model, the running-in of a 3-D rough surface by repeated overrolling using a rigid ball is simulated. The simulations employed several contact loads,  $F_N$ , for investigating the severity of the deformation. For  $F_N = 0.05$  N and  $0.5$  N the surface deformed mainly elastically and resulted a negligible topographical change of the asperities. For  $F_N = 5$  N, a significance change in surface topography due to repeated overrolling along the rolling path is observed. The observation made is that the running-in of rolling contacts takes place within the first few cycles.

A comparison of the FE model and experiment of the running-in of a rolling contact is made to validate the FE model. The proposed FE model predicts the running-in of a rolling contact over a rough surface rather well.

The change of the surface topography due to running-in of the rolling contact results in the transformation from a rough surface to a smoother surface: the flattening of the high asperities induces a reduction in surface roughness. This flattening of asperities is due to plastic deformation and plastic flow (material displacement) and causes a higher equivalent residual stress on the surface. The main conclusion is that the transition of the running-in phase to the steady-state phase of a rolling contact is governed by the transition of plastic to elastic deformation on roughness level.

## References


- [1] Hsu, S.M., Munro, R.G., Shen, M.C. and Gate, R.S., 2005, "Boundary lubricated wear," In: *Wear-Materials, Mechanisms & Practice*, G.W. Stachowiak (Ed.), 37-69, John Wiley & Sons Inc., UK.
- [2] Blau, P.J., 1989, *Friction and Wear Transitions of Materials: Break-in, Run-in, Wear-in*, Noyes Publications, Park Ridge, NJ, USA.
- [3] Jamari, J., 2006, *Running-in of Rolling Contacts*, PhD Thesis, University of Twente, Enschede, The Netherlands.

- [4] Jamari, J. and Schipper, D.J., 2006, "An elastic-plastic contact model of ellipsoid bodies," *Tribology Letters*, 21, No. 3, pp. 262-271.
- [5] Jamari, J. and Schipper, D.J., 2008, "Deterministic repeated contact of rough surfaces," *Wear*, 264, pp. 349-358.
- [6] Hertz, H., 1882, "Ueber die Beruehrung fester elastischer Koerper," *J Reine Angew. Math.*, 92, pp. 156-71.
- [7] Green, I., 2005, "Poisson ratio effects and critical values in spherical and cylindrical Hertzian contacts," *International Journal of Applied Mechanics*, 10, No. 3, pp. 451-462.
- [8] Bijak-Zochowski, M. and Marek, P., 1997, "Residual stress in some elasto-plastic problems of rolling contact with friction," *International Journal of Mechanical Science*, 39, No. 1, pp. 15-32.
- [9] Bhowmik, K., 2007, *Experimental and Finite Element Study of Elastic-Plastic Indentation of Rough Surfaces*, Master Thesis, Indian Institute of Science, Bangalore, India.
- [10] Jackson R.L. and Green I., 2005, "A finite element study of elasto-plastic hemispherical contact," *ASME Journal of Tribology*, 127, pp. 343-54.
- [11] Zhao, Y., Maietta, D.M. and Chang, L., 2000, "An asperity microcontact model incorporating the transition from elastic deformation to fully plastic flow," *ASME Journal of Tribology*, 122, pp.86-93.
- [12] Johnson, K.L. and Shercliff, H.R., 1992, "Shakedown of 2-D asperities in sliding contact," *International Journal of Mechanical Science*, 34, pp. 375-394.
- [13] Kadin, Y., Kligerman, Y. and Etsion, I., 2007. "Multiple loading-unloading of an elastic-plastic spherical contact," *International Journal of Solids and Structures*, 43, pp. 7119-7127.
- [14] Bhargava, V., Hahn, G.T. and Rubin, C.A., 1985, "An elastic plastic finite element model of rolling contact, part 1: analysis of single contacts," *ASME Journal of Applied Mechanics*, 52, pp. 67-74.
- [15] Bhargava, V., Hahn, G.T. and Rubin, C.A., 1985, "An elastic plastic finite element model of rolling contact, part 2: analysis of repeated contacts," *ASME Journal of Applied Mechanics*, 52, pp. 74-82.
- [16] Nélias, D., Antaluca, E. and Boucly, V., 2007, "Rolling of an elastic ellipsoid upon an elastic-plastic flat," *ASME Journal of Tribology*, 129, pp. 791-800.
- [17] Kulkarni, S., Hahn, G.T., Rubin, C.A. and Bhargarva, V., 1990, "Elastoplastic finite element analysis of three-dimensional pure rolling contact above the shakedown limit," *ASME Journal of Applied Mechanics*, 58, pp. 347-353.



- [18] Taşan, Y.C., 2005, *Measurement of Deformation in Rolling and Sliding Contacts*, PhD Thesis, University of Twente, Enschede, The Netherlands.
- [19] Taşan, Y.C., de Rooij, M.B. and Schipper, D.J., 2007, "Changes in the micro-geometry of a rolling contact," *Tribology International*, 40, pp. 672-679.
- [20] Nélías, D., Bounicy, V. and Brunet, M., 2006, "Elastic-plastic contact between rough surface: proposal for a wear or running-in model," *ASME Journal of Tribology*, 128, pp. 236-243.





CHAPTER  
4

## Running-in of Sliding Contacts

---

### 4.1 Introduction

Changes to the surface micro-geometry during the running-in phase of a sliding contact are usually related to mild wear processes, as described by Archard's wear concept [1-2], that includes wear particle removal and abrasive wear [3-5]. Some of the models assume that plastic deformation in the running-in of sliding contacts is insignificant [4]. On a macro scale, the sliding contact between two contacting bodies is often referring to an elastic contact situation. The macroscopic wear volume, or the change in the standard deviation of the surface roughness, has been studied extensively [3-6]. However, the local changes of the surface topography during the running-in process did not get much attention. When sliding occurs, it is known that the elastic-plastic contact situation on asperity level plays an important role in the change of the asperity shape. In this chapter, local plastic deformation is taken into account in the sliding contact between surfaces.

Most of the research conducted on running-in of sliding contacts is essentially experimental, and the change in surface topography and the transition from the running-in phase to the steady-state phase is expressed using statistical surface roughness parameters. The coefficient of friction and the wear rate of the contacting materials are the main parameters to distinguish the running-in and steady-state phase [6-11]. This chapter presents a method of analysing the running-in phase. The finite element method was used to analyse the running-in phase and the transition to the steady-state phase.

This chapter contains four sections, where Section 4.2 explores the model for the running-in of a sliding contact between a hemisphere and a flat surface using finite element analysis. An experimental investigation is used to compare the results obtained with the finite element simulations. Section 4.3 discusses the sliding contact of a rough sphere against a smooth flat surface. Finally, concluding

remarks are given in section 4.4, which consist of the findings of several investigations executed on the running-in of sliding contacts.

## 4.2 Running-in of sliding contacts, macroscopic wear

### 4.2.1 Simulation procedure

The simulation scheme for predicting wear in a sliding contact, schematically depicted in Fig. 4.1, will be compared with the predictive wear models of Podra and Anderson [12], Hegadekatte [13] and Hegadekatte et al. [14-15]. Basically, the model contains three stages in the simulation procedure: determination of the contact pressure, calculation of the wear based on Archard's wear equation and updating of the geometry. The wear simulation lasts until the sliding distance ( $s_{max}$ ) is reached.

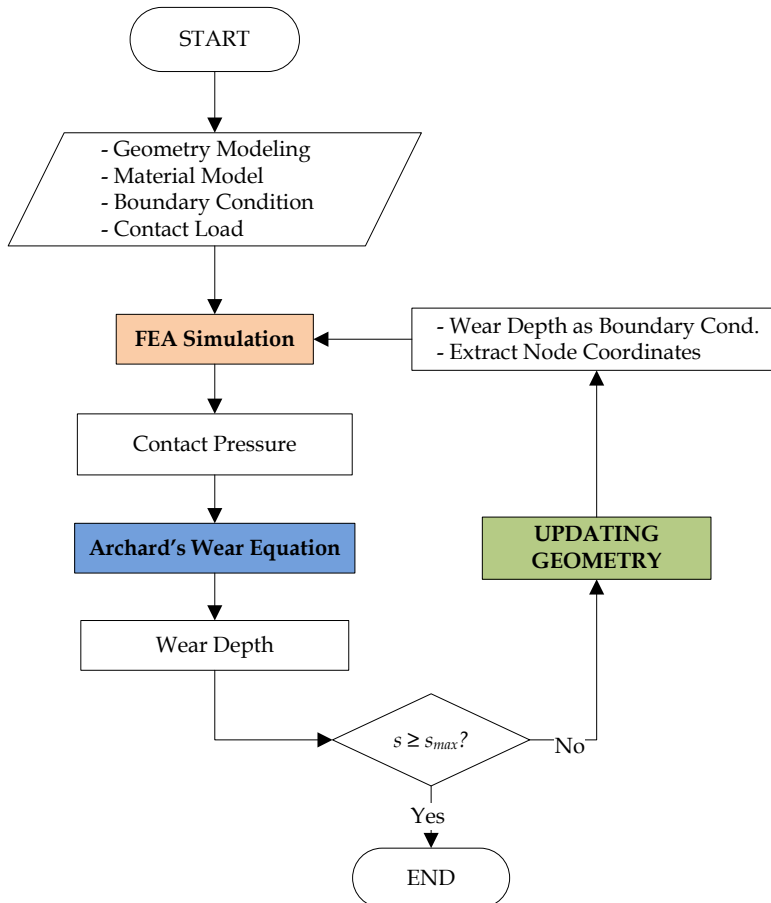


**Figure 4.1:** Flow chart for predicting wear in sliding contacts.

In the first stage, the inputs are the geometry, material model, boundary conditions and contact load. The simulation starts with a finite element analysis to obtain the contact pressure for each node on the contacting surface. Then, the contact pressure is used as input in the second stage for calculating the local wear by employing Archard's wear equation [16]. Here, the wear depth,  $h^w$ , of the contacting system was determined using the incremental sliding distances as well as the wear rate,  $K_D$ , of the system. Third, the geometry of the contact system was updated with the amount of wear,  $h^w$ , calculated in the previous stage. In this stage, the nodes and the boundary conditions are updated. The routine is repeated until a certain defined sliding distance ( $s_{max}$ ) was obtained.

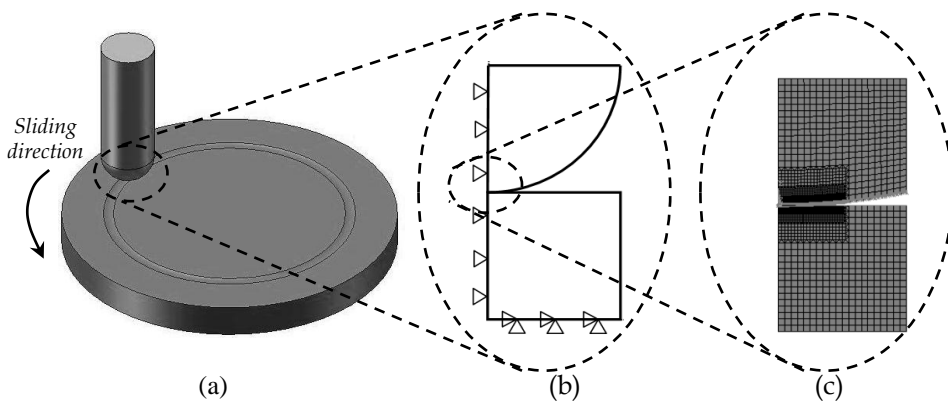


**Figure 4.2:** (a) Pin-on-disc contact system, (b) the model and its boundary conditions, and (c) the finite element mesh and its refined location.

In this section, the FE model of a pin-on-disc contact as schematically shown in Fig. 4.2a was simplified to a contact between an axis-symmetric hemisphere and a flat (Fig 4.2b). The mesh was refined in regions near the contact area of the hemisphere and the flat body, as depicted in Fig 4.2c, to increase the accuracy of the calculation. The simulation does not aim to simulate the entire sliding process of contact system, but instead treats the problem of sliding wear as 'quasi-static' to save the computational expense. In the simulations, the hardness of the material and the wear rate,  $K_D$ , were assumed to be constant during sliding. The discussion on wear focuses on the pin geometry while the wear of the disc is not discussed.

#### 4.2.2 Comparison of the model with the literature

In order to verify the validity of the present model, several simulations were run to be able to compare the wear depth of the present model with those of Podra and Andersson [12] and Hegadekatte [15].

In this comparison the finite element simulations are done for the pin-on-disc configuration (Fig. 4.2). A pin radius  $R_p$  of 0.794 mm was in sliding contact with a disc of  $R_D$  of 4 mm on a wear track  $R_{WT}$  of 3 mm. The thickness of the disc,  $t_D$ , was 1 mm and a contact load  $F_N$  of 200 mN was applied. The material used for pin and disc in the present study was ceramic  $\text{Si}_3\text{N}_4$  with a modulus of elasticity  $E = 304$  GPa, and the Poisson's ratio  $\nu = 0.24$ . A coefficient of friction  $\mu = 0.45$  and specific wear rate  $K_D = 13.5 \times 10^{-9}$  mm<sup>3</sup>/Nm was used. The results are presented in Fig. 4.3 together with the calculations of Hegadekatte et al. [15] and Sarkar [17].

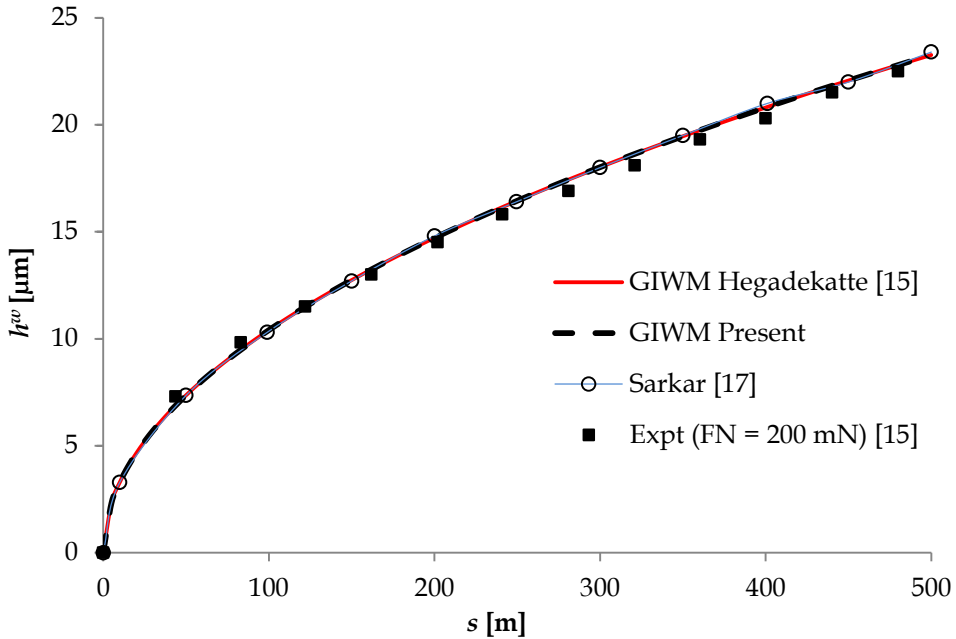
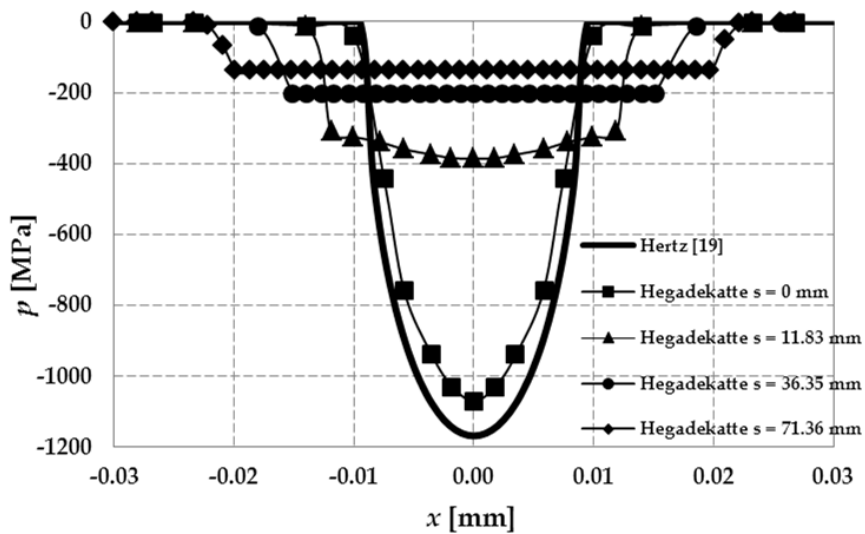


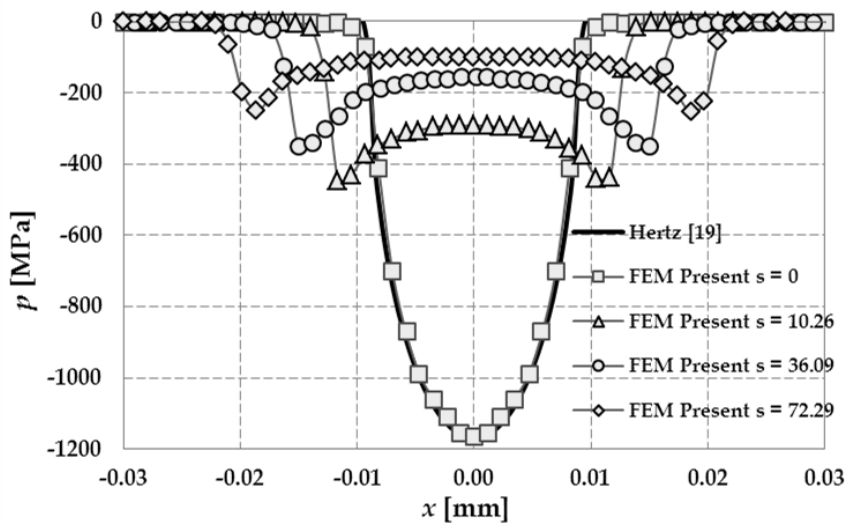
**Figure 4.3:** Comparison of the wear depth predicted by the model of Hegadekatte et al. [15], Sarkar [17] and present model as a function of the sliding distance.

The calculated contact pressure distributions were compared for the present model simulation and of Hegadekatte et al. [14]. Figure 4.4a shows the contact pressure distribution of Hegadekatte et al. [14] and Figure 4.4b shows the present model contact pressure distribution as a function of the sliding distance. Differences in pressure distribution are found; (i) the contact pressure distribution of the present model coincides with the contact pressure of Hertz for  $s = 0$  and (ii) for the consecutive cycles the present model shows similar pressure distributions

as discussed in [18]. When the hemisphere starts to wear and flattening occurs, the maximum in the contact pressure moves from the centre to the edge of the contact area. There is no pressure increase at the edges in Hegadekatte's graphs. From this it is concluded that the present model predicts the contact pressure distribution better.



(a)



(b)

**Figure 4.4:** The comparison of the contact pressure between:  
 (a) Hegadekatte et al. [14] and (b) present FEM model.

Next, the present model is compared with the work of Podra and Andersson [12]. They compared a finite element simulation with experimental data and found good agreement. Figure 4.5 depicts the wear depth evolution for the present results and those of Podra and Andersson [12] as a function of the sliding distance. The present simulation is limited to a sliding distance of 80 mm. The wear depth is predicted with the proposed FEM model and is in good agreement with the FEM model of Podra and Andersson [12] and Hegadekatte model [14-15]. The comparison with the Podra and Andersson model [12] concludes that the present FEM based prediction of the wear depth for sliding contacts is in good agreement with results from the literature.

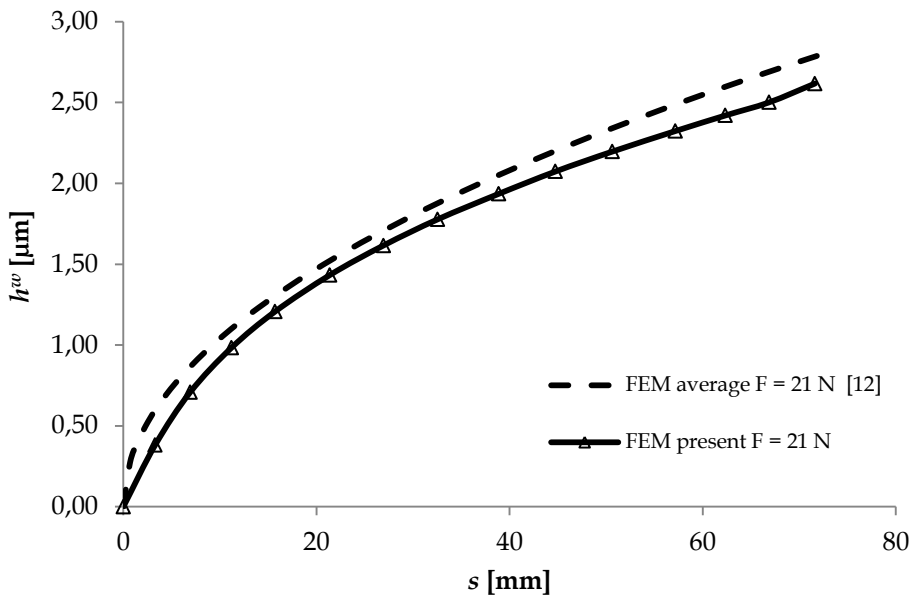


**Figure 4.5:** Comparison of the wear depth of a pin of Podra and Andersson [12] and present model simulation.

#### 4.2.3 Present model simulations and experiments

In the results discussed in the previous section, the predicted wear depth of the pin does not consider the different phases in the wear process, i.e. running-in and steady-state. Pin-on-disc experiments were conducted to determine the running-in wear and steady-state wear. Pin-on-disc tests of AISI 52100 versus AISI 52100 were carried out with a normal load,  $F_N$ , of 15 N, sliding velocity,  $v$ , of 0.005 m/s and a ball radius,  $R_P$  of 5 mm.

Using the model, the contact pressure distributions are calculated for the above described test as a function of the sliding distance, using a specific wear rate



of  $2.7 \times 10^{-7} \text{ mm}^3/\text{Nm}$ . The results are presented in Fig. 4.6. Two contact pressures are presented, namely the contact pressure at the centre of the pressure distribution ( $p_{\text{centre}}$ ) and the average contact pressure ( $p_{\text{av}}$ ). At the start of the sliding contact, where the running-in phase occurs, the  $p_{\text{centre}}$  and  $p_a$  are initially high and decrease gradually, until a more or less “steady-state” is reached. It is found that the average contact pressure reaches its “steady-state” after approximately 62 m sliding.

The contact pressure distribution at the contact area as a function of the sliding distance is depicted in Fig. 4.7. The contact pressure distribution follows the Hertz rule at the initial sliding contact then it decreases as the sliding distance increases. The increase of contact area due to wear is followed by the pressure increase at the edge of the pin. The contact pressure distribution explains the facts in Fig. 4.6 where the contact pressure at the centre node is initially higher than the average contact pressure, and after the transition between the running-in to steady-state phase it occurs vice versa.

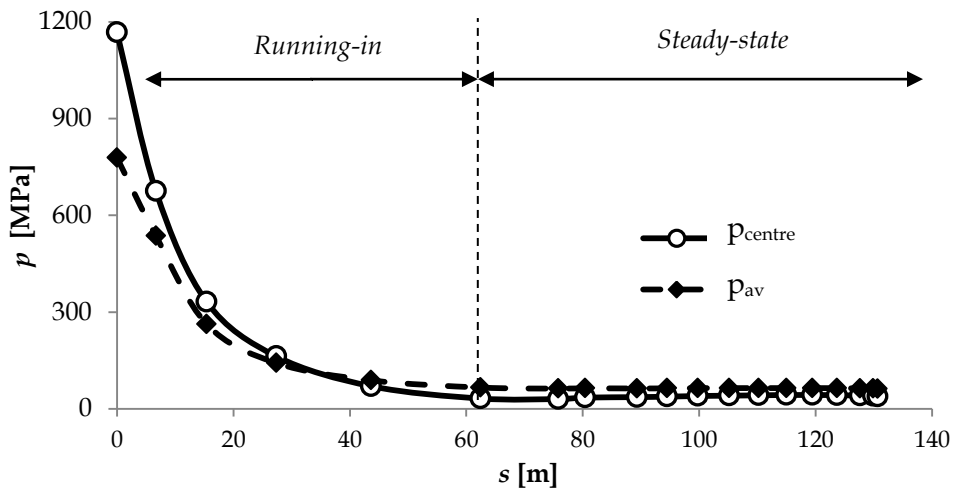


**Figure 4.6:** Determining the transition from the running-in phase to the steady-state phase based on contact pressure obtained by FEA.

Further, in Fig 4.8 the calculated and measured wear depth as a function of the sliding distance is plotted. Initially the calculated wear depth, using a constant specific wear rate, increases more rapidly than the measured wear depth with increasing sliding distance, but ultimately they coincide. The wear depth and wear rate, defined as the ratio of wear depth over unit sliding distance, as a function of the sliding distance is shown. Figures 4.9 and 4.10 depict the transition of the running-in to the “steady-state” phase of the Podra and Andersson [12] and Hegadekatte et al. [14] simulations based on the proposed method. The contact pressure evolution is plotted as a function of the sliding distance. Based on this, it

can be concluded that the model is able to determine the transition from a running-in phase to more or less steady-state phase.

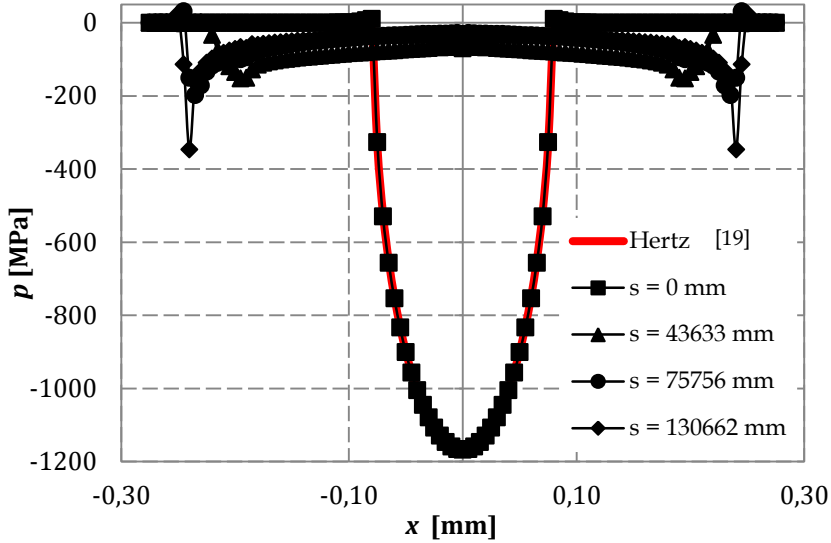


**Figure 4.7:** Contact pressure distribution of the present simulations as a function of the sliding distance.

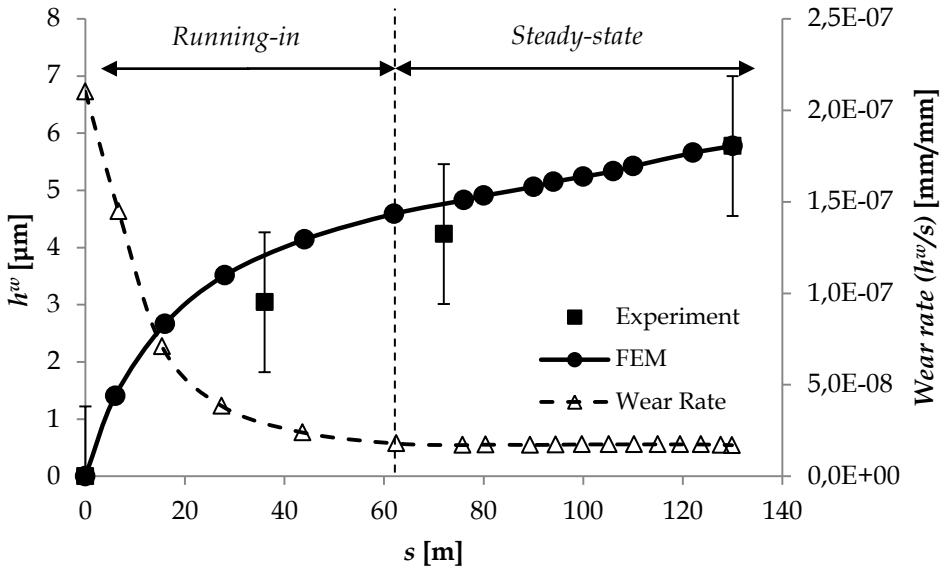


**Figure 4.8:** Wear depth as a function of sliding distance. Present model simulations versus experimental results, sliding contact of AISI 52100 vs AISI 52100,  $F_N = 15$  N, and  $R_p = 5$  mm.

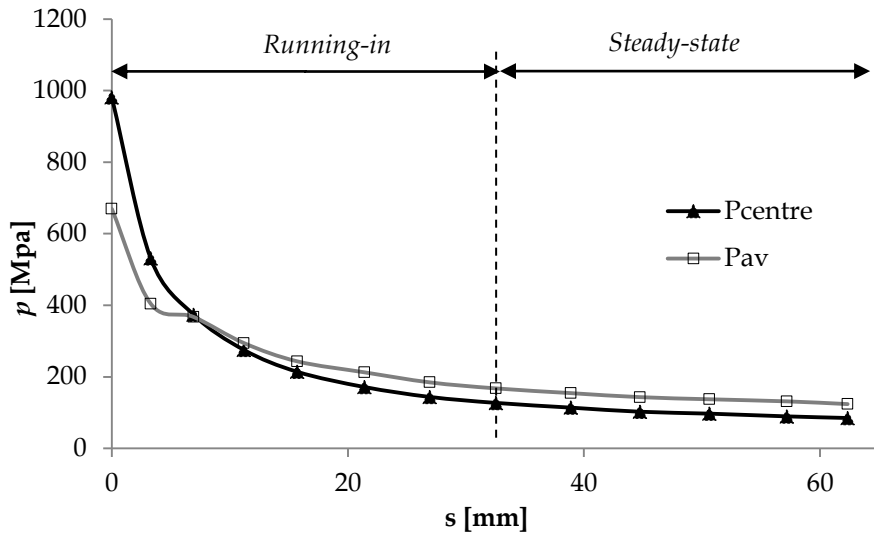


**Figure 4.9:** Determining the transition of the running-in to steady-state phase, Podra and Andersson [12], using the present model and  $F_N = 21$  N,  $R_{\text{ball}} = 5$  mm,  $E = 210$  GPa,  $\nu = 0.3$  and  $K_D = 1.33 \times 10^{-10}$  mm<sup>3</sup>/Nm.

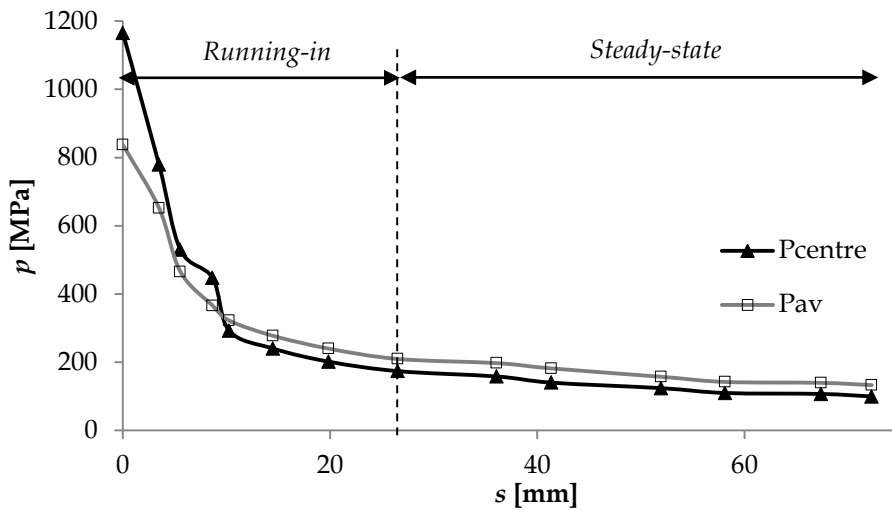


**Figure 4.10:** Determining the transition of the running-in to steady-state phase, Hegadekatte et al. [14], using the present model and  $F_N = 200$  mN,  $R_{\text{ball}} = 0.746$  mm and  $K_D = 13.5 \times 10^{-9}$  mm<sup>3</sup>/Nm.

### 4.3 Running-in of sliding rough surfaces, microscopic wear

#### 4.3.1 Running-in of sliding artificial rough surfaces

##### 4.3.1.1 Simulation procedure

In this section, wear of an artificial rough surface is investigated. The surface is represented by an artificial roughness in which the asperities are uniformly distributed spherical shaped asperities. The rough pin is in sliding contact with the flat smooth surface, as depicted in Fig. 4.11. The mesh is refined near the contact area for increasing the simulation accuracy.

The geometry, material properties and contact load of the pin-on-disc contact system is the same as in Section 4.2.2. The previous wear modelling, in Section 4.2.2, focused on the macroscopic geometry change of a component that wears. This section focuses on the microscopic wear of the asperities on the pin. The combination of Archard's wear equation and FEA, as proposed in Fig. 4.1, is employed to predict the wear of the asperities. Two cases of simulation were conducted in this section where the circumferential distance of the asperities and initial surface roughness are listed in Table 4.1.

**Table 4.1:** Dimension of the pin and the asperities.

Descriptions	Dimensions	
	$R_{as} = 25 \mu\text{m}$	$R_{as} = 50 \mu\text{m}$
Circumferential distance between asperities	9.69 $\mu\text{m}$	13.85 $\mu\text{m}$
Initial surface roughness of the pin ( $R_a$ )	0.348 $\mu\text{m}$	0.340 $\mu\text{m}$

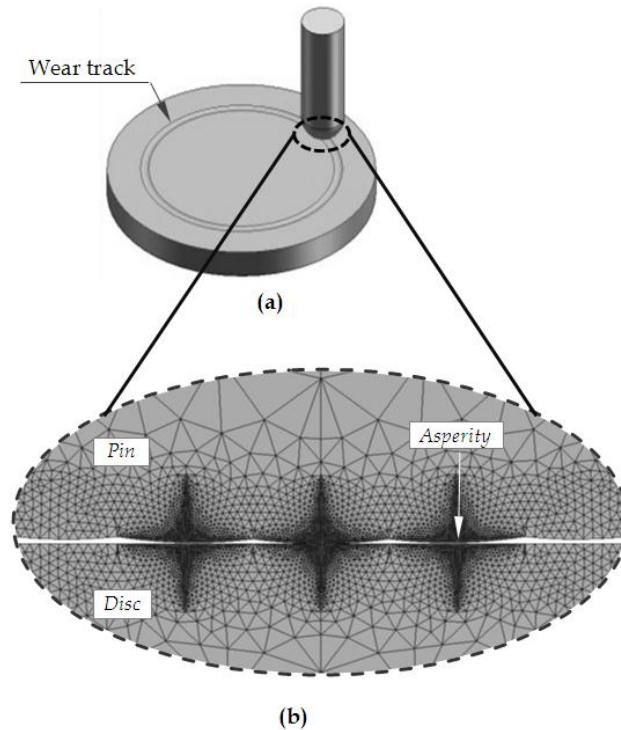


**Figure 4.11:** (a) Pin-on-disc contact system where a rough pin is in sliding contact with a smooth flat disc. (b) The zoom-in view depicts the contact in more detail and the mesh refinement in and near the contact area.

#### 4.3.1.2 Calculated contact pressure and wear depth

The contact area and contact pressure of the pin surface on asperity level for  $R_{as} = 25 \mu\text{m}$  and  $R_{as} = 50 \mu\text{m}$  are shown in Figs. 4.12 and 4.13, respectively. The asperity at the centre of the contact is loaded more than the asperities located further away from the centre, due to the geometrical setting of the asperities on the curved hemispherical pin. In the case of a conformal contact, the loading of the asperities was uniform. More asperities are involved in the contact for  $R_{as} = 25 \mu\text{m}$ .

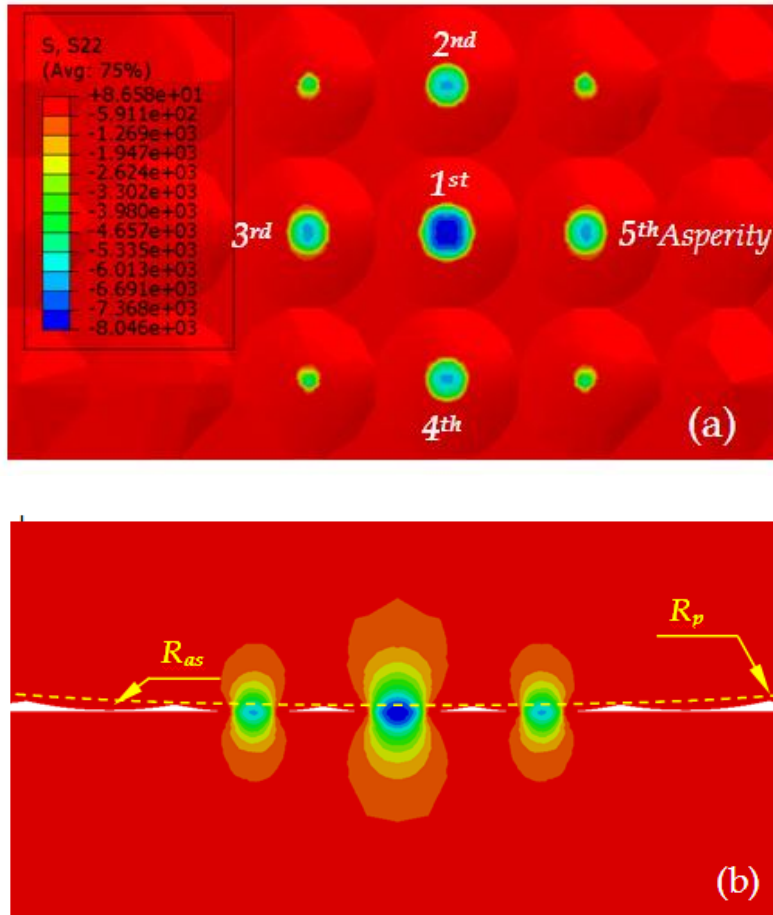


**Figure 4.12:** (a) Contact area of pin surface on asperity level and (b) pressure distribution in cross-sectional view of the rough pin with  $R_{as} = 25 \mu\text{m}$ , the insert gives the pressure in MPa.

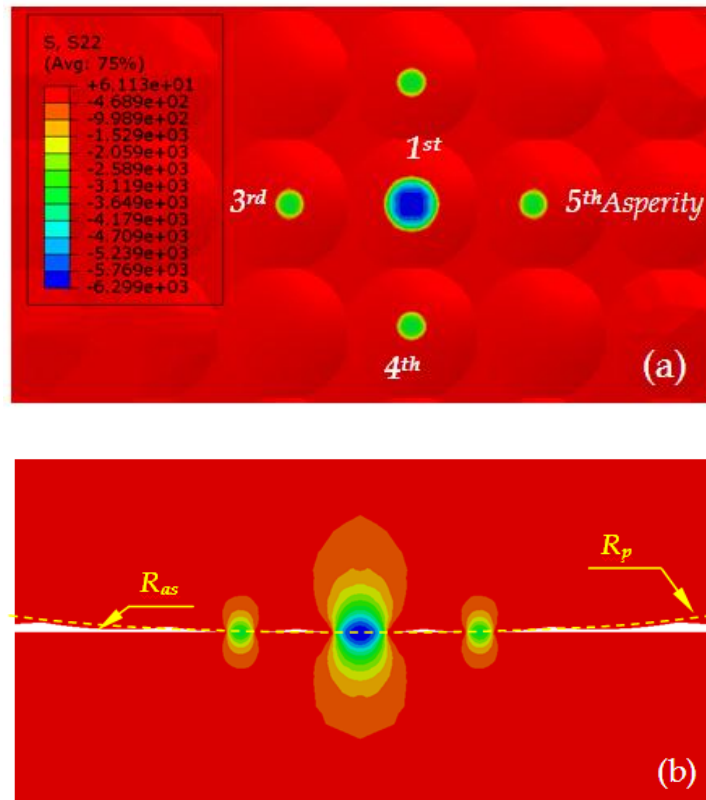


**Figure 4.13:** (a) Contact area of pin surface on the asperity level and (b) pressure distribution in cross-sectional view of the rough pin for  $R_{as} = 50 \mu\text{m}$ .

The contact pressure distribution of the rough pin on asperity levels for  $R_{as} = 25 \mu\text{m}$  and  $R_{as} = 50 \mu\text{m}$  are depicted in Fig. 4.14 and 4.15. From these figures, it becomes clear that with sliding distance the real contact area increases. Further, the pressure distribution across an asperity changes significantly from an initial Hertzian pressure distribution to a pressure distribution showing a pressure rise at the edge of each worn asperity. Due to wear of the asperities located at the centre of the macroscopic contact, more and more surrounding asperities are involved in carrying the load. The number of asperities in contact, for  $R_{as} = 25 \mu\text{m}$ , is higher due to the higher deformation of the asperities and the smaller circumferential distance between the asperities.

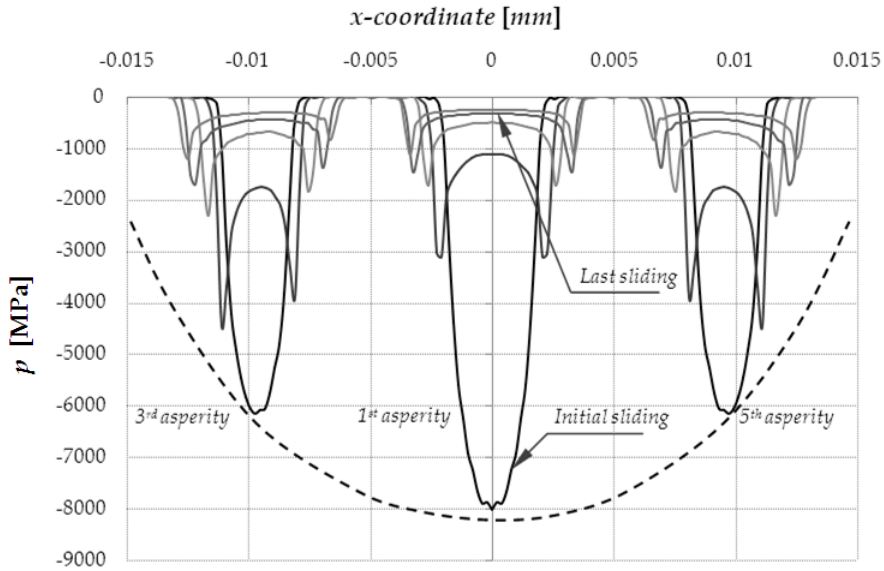


**Figure 4.14:** The contact pressure distribution on asperity level as the sliding distance increases,  $R_{as} = 25 \mu\text{m}$ .

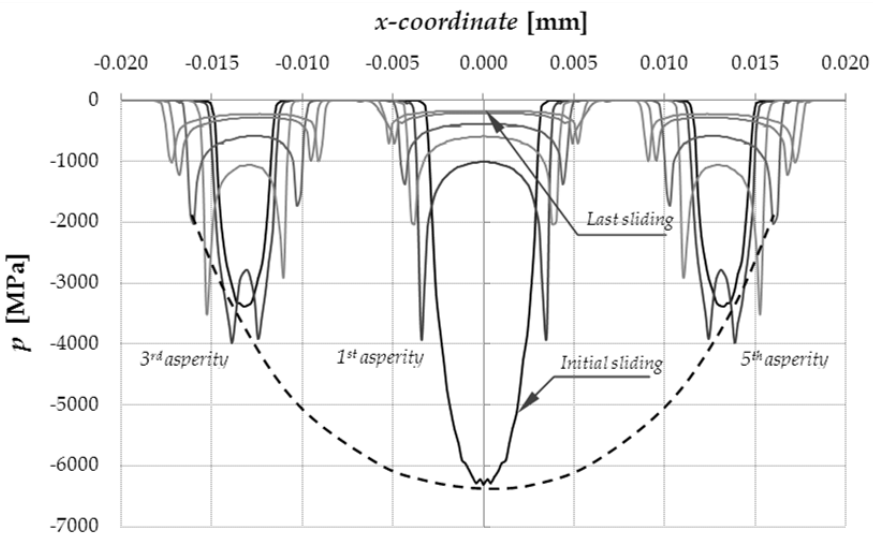


**Figure 4.15:** The contact pressure evolution on asperity level as the sliding distance increases,  $R_{as} = 50 \mu\text{m}$ .

The computed wear of the asperities is presented in Fig. 4.16. As expected, the wear of the asperity at the centre of contact area is higher than the surrounding asperities. Due to the symmetric artificial rough surface, wear of the 2<sup>nd</sup>, 3<sup>rd</sup>, 4<sup>th</sup> and



5<sup>th</sup> asperity is the same (see Fig. 4.15). At the start of the sliding process, the wear, reduction of the asperity height, is high (running-in phase) and then tends to stabilize (steady-state phase).

The initial surface roughness ( $R_a$ ), for the two cases of simulation, is nearly the same, as depicted in Fig. 4.17 and Table 4.1. The decrease in surface roughness ( $R_a$ ), in the running-in phase of the sliding process, is high and tends to stabilize in the steady-state phase due to the conformal shape of the asperities.

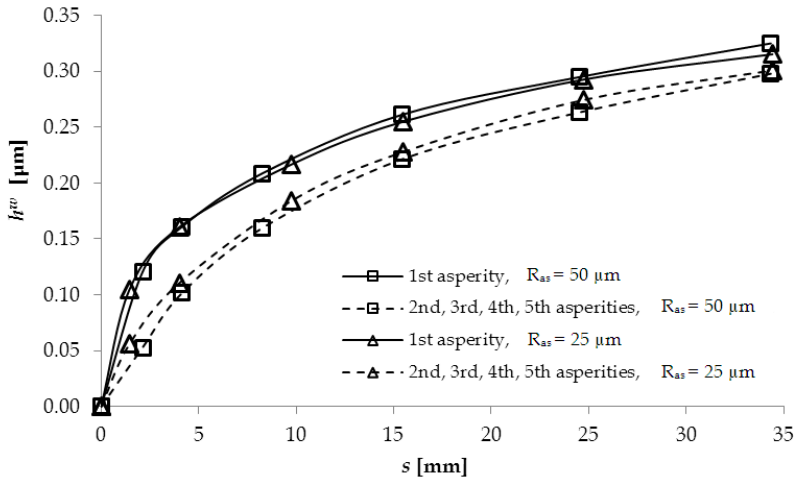


**Figure 4.16:** The wear depth of asperities of the rough pin as a function of sliding distance.

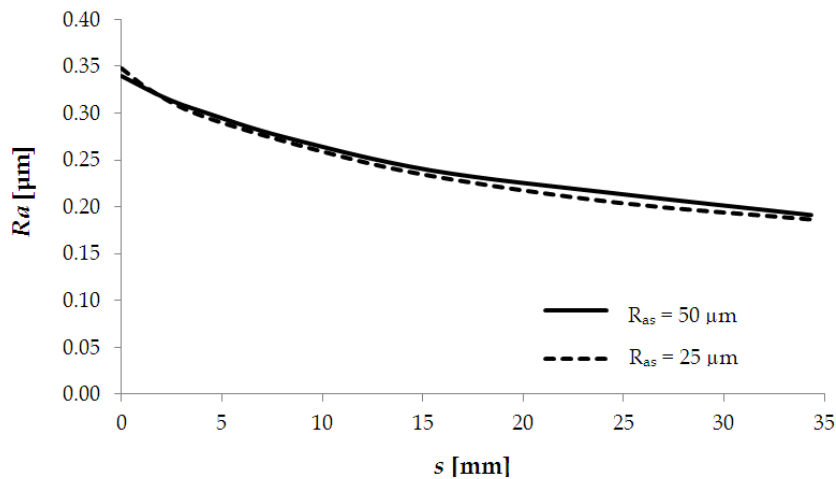


**Figure 4.17:** Surface roughness as a function of sliding distance.

The evolution of the average contact pressure of the asperities as a function of sliding distance is shown in Fig. 4.18. The decrease of the average contact pressure of the asperities is initially high, then tends to stabilize into the “steady-state” phase. The wear of the asperities, as the sliding distance increases, produces a wider contact area and induces conformal contact at the asperities.

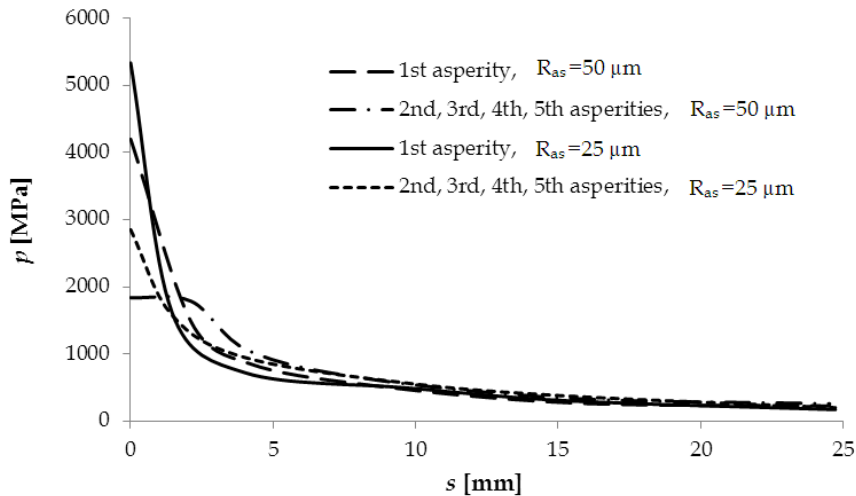


**Figure 4.18:** Average contact pressure as a function of sliding distance.

## 4.3.2 Running-in of sliding real rough surfaces

### 4.3.2.1 Simulation procedure

The change in surface topography due to wear in a sliding contact is discussed in this section, considering a real rough surface. The rough surface is generated using the method as discussed in Appendix B and is superimposed on the pin tip. This rough pin is in sliding contact with a flat smooth surface, as depicted in Fig. 4.19.

The geometry, material properties and contact load of the pin-on-disc contact system is the same as described in Section 4.2.2. The previous running-in calculations focused on the microscopic change of an artificial rough surface. This section focuses on the microscopic wear of the asperities on the pin. The combination of Archard’s wear equation and FEA, as proposed in Fig. 4.1, is employed to predict the wear of the asperities and as a result the change in micro-geometry, i.e. the roughness.

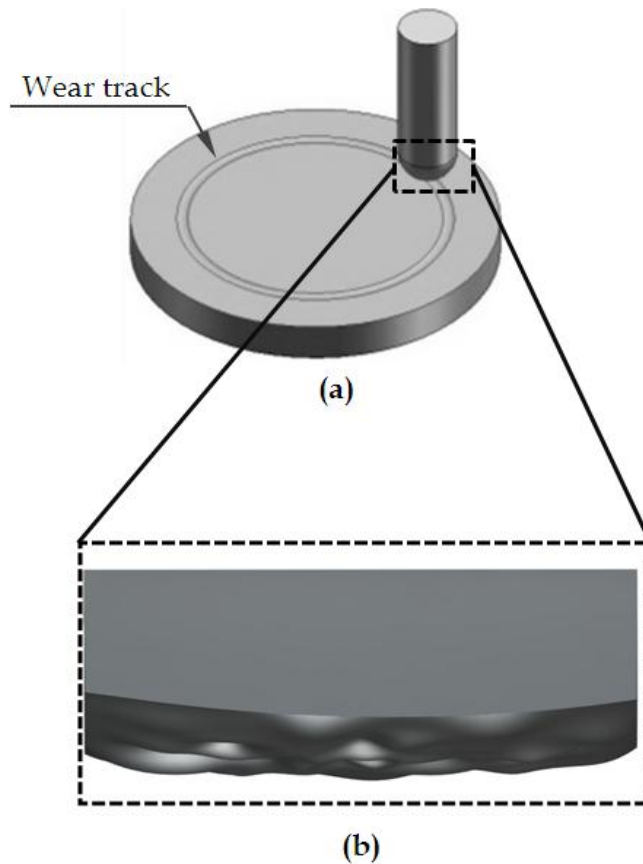


**Figure 4.19:** (a) Pin-on-disc contact system in which a rough pin is in sliding contact with a smooth flat disc. (b) Zoom-in view of the rough pin.

#### 4.3.2.2 Calculated contact pressure and wear depth

The initial contact area ( $s = 0$  mm) of the rough pin in contact with the flat counter surface is depicted in Fig. 4.20, showing four asperities, which are marked as asperity 1-4. During sliding contact, the contact area and the contact pressure of the rough pin change as the sliding distance proceeds.

Figure 4.21 shows the contact area of the asperities for  $s = 15$  mm. Due to the change in micro-geometry, new asperities come into contact, marked as 5<sup>th</sup> asperity, as the sliding distance increases. Wear during sliding contact truncates the higher asperities and a larger contact area is found.

The evolution of the contact pressure for one of the contacting asperities during sliding contact is depicted in Figs. 4.22 to 4.25. The contact pressure is plotted on a local  $x$  coordinate for depicting the contact width of the asperity.

The average contact pressure of the asperities as well as the average contact pressure of asperity 1 is depicted as a function of sliding distance in Fig. 4.26. In Fig. 4.27 the decrease in surface roughness ( $Ra$ ) is given. These figures show that a “transition” to the steady-state phase takes place at approximately 3 mm sliding distance.

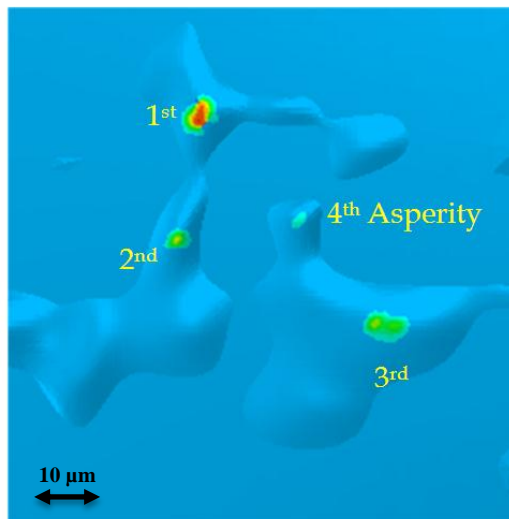


**Figure 4.20:** Contact area on asperity level at the initial sliding contact ( $s = 0$  mm).

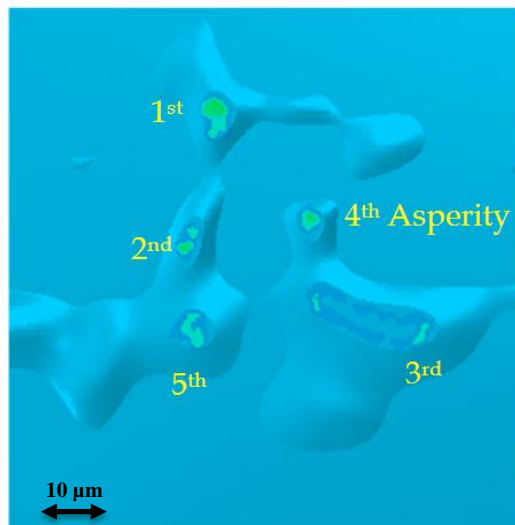


**Figure 4.21:** Contact area on asperity level after a sliding distance of  $s = 15$  mm.

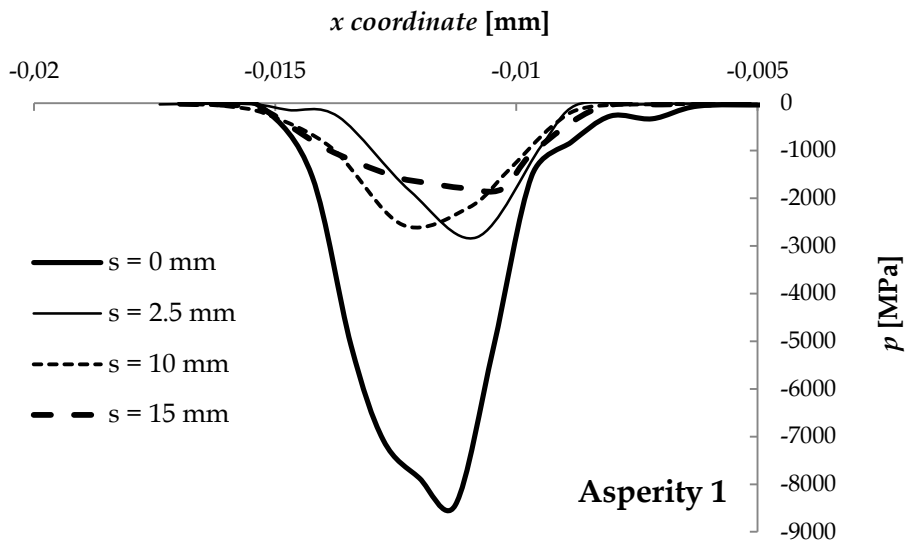


**Figure 4.22:** The contact pressure distribution on 1<sup>st</sup> asperity as a function of sliding distance.

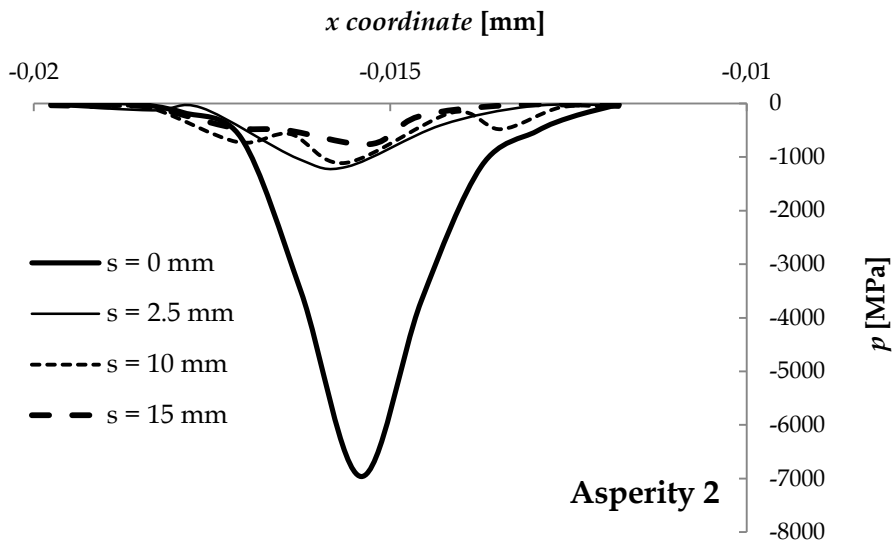


**Figure 4.23:** The contact pressure distribution on 2<sup>nd</sup> asperity as a function of sliding distance.

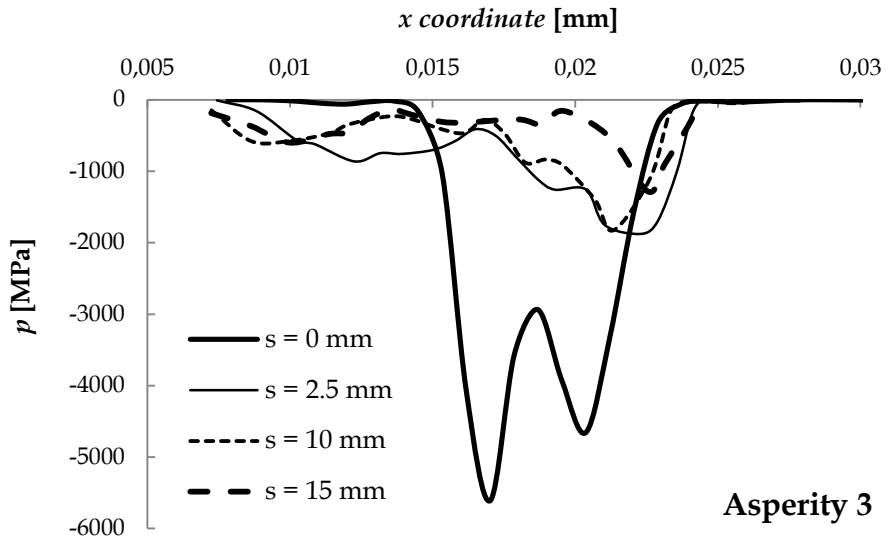


**Figure 4.24:** The contact pressure distribution on 3<sup>rd</sup> asperity as a function of sliding distance.

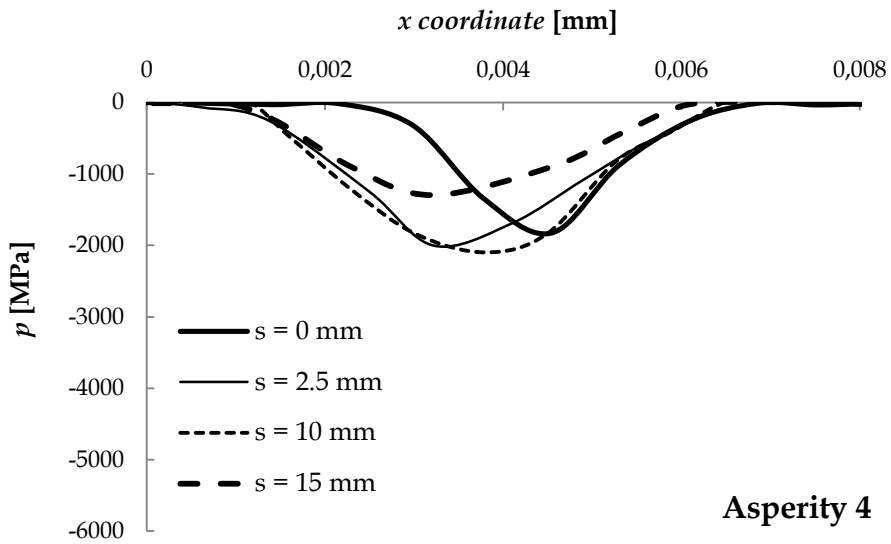


**Figure 4.25:** The contact pressure distribution on 4<sup>th</sup> asperity as a function of sliding distance.

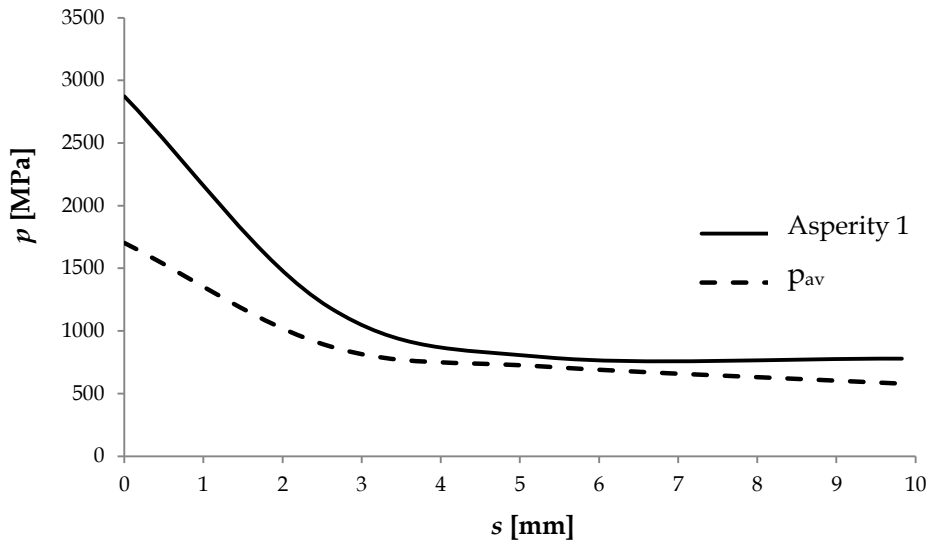


**Figure 4.26:** Average contact pressure as a function of sliding distance.

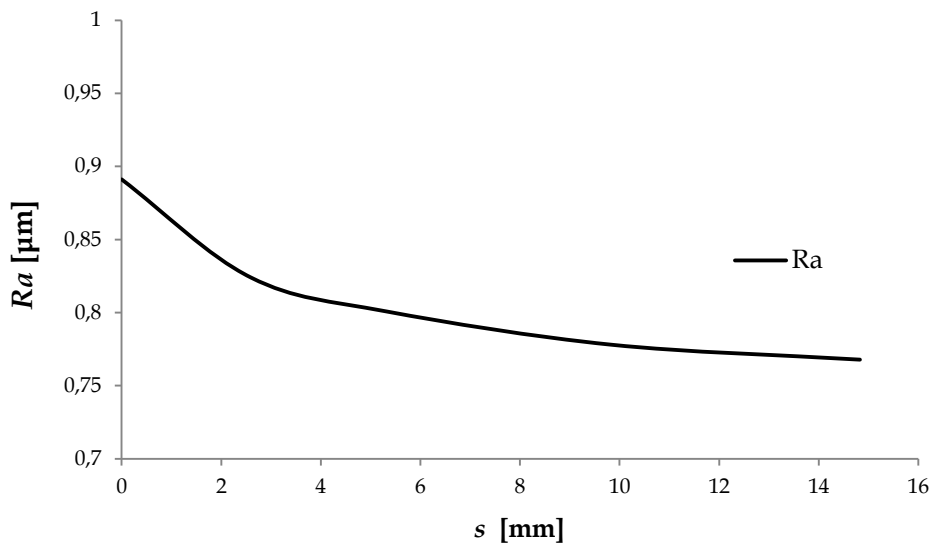


**Figure 4.27:** Surface roughness as a function of sliding distance.

#### 4.4 Concluding remarks

In this chapter, finite element simulations have been conducted for sliding contacts which cover contact pressure evolution and change in the topography of sliding contacts. The results have been verified with results from the literature. Good agreement is found. The finite element model combined with Archard's wear formula is a useful tool to study the running-in of a surface on roughness level. Obviously the transition between the running-in phase and the steady-state phase for sliding contacts cannot be captured with a single parameter likewise for the rolling contact situation. Wear is an ongoing process.

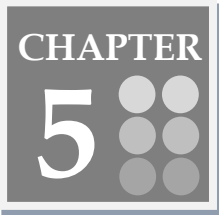
#### References

- [1] Lin, J.-Y. and Cheng, H.S., 1989, "An analytical model for dynamic wear," *ASME Journal of Tribology*, 111, pp. 468-474.
- [2] Hu, Y.Z., Li, N. and Tonder, K., 1991, "A dynamic system model for lubricated sliding wear and running-in," *ASME Journal of Tribology*, 113, No. 3, pp. 499-505.
- [3] Sugimura, J., Kimura, Y. and Amino, K., 1987, "Analysis of the topography changes due to wear-geometry of the running-in process," *JSLE*, 31(11), pp. 813-820.
- [4] Jeng, Y. R. and Gao, C.-C., 2000, "Changes of surface topography during wear for surfaces with different height distributions," *Tribology Transactions*, 43, pp. 749-757.
- [5] Jeng, Y.R., Lin, Z.W. and Shyu, S.H., 2004, "Changes of surface topography during running-in process," *ASME Journal of Tribology*, 126, pp. 620-625.
- [6] Kumar, R., Prakash, B. and Sethuramiah, A., 2002, "A systematic methodology to characterize the running-in and steady-state processes," *Wear*, 252, pp. 445-453.
- [7] Blau, P. J., 1987, "A model for run-in and other transitions in sliding friction," *ASME Journal of Tribology*, 109, pp. 537-544.
- [8] Blau, P.J., 2005, "On the nature of running-in," *Tribology International*, 38, pp. 1007-1012.
- [9] Nogueira, I., Dias, A.M., Gras, R., and Progri, R., 2002, "An experimental model for mixed friction during running-in," *Wear*, 253, pp. 541-549.
- [10] Dienwiebel, M. and Pohlmann, K., 2007, "Nanoscale evolution of sliding metal surface during running-in," *Tribology Letters*, 27, pp. 255-260.
- [11] Luo, Q., 2010, "Origin of friction in running-in sliding wear of nitride coatings," *Tribology Letters*, 37, pp. 529-539.



- [12] Podra, P. and Andersson, S., 1999, "Simulating sliding wear with finite element method," *Tribology International*, 32, pp. 71-81.
- [13] Hegadekatte, V., 2006, *Modeling and Simulation of Dry Sliding Wear for Micro-machine Applications*, PhD thesis, University of Karlsruhe, Karlsruhe, Germany.
- [14] Hegadekatte, V., Huber, N. and Kraft, O., 2006, "Modeling and simulation of wear in a pin on disc tribometer," *Tribology Letters*, 24, pp. 51-60.
- [15] Hegadekatte, V., Kurzenhauser, S., Huber, N. and Kraft, O., 2008, "A predictive modeling scheme for wear in tribometers," *Tribology International*, 41, pp. 1020-1031.
- [16] Archard, J.F., 1953, "Contact and rubbing of flat surfaces," *Journal of Applied Physics*, 24, pp. 981-988.
- [17] Sarkar, A.D., 1980, *Friction and Wear*, Academic Press, London, UK.
- [18] Johnson, K.L., 1985, *Contact Mechanics*, Cambridge University Press, Cambridge, UK.
- [19] Hertz, H., 1882, "Ueber die beruehrung fester elastischer koerper," *J Reine Angew. Math.*, 92, pp. 156-71. (in German).





## Running-in of Rolling-Sliding Contacts

---

### 5.1 Introduction

In the study of rolling-sliding contacts of mechanical components such as roller-bearings [1], cam and followers [2], gears [3] and micro gears [4], wear is regarded as a surface phenomenon that has been identified as a critical factor for controlling the lifetime of these components. However, the investigations on wear of rolling-sliding contacts were mostly conducted when operating in the steady-state phase without considering the running-in phase. During running-in, the friction and wear between two contacting bodies may vary considerably over time.

In the investigations conducted in the past decades in developing running-in models and performing running-in experiments, attention was paid to observing changes in the coefficient of friction [5-7] and the surface topography [8-10] during running-in. However, there are other parameters whose contribution cannot be neglected for a successful running-in phase. Hsu et al. [11] observed that besides surface roughness, contact pressure and interface layer, the establishment of an effective lubricating film is also adjusted in the transient period of running-in to the steady-state condition. These parameter adjustments induce surface conformity, oxide film formation, material transfer, lubricant reaction products, martensitic phase transformations and subsurface microstructure reorientation.

Recently, Argatov and Fadin [12] indicated that based on mathematical modelling, using the theory of elasticity in conjunction with Archard's law of wear, the contact pressure is very important in determining the end of the running-in phase and the start of the steady-state phase. The rolling-sliding contact is simulated using the finite element method to analyse wear, change in surface topography and contact pressure as a function of sliding distance/time.

The content of this chapter on running-in of rolling-sliding contacts is divided into six sections. Section 5.2 deals with the rolling-sliding contact models

proposed in the literature and the validation of the present finite element based model. Then, the running-in of an artificial rolling-sliding contact is discussed based on the contact pressure evolution as a function of the number of overrollings/cycles in Section 5.3. The running-in of a real rough rolling-sliding contact is simulated and validated with experimental results in section 5.4. In section 5.5 the running-in of lubricated rolling-sliding contacts is presented. Finally, concluding remarks are given in Section 5.6 on the running-in of rolling-sliding contacts on macro-scale and micro-scale.

## 5.2 Modelling wear in rolling-sliding contacts: a comparison

In this section, macroscopic wear and contact pressure development in rolling-sliding contacts is presented based on the finite element simulation model and these are compared with the aforementioned models [13-14] in chapter 2.

### 5.2.1 Analytical model

Hegadekatte et al. [13] introduced the Global Increment Wear model (GIWM) for sliding contacts for calculating the local wear depth as follows:

$$h_{i+1}^w = K_D p_i \Delta s_i + h_i^w \quad (5.1)$$

where  $K_D = K/H$  is the specific wear rate,  $p$  is the contact pressure and  $\Delta s$  is the interval of the sliding distance,  $h^w$  is the current wear depth. The equation for calculating the wear in rolling-sliding contacts proposed by Andersson [15], who took the slip between two rollers into account and modified the GIWM equation, reads as follows:

$$h_{i+1} = h_i + \frac{\Delta t_i |V_1 - V_2|}{2\pi R_i} 2K_D p_i a_i \quad (5.2)$$

where  $\Delta t$  refers to a given time increment,  $R$  is the radius of the disc where wear takes place,  $a$  is the contact width and  $V$  indicates the rolling velocity where the subscript 1 and 2 denotes surface 1 and surface 2. Subscribe  $i$  denotes the number of rolling-sliding rotations. The model of Andersson [16], which has been validated with experiments, is modified and combined with GIWM in the present rolling-sliding model.

With the present model for rolling-sliding contacts, using the simulation parameters and data of Hegadekatte et al. [13], several simulations were performed to study the effect of load, slip and rolling velocity on wear and contact pressure.

### 5.2.1.1 Validation with Hegadekatte et al. [13]

The simulation is performed based on parameters of Hegadekatte et al. [13] as listed in Table 5.1. The simulation procedure has been discussed in subsection 2.5.3.

**Table 5.1:** Parameters used in the simulation of the present model based on Hegadekatte et al. [13].

Radius of ball (1)	$R_{ball} = 4 \text{ mm}$
Radius of lower rigid cylinder (2)	$R_{cyl} = 4 \text{ mm}$
Normal load	$F_N = 300 \text{ N}$
Young's modulus	$E_1 = E_2 = 152 \text{ GPa}$
Poisson's ratio	$\nu_1 = \nu_2 = 0.32$
Velocity of upper ball	$V_1 = 800 \text{ mm/s}$
Velocity of lower cylinder	$V_2 = 880 \text{ mm/s}$
Friction coefficient	$\mu = 0.6$
Wear rate	$K_D = 1 \times 10^{-5} \text{ mm}^3/\text{Nm}$

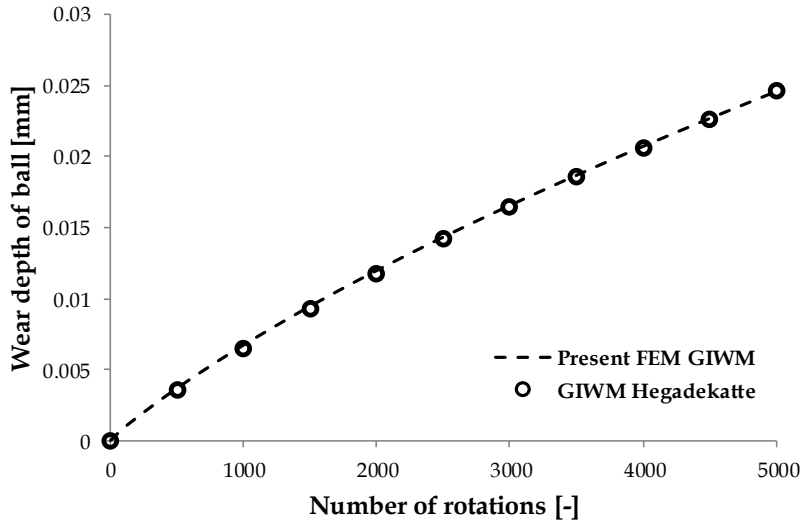


**Figure 5.1:** Comparison of the wear depth of ball as a function of number of rotations of the present FEM GIWM and Hegadekatte [13].

The comparison of the calculated wear depth of the present FEM GIWM model and the results of Hegadekatte et al. [13] are shown in Fig. 5.1. It shows that the present FEM GIWM model predicts wear rather well.

### 5.2.1.2 The effect of slip, load, and rolling velocity

Simulations were performed by varying the slip, contact load and rolling velocity. The effect of the parameters on the wear depth of the ball and the contact pressure are discussed.

The contact load was set at 150 N, 300 N and 450 N respectively. The contact load is the parameter which is varied in the simulations, whereas the others remained constant, as listed in Table 5.1. The effect of contact load on the wear depth and contact pressure is depicted in Fig. 5.2 and Fig. 5.3. A decrease of the contact pressure is shown in Fig. 5.3. The “steady-state” value of the contact pressure, according to Argatov and Fadin [12], is found after 500 rotations for the three loads.

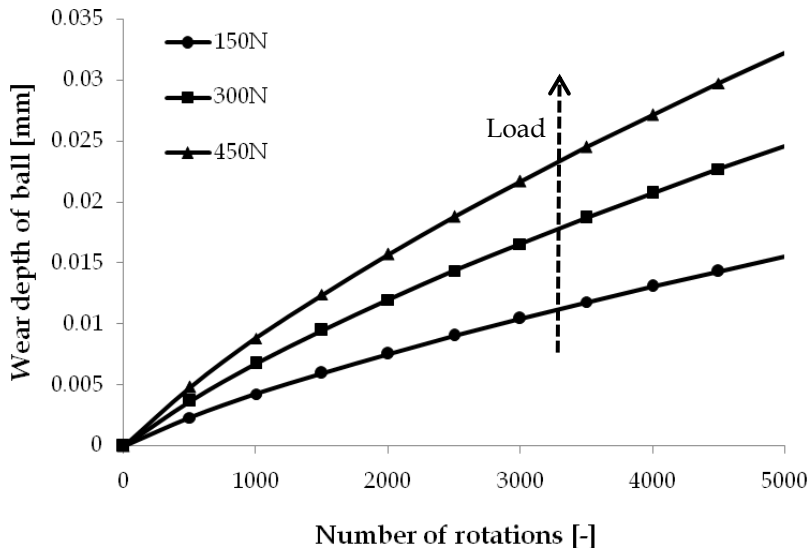


**Figure 5.2:** The effect of load on the wear depth as a function of number of rotations. The operational conditions are given in Table 5.1,  $V_1 = 800 \text{ mm/s}$  and slip = 10 %.

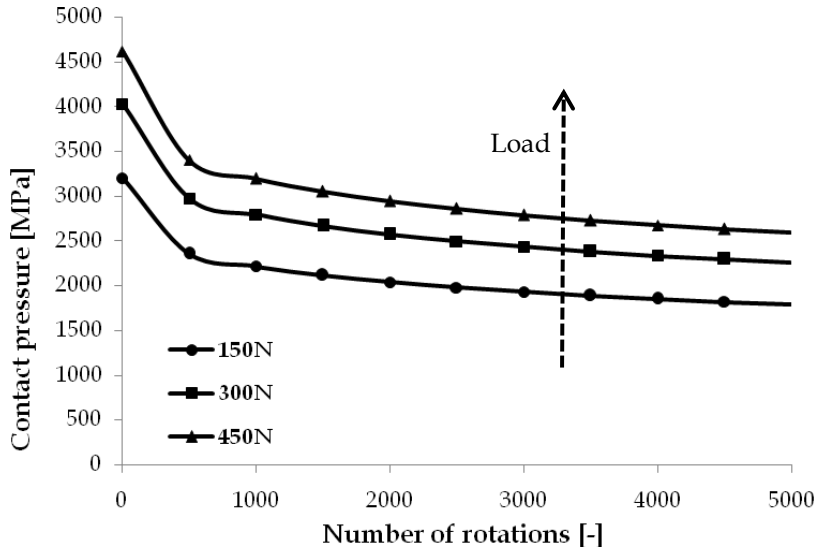


**Figure 5.3:** The effect of load on the contact pressure as a function of number of rotations. The operational conditions are given in Table 5.1,  $V_{ball} = 800$  mm/s and slip = 10 %.

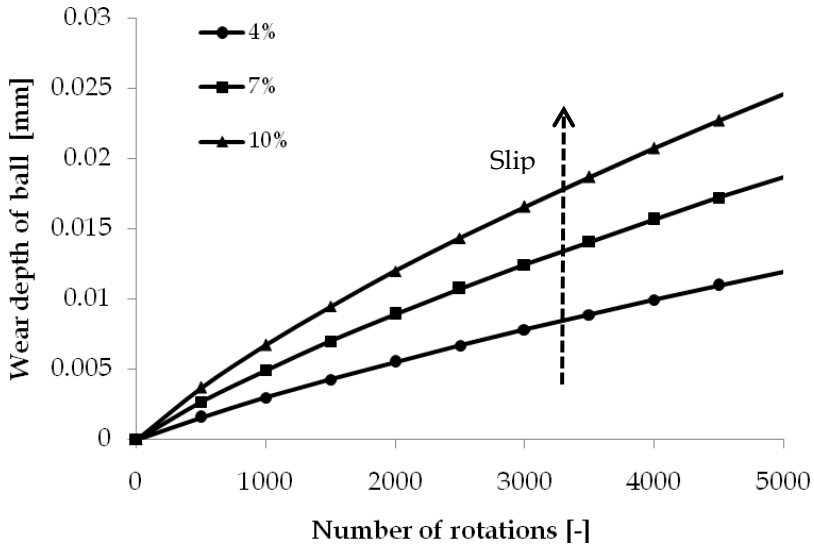


**Figure 5.4:** The effect of slip on the wear depth as a function of number of rotations. The operational conditions are given in Table 5.1,  $F_N = 300$  N and  $V_{ball} = 800$  mm/s.

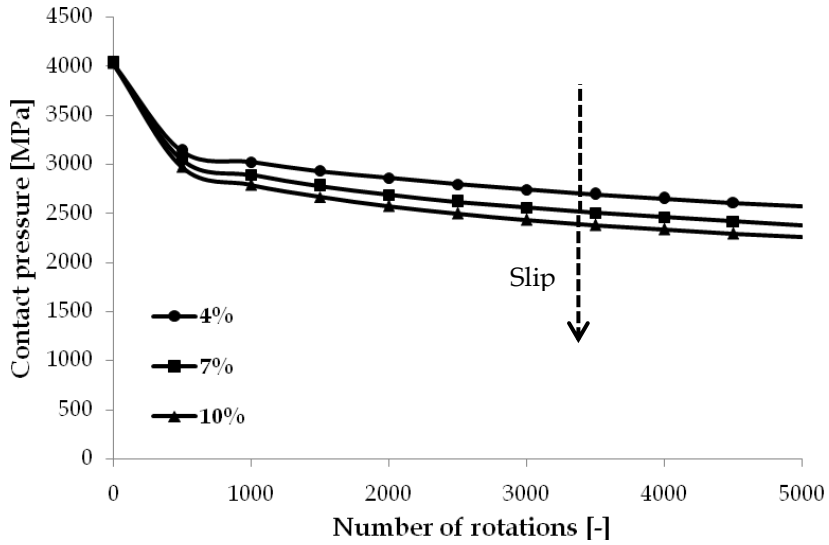


**Figure 5.5:** The effect of slip on the contact pressure as a function of number of rotations. The operational conditions are given in Table 5.1,  $F_N = 300$  N and  $V_{ball} = 800$  mm/s.

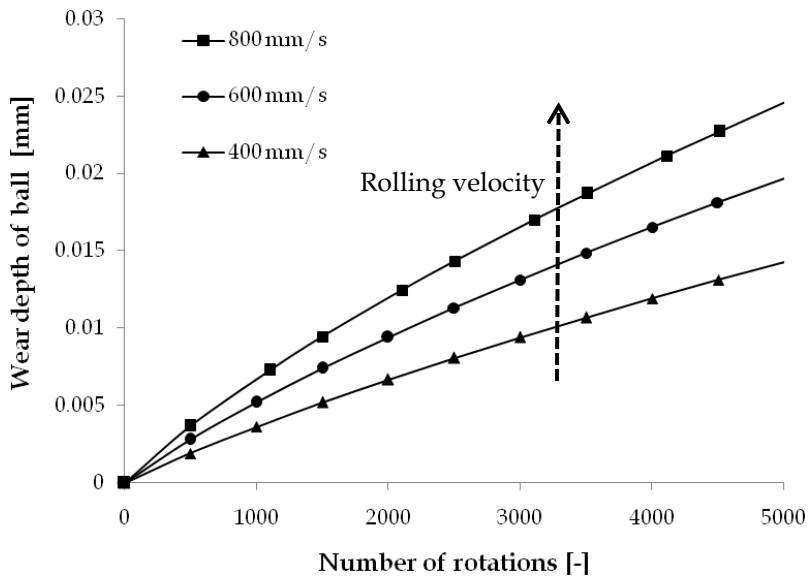


**Figure 5.6:** The effect of rolling velocity on the wear depth as a function of number of rotations. The operational conditions are given in Table 5.1,  $F_N = 300$  N and slip = 10 %.



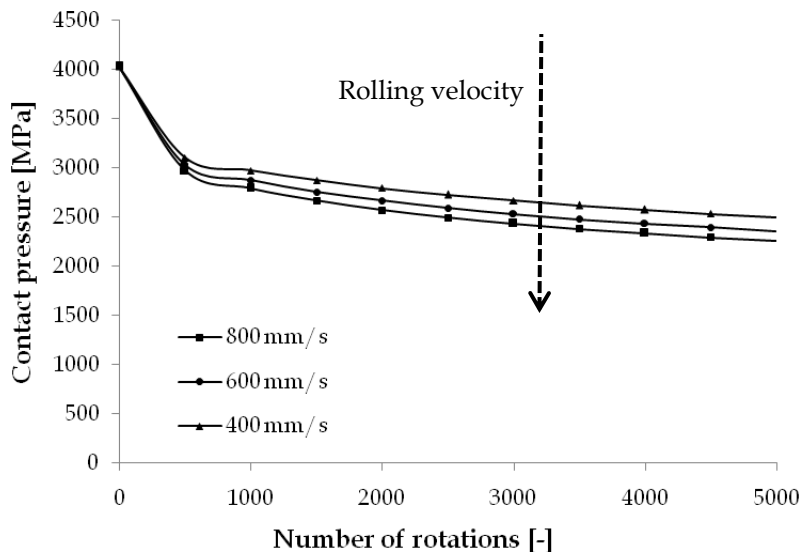


**Figure 5.7:** The effect of rolling velocity on the contact pressure as a function of number of rotations. The operational conditions are given in Table 5.1,  $F_N = 300$  N and slip = 10 %.

The effect of slip on the wear depth and the contact pressure was simulated for slip values of 4%, 7% and 10 %. The slip was varied by changing the velocity of the lower surface whilst the upper surface, as well as the other parameters in Table 5.1, were kept constant. The effect of the slip on the wear depth and average contact pressure can be seen in Fig. 5.4 and Fig. 5.5, respectively. The results show that the wear increases with increasing slip, which is due to an increase in sliding distance per rotation. The decrease in the “steady-state” contact pressure with increasing slip, as shown in Fig. 5.5, is a consequence due to an increase in wear.

The effect of the rolling velocity on wear depth and contact pressure is depicted in Fig. 5.6 and Fig. 5.7. The rolling velocity is the only parameter which varied in these simulations whereas the other parameters remained unchanged, as listed in Table 5.1. The rolling velocity of the ball is 400 mm/s, 600 mm/s and 800 mm/s, respectively and the applied slip is set at 10%.

When the rolling velocity increases, the wear depth is found to be higher and the contact pressure is lower. The same occurrence with the slip was noticed. The driving parameter is the increase of the sliding distance.

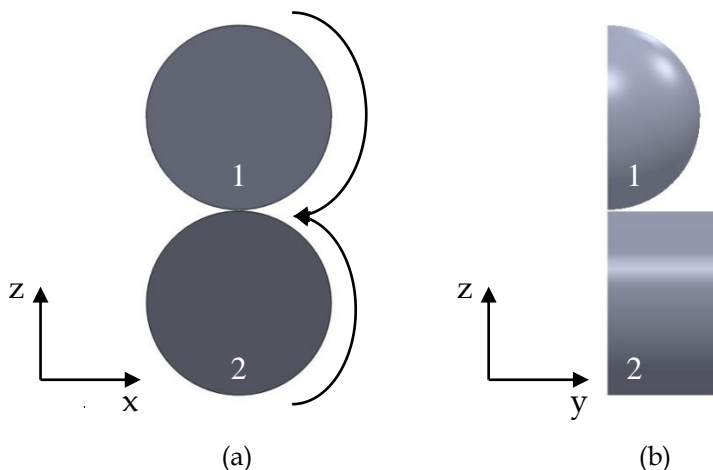
## 5.2.2 Finite element simulation

The discussion in Chapter 4 showed that the finite element analysis was suitable in predicting the wear in sliding contacts. The proposal is to calculate the wear using FEA using ABAQUS for a sliding contact, using the modified GIWM equation Eq. (5.2), to predict the wear for the rolling-sliding contact situation. Two simulations were performed to compare the previous model of the GIWM model [13], FEM model [13] and BEM model [14].

### 5.2.2.1 Comparison of GIWM and FEM [13]

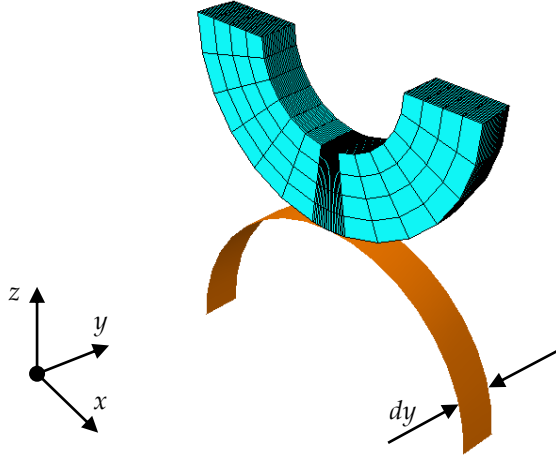
Hegadekotte et al. [13] developed three methods in predicting wear in rolling-sliding contacts, namely the analytical GIWM model, the FEM model UMESHMOTION and the Wear-Processor. Both UMESHMOTION and Wear-Processor simulations made use of ABAQUS with the computational code modification as discussed in Chapter 2. In order to validate the present wear calculation using finite element simulation in rolling-sliding contacts, a comparison of the present result and GIWM, UMESHMOTION and Wear-Processor is presented in this subsection.

Figure 2.9 depicts schematically the contact of the two-disc machine of Hegadekotte et al. [13]. This contact situation was used in predicting the wear depth using GIWM, UMESHMOTION and Wear-Processor. In the present simulation, the contact situation, as shown in Fig. 5.8, consists of a ball in rolling-sliding contact with a cylinder.



**Figure 5.8:** Two-disc configuration used in the FEM simulations (a) X-Z plane (b) Y-Z plane.

The simplification of the contact model, as depicted in Fig. 5.9, was used to reduce the computational time during simulation. The cylinder was modelled as rigid and the upper ball was modelled as an elastic-plastic deformable material. The value for the dimensions and parameters in the present simulation is listed in Table 5.1, as used in the previous section.



**Figure 5.9:** Simplification of the contact model of Fig. 5.8.

The finite element simulation scheme is shown in Fig. 5.10. The Archard wear equation was modified for the rolling-sliding contact. For every rotation of the ball, the wear was calculated as follows:

$$h_{j+1} = K_D \int_{\phi=0}^{\phi=2\pi} p r d\phi + h_j \quad (5.3)$$

where  $r$  is the radius of the ball and  $\phi$  is the angle of rotation. The calculation of the wear depth using Eq. (5.3) will hold for all the nodes lying along the same circumference (streamline). For a given time increment  $\Delta t_j$ , the wear depth of the observed roller with a radius,  $R$ , can then be written as shown in Eq. (5.4). The iteration is repeated until the sliding distance reaches the value set and the number of iterations depends on the rolling distance for each iteration.

$$h_{j+1} = K_D \frac{\Delta t_j |V_1 - V_2|}{2\pi R_j} \int_{\phi=0}^{\phi=2\pi} p r d\phi + h_j \quad (5.4)$$

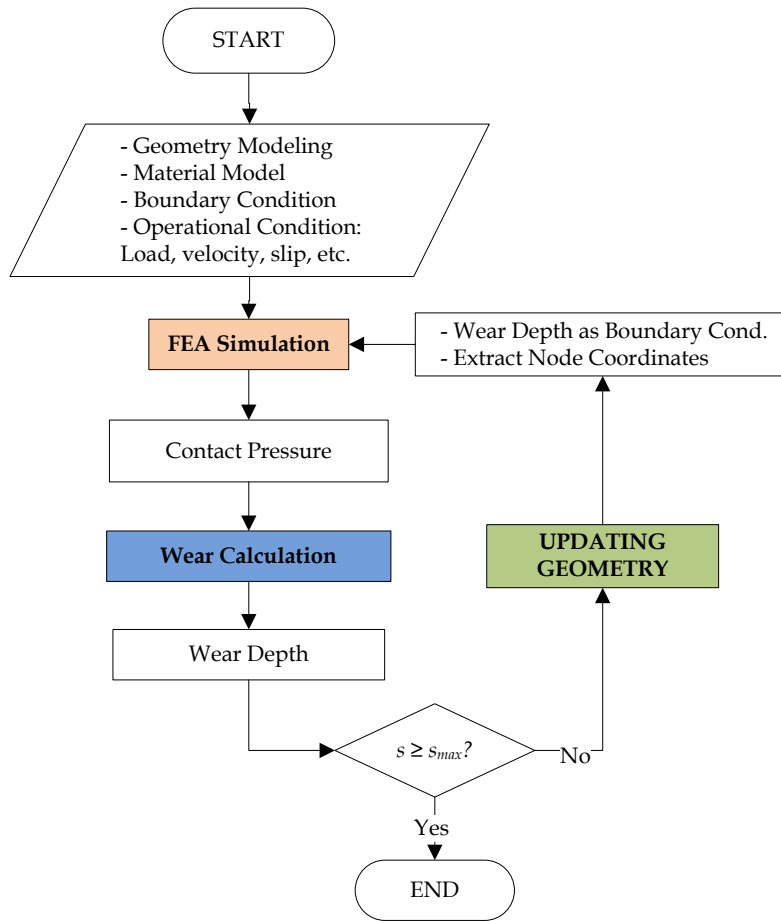


**Figure 5.10:** The scheme for the finite element simulation.

The result of the contact pressure in the X-Y plane (Fig. 5.9) of the simulation is shown in Fig. 5.11. The red colour indicates the highest contact pressure, located at the centre of the contact area. The local contact pressure along the contact was put into the modified Archard wear equation to calculate the local wear depth. The geometry was updated for the next iteration step. The iteration was repeated until the sliding distance reaches the pre-set sliding distance.

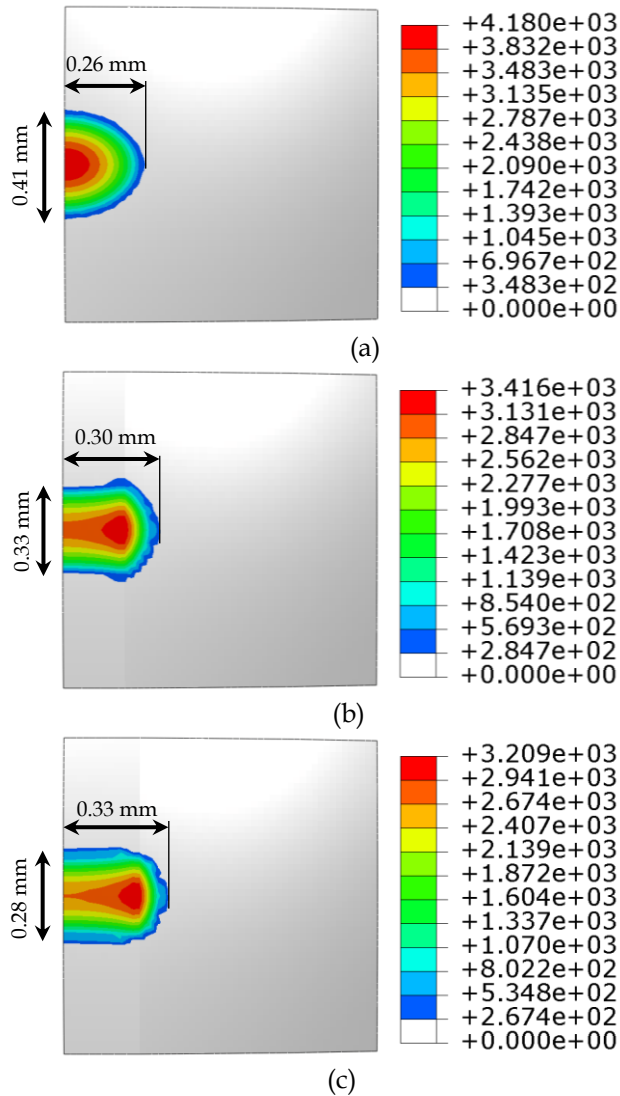


**Figure 5.11:** Contact pressure (MPa) as a function of number of overrollings: (a)  $n = 0$ , (b)  $n = 500$  and (c)  $n = 1000$ . The parameters used in the simulations are given in Table 5.1.

The contact area becomes wider and hardly changes in sliding direction. The increase in contact area results in a decrease of the contact pressure. The plot of the wear depth as a function of number of rotations is depicted in Fig. 5.12 where the present simulation, Wear-Processor, UMESHMOTION and GIWM are compared. The present result has a very good correlation with the UMESHMOTION model and a good agreement is found with the Wear-Processor model and the GIWM model. The change in average contact pressure during

rolling-sliding is given in Fig. 5.13, where the comparison with the Wear-Processor is shown.

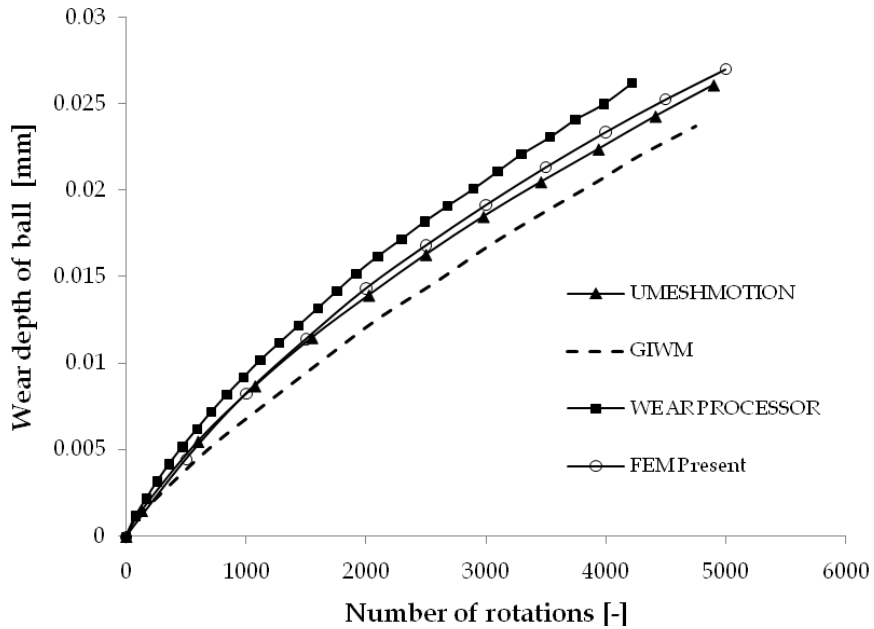


**Figure 5.12:** Comparison of the wear depth as a function of number of rotations between the present FEM model and Hegadekotte et al. [13]: Wear-Processor, UMESHMOTION and GIWM.

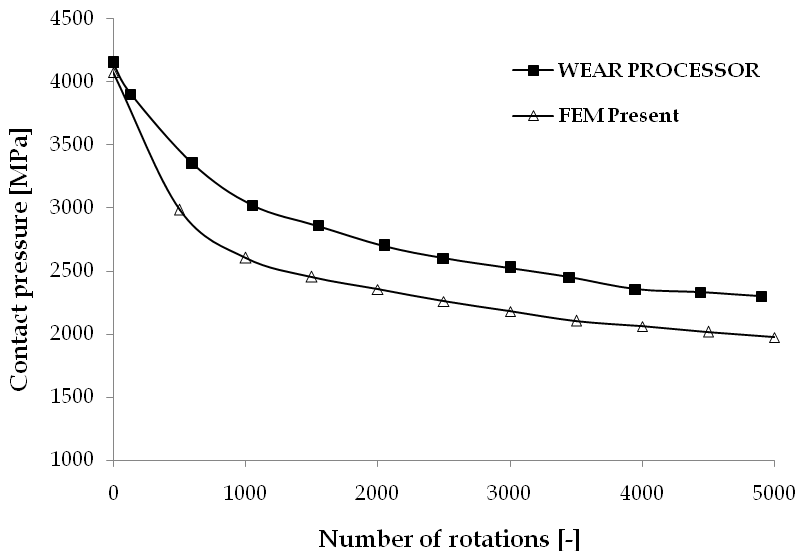


**Figure 5.13:** The calculated average contact pressure as a function of the number of rotations, FEM model results compared with the Wear-Processor results of Hegadekatte et al. [13].

### 5.2.2.2 Comparison with BEM

In this section, the present finite element model is compared with the boundary element method as proposed by Rodríguez-Tembleque et al. [14] in calculating the wear depth of a rolling-sliding contact. The rolling-sliding contact simulated is schematically given in Fig. 5.14 and the values for the parameters used are listed in Table 5.2 [14].

The present simulation of the rolling-sliding contact is conducted using ABAQUS. The contact and simulation procedure is the same as described in the previous section, see Fig. 5.9 and Fig. 5.10. The results with respect to contact area and contact pressure are depicted in Fig. 5.15 and show the same trend as found in the previous section. The large increase in contact length is due to a much larger radius of the ellipsoid perpendicular to the sliding direction, as is the case for the previous simulation. As found before, the increase in track width is rather limited.

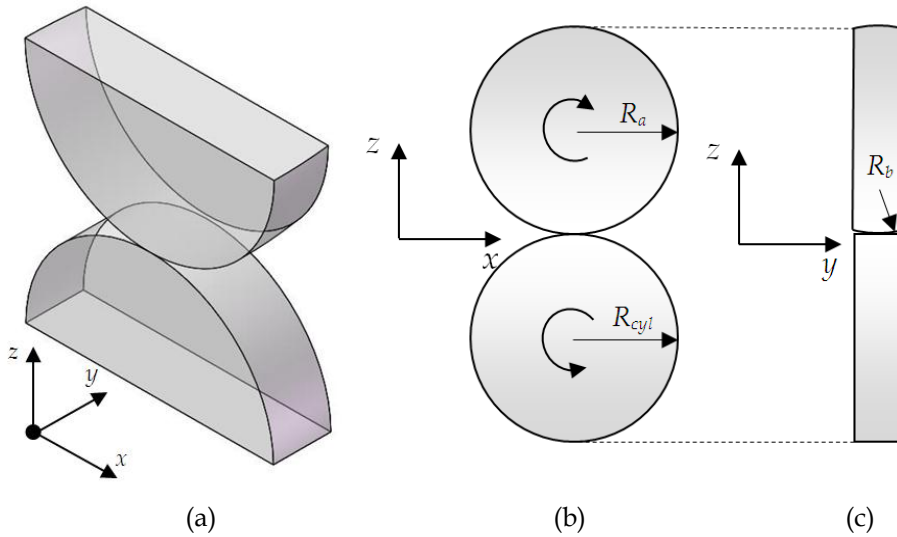


**Figure 5.14:** Contact situation used in the FEM simulations. (a) isometric view (b) Y-Z plane and (c) X-Y plane

**Table 5.2:** The parameters for the BEM simulation, after Rodríguez-Tembleque et al. [14].

Radii of upper ellipsoid	$R_a = 32.5 \text{ mm}$ and $R_b = 125 \text{ mm}$
Radius of lower cylinder	$R_{cyl} = 32.3 \text{ mm}$
Normal load	$F_N = 300 \text{ N}$
Speed of ellipsoid	$n_1 = 300 \text{ rev/min}$
Young's modulus	$E_1 = E_2 = 208 \text{ GPa}$
Poisson's ratio	$\nu_1 = \nu_2 = 0.3$
Frictional coefficient	$\mu = 0.6$
Wear rate	$K_D = 2 \times 10^{-6} \text{ mm}^3/\text{Nm}$
Slip	0.5%

The wear depth curves obtained by using BEM [14] and the present simulation are plotted in Fig. 5.16. Good agreement is found for the two models in predicting the wear depth.



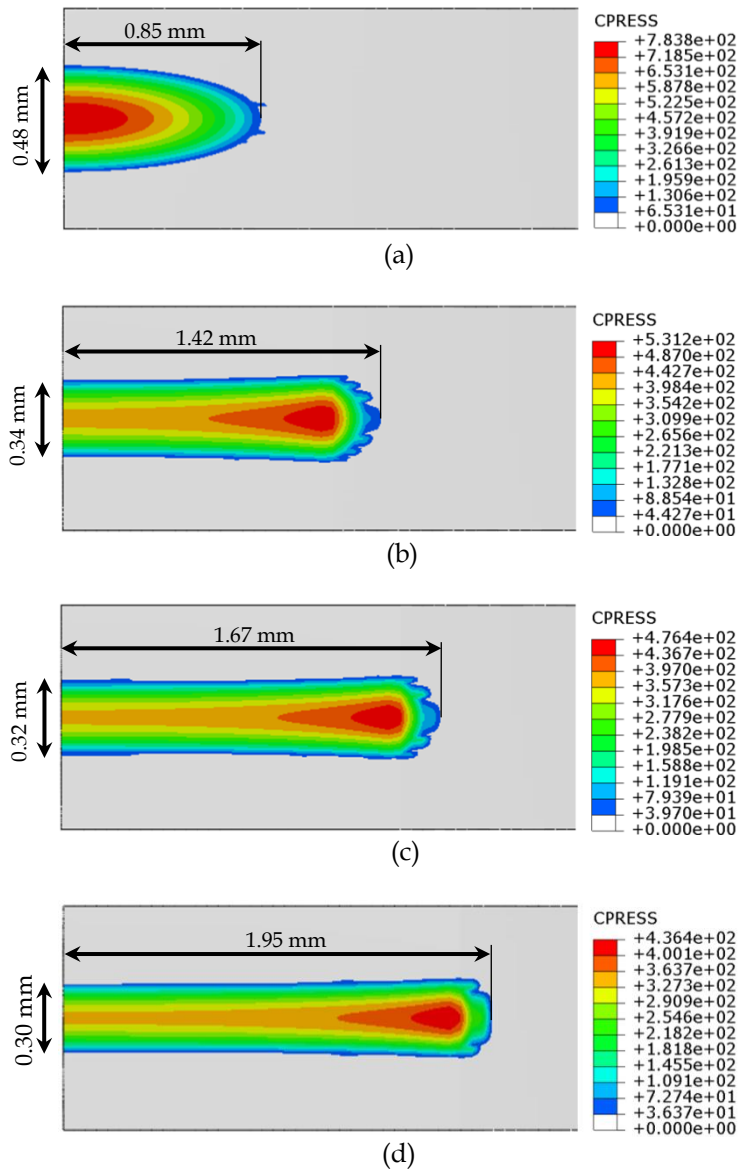


**Figure 5.15:** The evolution of the contact size and contact pressure (MPa) during rolling-sliding after: (a) start, (b) 3,000 revolutions, (c) 6,000 revolutions and (d) 10,000 revolutions. The parameters used in the simulations are given in Table 5.2.

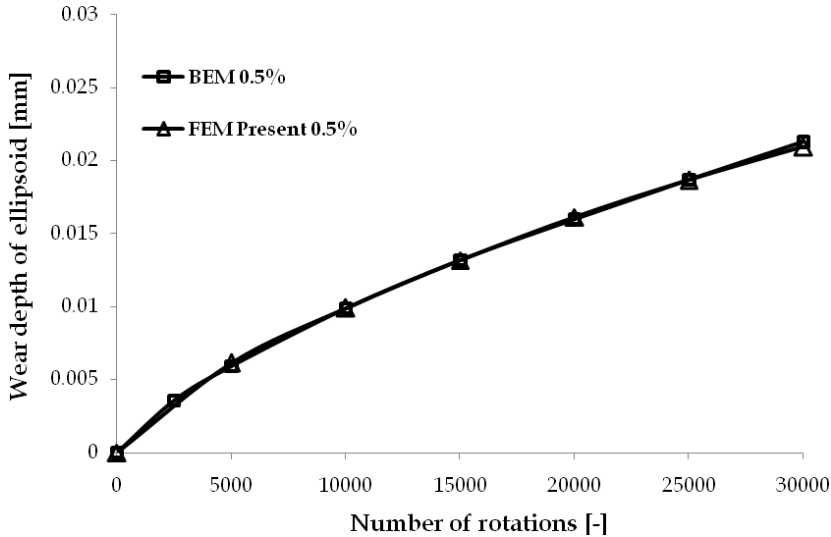


**Figure 5.16:** Wear depth of the ellipsoid versus number of rotations during rolling-sliding contact for: BEM model [14] and the present FEM model.

### 5.3 Running-in of artificial rough rolling-sliding contact

#### 5.3.1 Simulation procedure

In the previous section, the focus was on macroscopically wearing components. In this section, finite element simulations are done for the two-disc configuration with an artificial rough surface of the upper sphere and a smooth lower cylinder. An arrangement of asperities covers the upper disc surface as depicted in Fig. 5.17. The mesh is refined near the local contact area for increasing simulation accuracy. The operational conditions of the two-disc system is the same as used in Table 5.1, where the rolling-sliding contact was discussed for the wear that takes place on macro-scale. In this section, a contact load  $F_N$  of 100 N and radius of artificial asperity,  $R_{as}$ , 50  $\mu\text{m}$  is used in the simulation. The circumferential distance between asperities centre is 120  $\mu\text{m}$  ( $1.7^\circ$ ).

The simulation stages adopted are as explained in Fig. 5.10. The model contains three stages in the simulation procedure: determination of the contact pressure, calculation of the wear based on Archard's wear equation and updating of the geometry. The wear simulation lasts until the sliding distance ( $S_{max}$ ) is obtained.

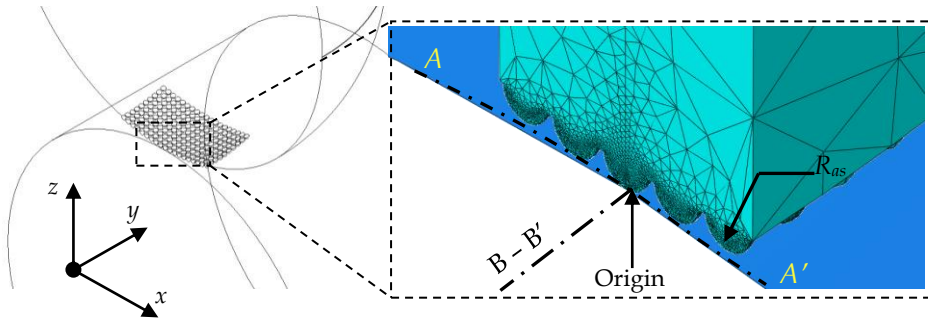


**Figure 5.17:** Two-disc contact where an artificial rough surface is modelled on the upper disc surface. The zoom-in view depicts the contact between the rough surface and the smooth lower surface and the mesh refinement near the contact area. The axis-symmetrical line is denoted as A-A'.

### 5.3.2 Contact pressure and wear depth of rough surface

The initial contact between the rough sphere and the smooth cylinder when loading the system initially occurs on asperities on the axis-symmetrical line of the disc (line A-A'). Then, as the contact load increases and reaches, in this case, 100 N, other asperities in perpendicular direction of line A-A' come in contact, marked with number 4 and 5 as illustrated in Fig. 5.18 and Fig. 5.19. It shows that the nominal contact area becomes larger and the number of contacting asperities increases as the contact load increases.

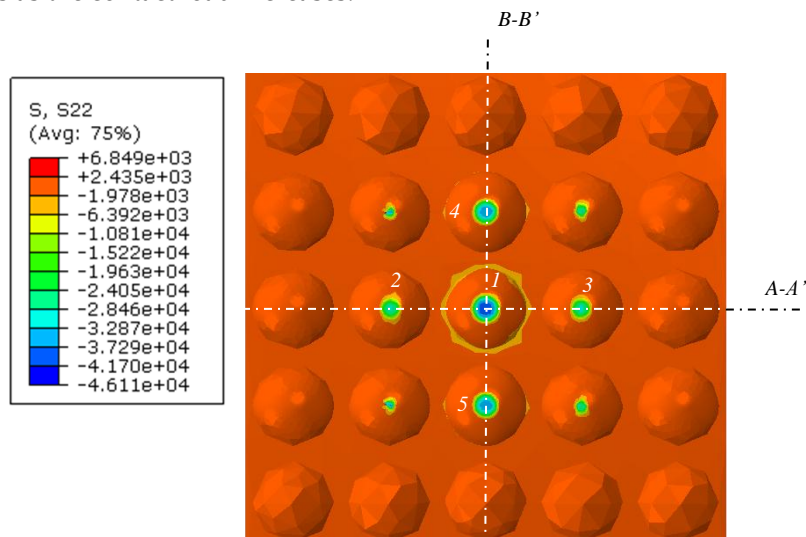


**Figure 5.18:** Contact area between the rough disc and smooth disc. The contact pressures are given in MPa.

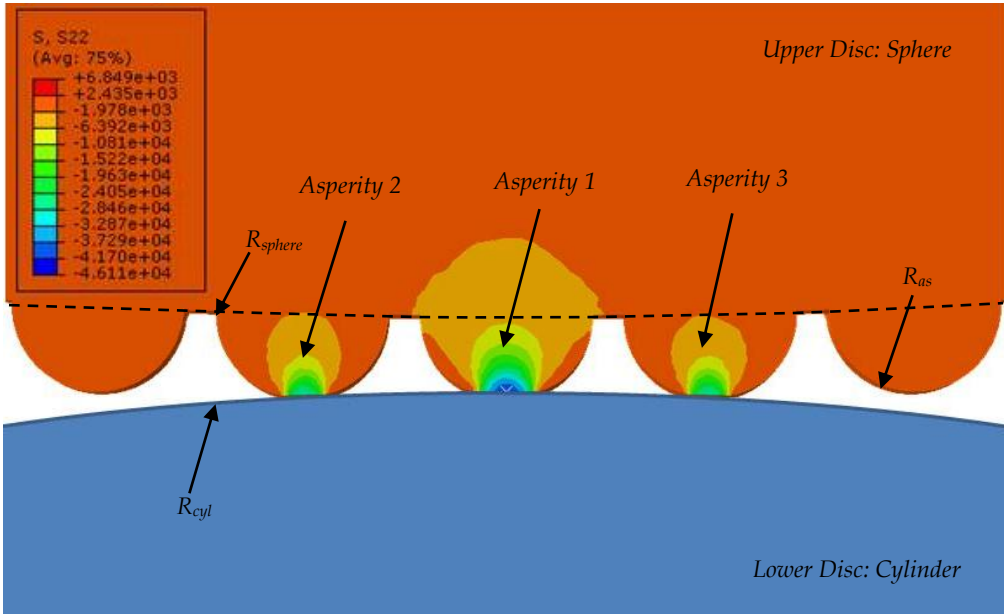


**Figure 5.19:** Cross-sectional view of the twin disc system on A-A'.

The evolution of the average contact pressure of the asperities with increasing number of rotations is shown in Fig. 5.20. Average contact pressures of asperity 1, 2 and 3, located along A-A' line, are assumed to have similar value. There is a moment when asperity 2 and asperity 3 have a similar position to asperity 1 in Fig. 5.19.

Asperity 4 and asperity 5 have the same distance to line A-A' and are assumed to have similar average contact pressure. Initially the contact pressures of asperity 1, 2 and 3 are higher than asperity 4 and 5. As the number of rotations increases, the contact pressures of asperity 1, 2 and 3 decrease and are finally lower than the average contact pressure in asperity 4 and 5. Then, the contact pressures of the asperities are stabilized after 1600 rotations. The contact pressure reaches a stabilized value, which indicates the end of the running-in phase and the beginning of the steady-state phase.

The local wear depth of the rough surface,  $h^w$ , is calculated by considering the contacting asperity. The asperity contact pressures distribution is put in the Archard wear equation to calculate the local wear depth. Figure 5.21 depicts the wear depth of the asperity 1-5 as a function of the number of rotations of the lower disc. The highest wear depth is found for asperity 1, 2 and 3, where initially the highest contact pressure was located. The wear depth of asperity 4 and 5 is the same because these asperities have the same contact pressure evolution.

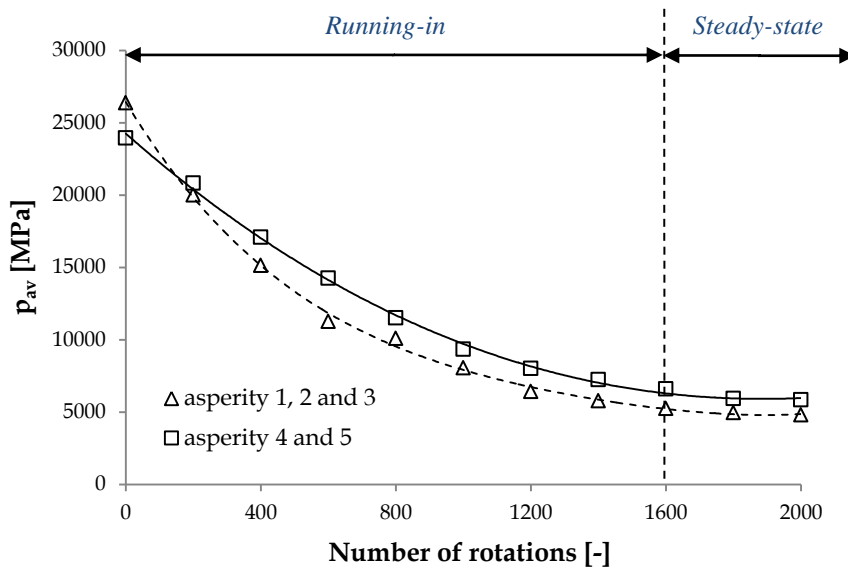


**Figure 5.20:** Calculated contact pressure evolution of asperity 1-5 as a function of the number of rotations.

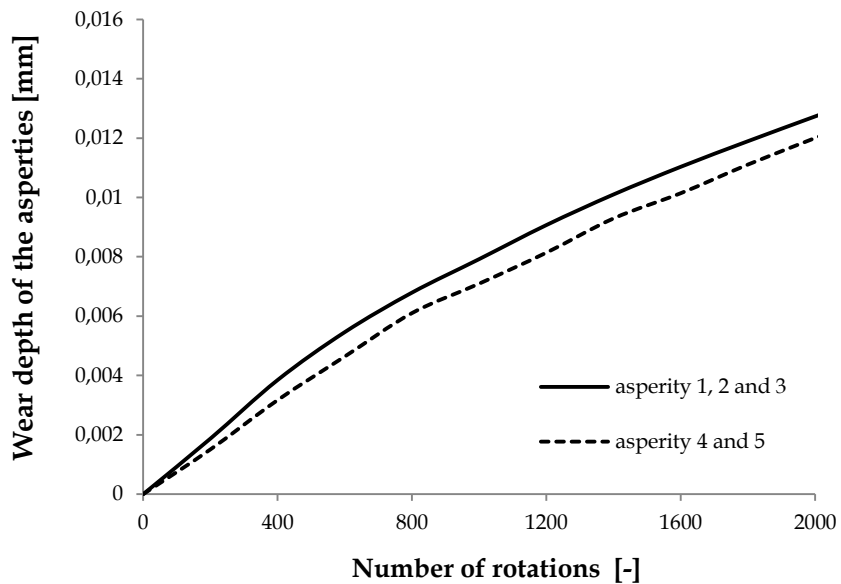


**Figure 5.21:** The wear depth evolution of asperity 1-5 as the sliding distance (number of revolutions) increases.

## 5.4 Running-in of real rough rolling-sliding contact

### 5.4.1 Experiment

In his experiment of running-in of repeated rolling contacts, Jamari [16] reported the presence of slip in his experiments and found that the surface topographical change of the rough surface is the result of plastic deformation and mild wear. FE simulation of the present model for running-in of rolling-sliding contact is conducted with respect to Jamari's experiment [16].

A silicon carbide ceramic ball ( $H = 28$  GPa,  $E = 430$  GPa,  $\sigma_Y = 1.18$  GPa and  $\nu = 0.17$ ) with a diameter of 6.35 mm was in contact with a mild steel flat rough surface ( $H = 3.55$  GPa,  $E = 210$  GPa and  $\nu = 0.3$ ) in a ball-on-disc experimental set-up. With maintaining the contact load ( $F_N = 2.5$  N), the disc is rotated. The sum velocity of the experiment is about 7 mm/s, with an average slip of 2.98% and the system is unlubricated. After each rotation of the disc, the disc is stopped and then the surface roughness is measured. The change of the topographical surface of the mild steel is reported.

### 5.4.2 Validation of FE simulation

The method for generating the mild steel rough surface, as used by Jamari [16], is described in Appendix C. The comparison between the experiment [16] and the present FE model for  $n = 10$  and  $n = 40$  cycles is depicted in Fig. 5.22.

The result shows that the finite element simulation is in reasonably good agreement with the experimental result in predicting the surface topographical change of the mild steel surface. Difficulties in matching and stitching of the initial and deformed surface for the finite element surface model and the experimental surface are found in this case. As a result, the initial geometry of the finite element simulation does not precisely match with the experimental surface.

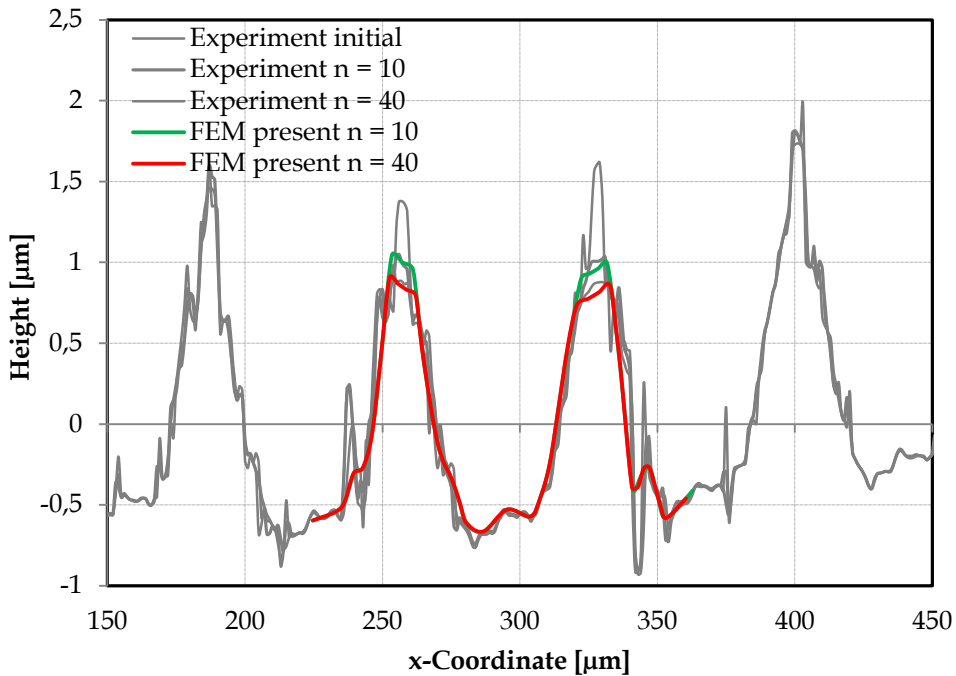


**Figure 5.22:** Validation of FE simulation of the present model with Jamari's experiment [16] for running-in of rolling-sliding contact (profile is perpendicular to the rolling direction).

## 5.5 Running-in of lubricated rolling-sliding contacts

In the previous section the effect of wear on the contact pressure during the running-in phase is shown; however, hydrodynamic effects, i.e. lubrication, were neglected in the previous discussion.

Wang and his co-workers [17-19] used the partial elasto-hydrodynamic lubrication (PEHL) model in determining the lubrication film between the contacting surfaces during the running-in phase of rolling-sliding contacts. In that model a statistical parameter of the rough surface is used, represented by the arithmetic average of the surface roughness,  $R_a$ . The development of the  $R_a$  in the transient running-in regime was reported, in which some parameters in rolling-sliding contact were varied.

Akbarzadeh and Khonsari [20] started their work in predicting running-in by using the elasto-hydrodynamic lubrication model. The load-sharing concept, i.e. the lubrication model, was combined with the asperity deformation model. The developed lubrication model for the mixed-lubrication regime is combined with the contact model of Zhao et al. [21] in order to predict the running-in phenomena.

Continuing their research, the effects of the initial surface roughness, surface topography, rolling-sliding velocity and contact load, during the running-in phase of a rolling-sliding contact, were reported in a recent paper [22]. An experimental set-up was employed to check their load-sharing model in the running-in phase by varying the hardness of the material and the slide-to-roll ratio. They observed a change in surface roughness, wear depth, coefficient of friction and surface temperature when the input parameters were varied. In this section, numerical simulations in determining the running-in phase of lubricated rolling-sliding contacts on asperity level are conducted by following the work of Akbarzadeh and Khosari [20].

### 5.5.1 Computational model and procedures

In this research, the rolling-sliding contact consists of two cylindrical rollers. The dimensions of the rollers, the operating conditions, and the lubricant properties are taken from Wang et al. [19] and listed in Table 5.3.

Table 5.3: The operating conditions for running-in of a lubricated rolling-sliding contact simulation based on the experiments of Wang et al. [19].

<b>Dimensions and Operating Condition</b>	<b>Case 1</b>	<b>Case 2</b>
Radius of larger roller	43 mm	43 mm
Radius of smaller roller	17 mm	17 mm
Velocity of larger roller	<i>0.8 m/s</i>	<i>0.7 m/s</i>
Velocity of smaller roller	<i>1.2 m/s</i>	<i>1.3 m/s</i>
Applied force	40 N	40 N
Lubricant viscosity	0.0283 Pa.s	0.0283 Pa.s
Pressure-viscosity index (Roelands)	0.6	0.6
Average roughness of larger roller	<i>0.58 <math>\mu\text{m}</math></i>	<i>1.27 <math>\mu\text{m}</math></i>
Average roughness of smaller roller	0.1 $\mu\text{m}$	0.1 $\mu\text{m}$
Hertzian pressure	0.22 GPa	0.22 GPa
Modulus of elasticity of each roller	230 GPa	230 GPa
Poisson's ratio of each roller	0.3	0.3
Dry wear coefficient	0.0003	0.0003
Asperity-asperity friction coefficient	0.12	0.12

Akbarzadeh and Khonsari [20] checked the load-sharing concept by comparing their results with the work of Wang et al. [19]. Two cases of simulations are prepared, where the distinction between these simulations lies in the initial surface roughness and rolling velocity of the two contacting bodies.



The simulation procedure is given in the flow chart of Fig. 5.26. The equations used in the flow chart were reviewed briefly in Section 2.5.5. The change of the surface roughness,  $R_{ar}$ , was calculated after the wear volume calculation.

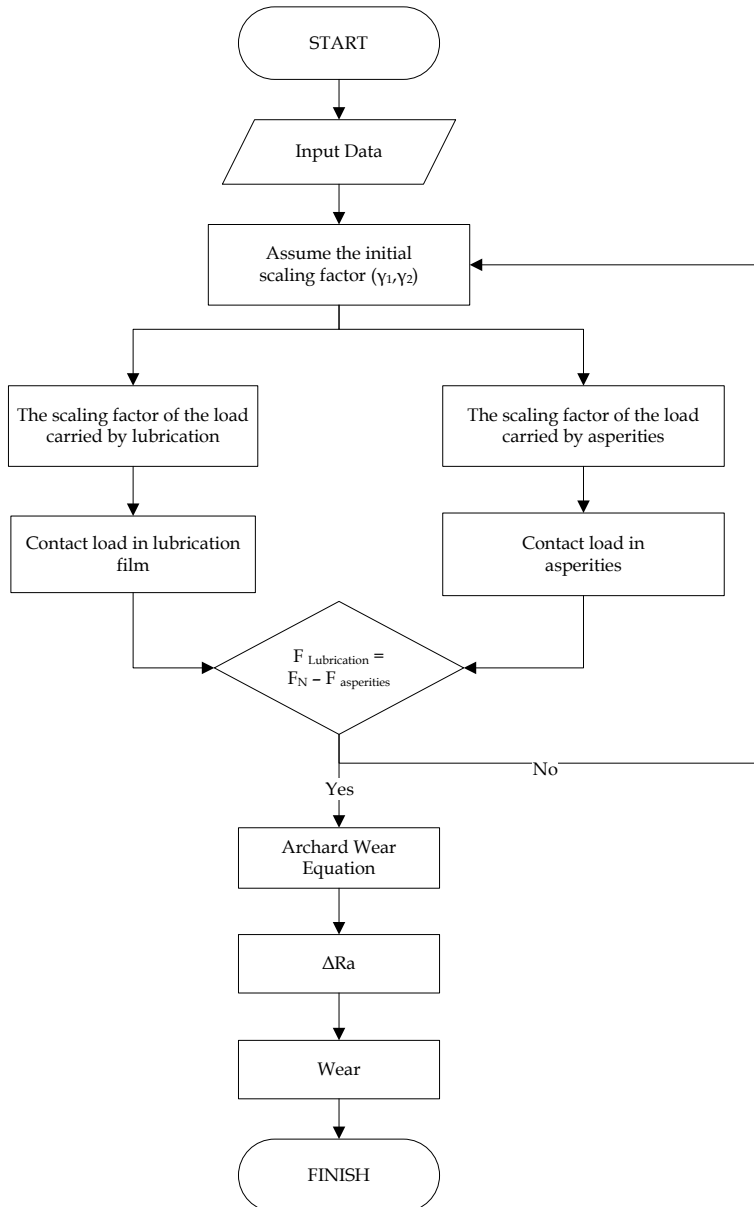


**Figure 5.23:** Flow chart on wear prediction during running-in of lubricated rolling-sliding contacts.

## 5.5.2 Results and discussions

The results are plotted in graphs as a function of time and compared with the results of Akbarzadeh and Khonsari [17] as seen in Fig. 5.24-5.25.

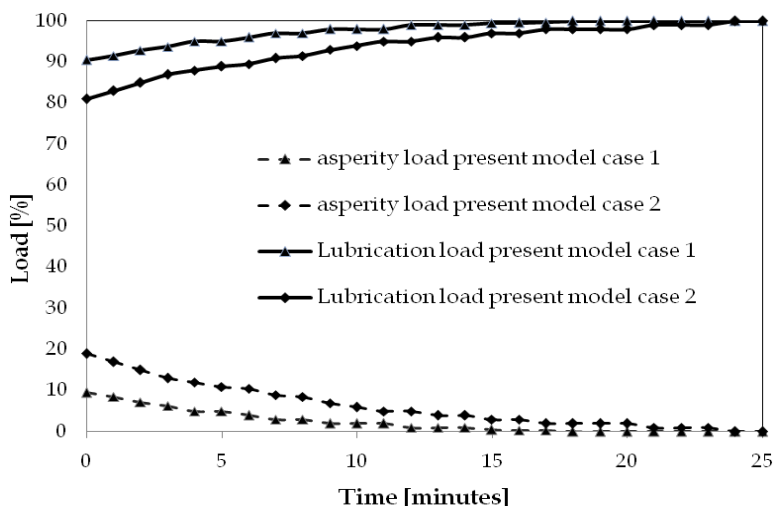


**Figure 5.24:** Comparison of the percentage of the load carried by asperities and lubricant film in time during running-in of rolling-sliding contacts. The operating conditions for case 1 and 2 are given in Table 5.3.

Figure 5.24 depicts the comparison of the percentage of the load carried by asperities and lubricant film in time during running-in of a rolling-sliding contact. Initially, the load carried by asperities in the first case is smaller than for the second case due to the initial smoother surface. At the start of the first case, the asperities carry around 10% of the load and the lubricant film carries around 90 % of the load, whereas in the second case the asperities carry around 20% of the load and the lubricant film carries around 80% of the load.

As the time of the rolling-sliding contact increases, the asperities are truncated due to normal deformation and wear, the surface becomes smoother and the lubrication performance increases. As a result, the load carried by the asperities decreases as the load carried by the lubricant increases. The smoothing of the surface can be seen in Fig. 5.25 where a lower surface roughness ( $R_a$ ) for the first and second case is obtained due to the running-in of the rolling-sliding contact.

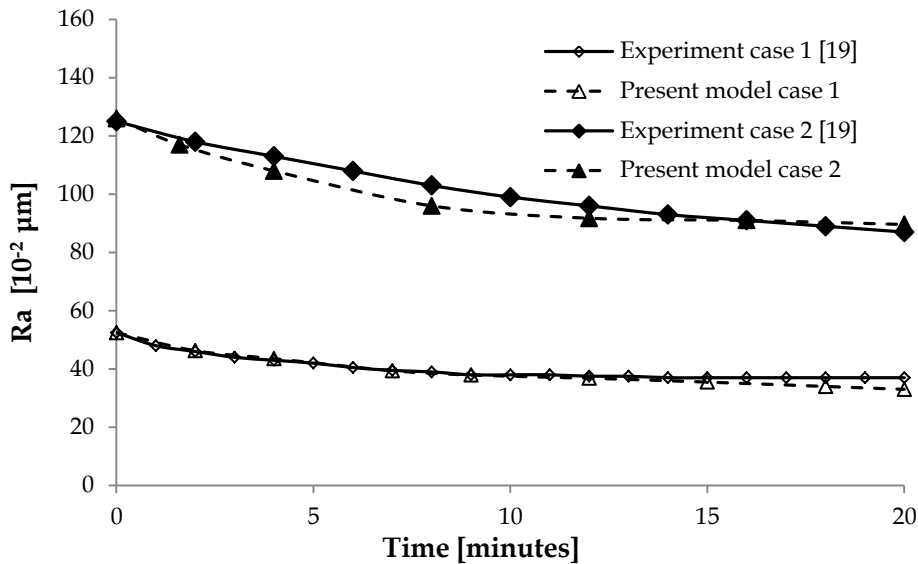


**Figure 5.25:** Evolution of the surface roughness ( $R_a$ ) as a function of time for the experimental cases 1 and 2 of Table 5.3.

## 5.6 Concluding remarks

This chapter described the running-in of rolling-sliding contacts on macroscopic and microscopic level.

- 1) On macro-scale, the geometrical change of the contacting components due to wear is predicted using the present FEM model, combined with the Archard wear equation, and has been compared with results from the literature, with which they agree very well. With the models, the effect of contact load, slip, and rolling velocity on the running-in of rolling-sliding contacts was shown.
- 2) On micro-scale, the present FEM based wear model is used to perform simulations in which an artificial rough hemisphere is in rolling-sliding contact with a smooth cylinder. Next, the running-in of real rough surfaces was simulated using a measured surface, and the results show reasonably good agreement between the FEM prediction and the experiment results.

Further, the change of a rough surface, represented by an arithmetic average surface roughness,  $R_a$ , is predicted for lubricated rolling-sliding contacts using the load-sharing concept. The results obtained are in good agreement with experimental results.

The transition between the running-in phase to the steady-state phase of a rolling-sliding contact cannot be captured with a single parameter.

## References

- [1] Olofsson, U., Andersson, S. and Björklund, S., 2000, "Simulation of mild wear in boundary lubricated spherical roller thrust bearings," *Wear*, 241, pp. 180-185.
- [2] Hugnell, A.B.-J., 1995, *Simulation of the Dynamics and Wear in a Cam-follower Contact*, Ph.D. Thesis, KTH Royal Institute of Technology, Stockholm, Sweden.
- [3] Flodin, A., 2000, *Wear of Spur and Helical Gears*, Ph.D. Thesis, KTH Royal Institute of Technology, Stockholm, Sweden.
- [4] Hegadekatte, V., Hilgert, J., Kraft, O. and Huber, N., 2010, "Multi time scale simulations for wear prediction in micro-gears," *Wear*, 268 pp. 316-324.
- [5] Blau, P.J., 1989, *Friction and Wear Transitions of Materials: Break-in, Run-in, Wear-in*, Noyes Publications, Park Ridge, NJ, USA.
- [6] Shirong, G. and Gouan, C., 1999, "Fractal prediction models of sliding wear during the running-in process," *Wear*, 231, pp. 249-255.
- [7] Zhu, H., Ge, S., Cao, X. and Tang W., 2007, "The change of fractal dimension of frictional signals in the running-in wear process," *Wear*, 263, pp. 1502-1507.
- [8] Sugimura, J., Kimura, Y. and Amino, K., 1987, "Analysis of the topography changes due to wear-geometry of the running-in process," *JSLE*, 31(11), pp. 813-820.
- [9] Jeng, Y.R. and Gao, C.-C., 2000, "Changes of surface topography during wear for surfaces with different height distributions," *Tribology Transactions*, 43, pp. 749-757.
- [10] Jeng, Y.R., Lin, Z.W. and Shyu, S.H., 2004, "Changes of surface topography during running-in process," *ASME Journal of Tribology*, 126, pp. 620 - 625.
- [11] Hsu, S.M., Munro, R.G., Shen, M.C. and Gate, R.S., 2005, "Boundary lubricated wear," In: *Wear-Materials, Mechanisms & Practice*, G.W. Stachowiak (Ed.), John Wiley & Sons Inc., London, UK, pp. 37-69.
- [12] Argatov, I.L. and Fadin, Y.A., 2011, "A macro-scale approximation for the running-in period," *Tribologi Letters*, 42, pp. 311-317.
- [13] Hegadekatte, V., Kurzenhauser, S., Huber, N. and Kraft, O., 2008, "A predictive modeling scheme for wear in tribometers," *Tribology International*, 41, pp. 1020-1031.
- [14] Rodríguez-Tembleque, L., Abascal, R. and Aliabadi, M.H., 2010, "A boundary element formulation for wear modeling on 3D contact and rolling-contact problems," *International Journal of Solids and Structures*, 47, pp. 2600-2612.

- [15] Andersson, S., 2010, "Wear simulation," In: *Advanced Knowledge Application in Practice*, Igor Fuerstner (Ed.), Intech, Rijeka, Croatia, pp. 15-36.
- [16] Jamari, J., 2006, *Running-in of Rolling Contacts*, PhD Thesis, University of Twente, Enschede, The Netherlands.
- [17] Wang, W. and Wong, P.L., 2000, "Wear volume determination during running-in for PEHL contact," *Tribology International*, 33, pp. 501-506.
- [18] Wang, W., Wong, P.L. and Zhang, Z., 2000, "Experimental study of the real time change in surface roughness during running-in for PEHL contact," *Wear*, 244, pp. 140-146.
- [19] Wang, W., Wong, P.L. and Guo, F., 2004, "Application of partial elastohydrodynamic lubrication analysis in dynamic wear study for running-in," *Wear*, 257, pp. 823-832.
- [20] Akbarzadeh, S. and Khonsari, M.M., 2010, "On the prediction of running-in behavior in mixed-lubrication line contact," *ASME Journal of Tribology*, 132, pp. 1-11.
- [21] Zhao, Y., Maietta, D.M. and Chang, L., 2000, "An asperity microcontact model incorporating the transition from elastic deformation to fully plastic flow," *ASME Journal of Tribology*, 122, pp. 86-93.
- [22] Akbarzadeh, S. and Khonsari, M.M., 2011, "Experimental and theoretical investigation of running-in," *Tribology International*, 44, pp. 92-100.





CHAPTER  
6

## Conclusions and Recommendations

---

This chapter summarises the main conclusions of the results obtained in this research on running-in of rolling, sliding and rolling-sliding contacts. After a discussion on several topics, which can be researched with the developed running-in model, recommendations are given for future research.

### 6.1 Conclusions

#### Chapter 2: Literature

- Modelling running-in wear is done analytically and numerically. The parameters studied mainly focus on material loss and wear depth, change in surface roughness and the coefficient of friction. The transition of the running-in phase to the steady-state phase is determined using these parameters.
- Regarding the running-in of rolling contacts, it is shown that plastic deformation in normal direction is the main cause of the topographical changes of a rough surface.
- For sliding contacts, existing models on running-in are based on the well-known Archard's wear equation, where the contact pressure is calculated by using elastic-plastic contact models.
- Running-in of rolling-sliding contacts is governed by a combination of the effects in rolling and in sliding contacts.
- Existing models that predict the change of the surface topography and wear during the running-in phase are most frequently based on a statistical approach. A deterministic rough surface approach is hardly used.

**Chapter 3: Running-in of Rolling Contacts**

- A study regarding the topographical change due to running-in of rolling contacts was presented in this chapter by applying the finite element (FE) method to rolling contacts on rough surfaces. Comparison of the simulations and the experimental results did show good agreement.
- The equivalent contact stress distribution and the equivalent residual stress due to elastic-plastic deformation during repeated overrolling demonstrate a transition to steady-state behaviour. In the case of a rolling contact, ignoring slip and friction, it is shown that the surface topographical change during running-in is mainly caused by plastic deformation in normal direction. The transition from the running-in phase to the steady-state phase is governed by the change of plastic to elastic deformation behaviour on roughness level.

**Chapter 4: Running-in of Sliding Contacts**

- In the model for running-in of sliding contacts, the change in surface topography is addressed as regards wear and is predicted by using Archard's wear law.
- Running-in FE simulations for predicting macroscopic wear of contacting components show that the evolution of the contact pressure appears to be a parameter that indicates the transition between the running-in and steady-state phase.
- The FE model showed its capability to predict the microscopic wear for sliding contact with an artificial rough surface as well as of a real rough surface.

**Chapter 5: Running-in of Rolling-sliding Contacts**

- The finite element simulation has been compared with existing wear models and experiments; good agreement is found.
- Microscopic wear has been calculated with the FE model and compared with experiments and reasonably good agreement is found.
- The FE model showed its capability to predict the microscopic wear of an artificial rough surface as well as of a real rough surface for rolling-sliding (lubricated) contacts.

**6.2 Discussions and direction for further research****6.2.1 Abrasion**

With the developed model, which is a combination of the finite element analysis and Archard's wear equation, one is able to study the change in surface topography. In many applications the abrasive wear mechanism takes place. The



running-in of systems in which abrasion takes place, besides the mild corrosive wear, may differ significantly.

Based on a theoretical investigation of slip-lines by Challen and Oxley [1], Kato and co-workers developed a wear mode map distinguishing three wear modes: ploughing, wedge formation and cutting [2], see Fig. 6.1.

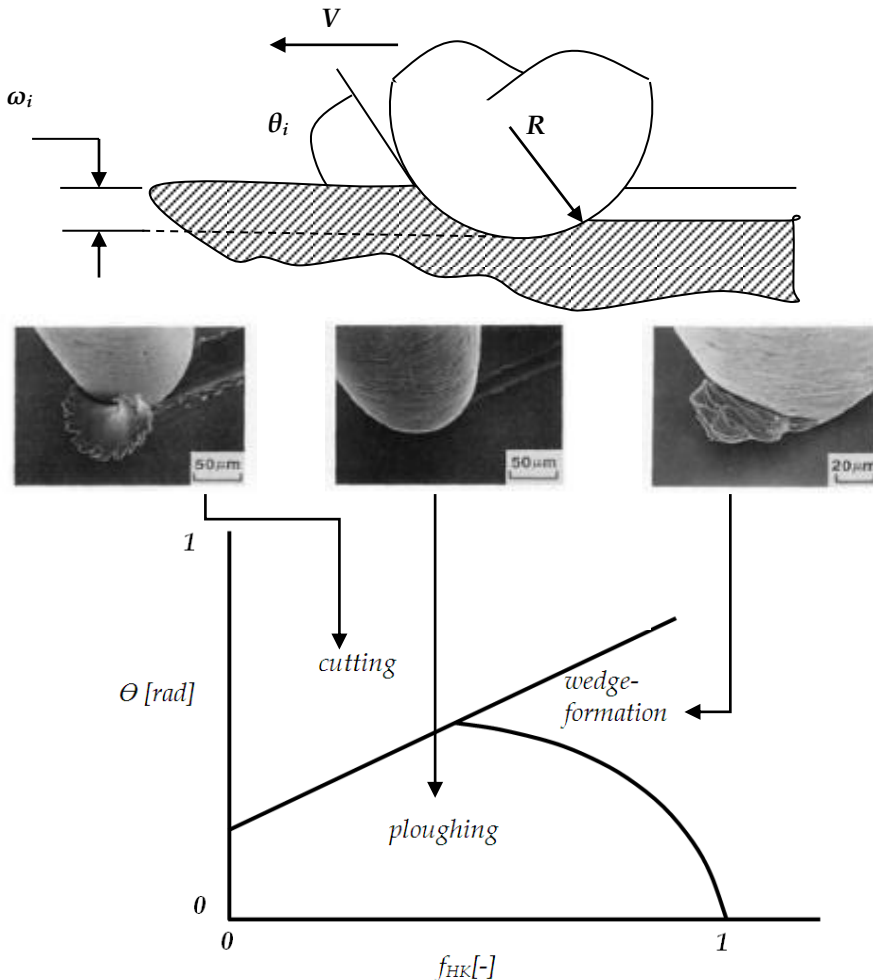


**Figure 6.1:** The wear mode diagram, after de Rooij [3].

Abrasive wear, three mechanisms observed using a scanning electron microscope:  
 (a) Cutting, (b) Ploughing and (c) Wedge formation.

De Rooij [3] uses the attack angle of the sliding asperity,  $\theta$ , and the dimensionless shear strength,  $f_{HK}$  to visualize the wear regimes. The dimensionless shear strength,  $f_{HK}$  was calculated as:  $f_{HK} = \tau/k$  where  $k$  is the shear strength of the softest contact partner and  $\tau$  is the shear strength of the interface, similar to Childs [4].

The regime of interest is the ploughing regime because in the other regimes the wear is high and not of interest for mechanical systems, unless one is interested in machining. In order to study the effect of ploughing on the change of surface topography, an initial finite element simulation has been conducted in which a rigid indenter slides over a deformable flat surface. Figure 6.2 depicts a sliding rigid indenter ( $R = 2.5$  mm) over a flat surface, made of AA 7475 ( $E = 71.7$  GPa,  $\nu = 0.33$ ,  $\sigma_Y = 460$  MPa) for a certain distance. The deformed surface and the residual von Mises stress are depicted in Fig. 6.3. Combining this type of calculation on micro level with the rolling-sliding contact calculation presented in this thesis one is able to predict the change in surface topography as a function of sliding distance.

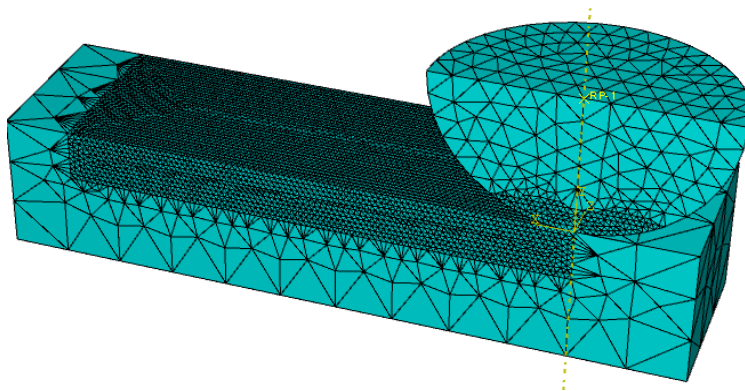


**Figure 6.2:** Contact model of a hemisphere on a flat surface in finite element simulation of ploughing wear.

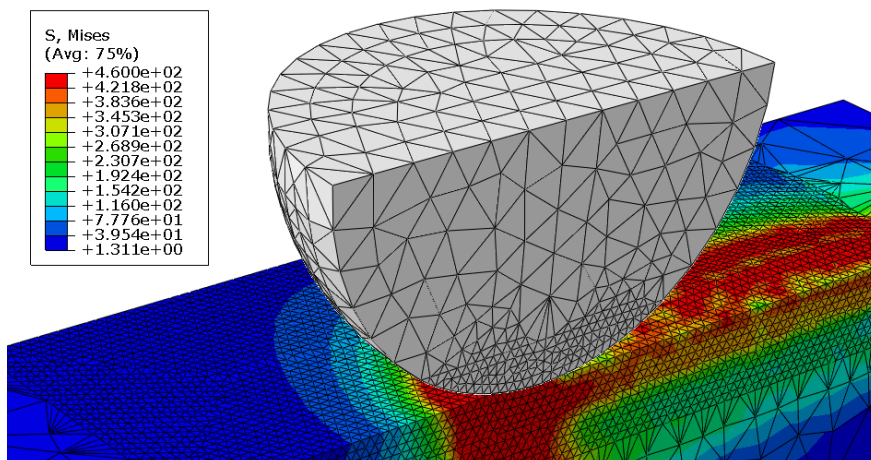


**Figure 6.3:** Stress distribution (stresses given in MPA) in finite element simulation of ploughing wear during sliding contact.

### 6.2.2 Specific wear rate

In this thesis the local wear is calculated using Archard's wear equation, in which the wear rate is taken from experiments and is constant. Recently, Bosman [5] conducted research in which the wear rate in the mild corrosive wear regime is predicted on the basis of the operational conditions normal load,  $F$ , and sliding velocity,  $v$ , see Fig. 6.4. If the present FE model is combined with such a model, the wear rate can be adopted to local conditions.

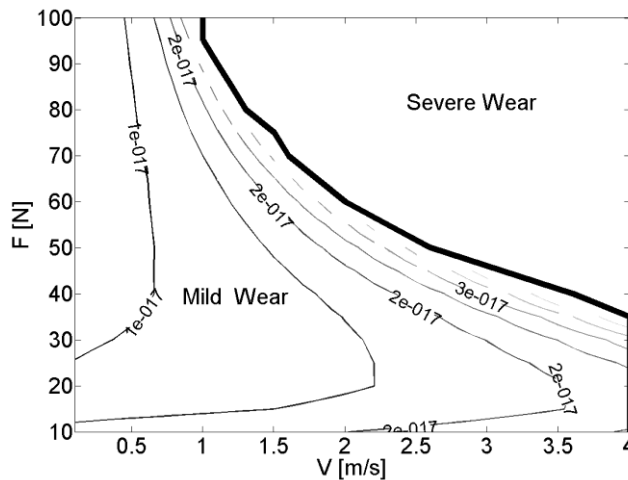


**Figure 6.4:** Transition diagram mild to severe wear. Iso-lines in the mild wear regime are lines of constant wear rates [ $\text{m}^3/\text{Nm}$ ], after Bosman [5].

### References

- [1] Challen, J.M. and Oxley, P.L.B., 1979, "An explanation of the different regimes of friction and wear using asperity deformation models," *Wear*, 53, pp. 229-243.
- [2] Hokkirigawa, K. and Kato, K., 1988, "An experimental and theoretical investigation of ploughing, cutting, and wedge formation during abrasive wear," *Tribology International*, 21, pp. 51-57.
- [3] de Rooij, M.B., 2005, *Tribological Aspect of Unlubricated Deepdrawing Processes*, PhD Thesis, University of Twente, Enschede, The Netherlands.
- [4] Childs, T.H.C., 1988, "The mapping of metallic sliding wear," *Proc. Instn. Mech. Engrs. C*, 202, pp. 379-395.
- [5] Bosman, R., 2011, *Mild Microscopic Wear Modeling in the Boundary Lubrication Regime*, PhD Thesis, University of Twente, Enschede, The Netherlands.





## Measurement of Plastic Deformation of Static Contact between Hemispheres with Different Radii

---

The investigation of the plastic deformation of the static contact between hemispheres with different radii was conducted experimentally and numerically using finite element simulations.

### A.1 Experimental investigation

The experiments were conducted using a universal tensile tester, as shown in Fig. A1. The applied loads in these experiments were 8000 N and 11000 N.

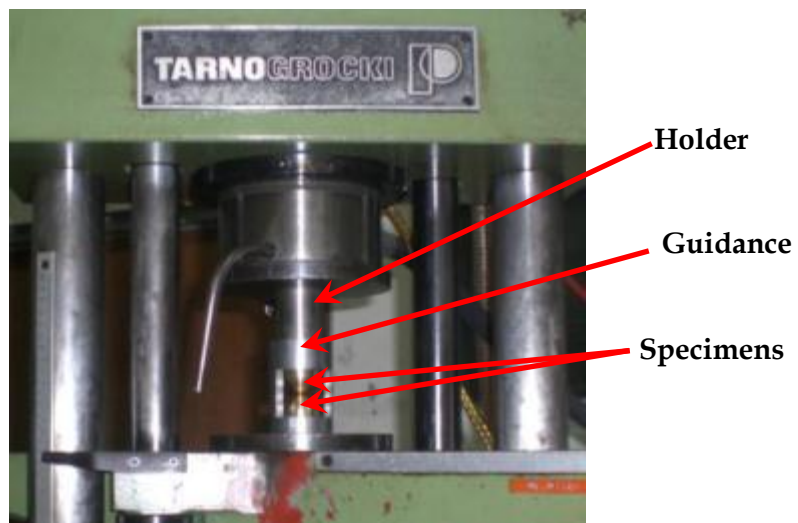


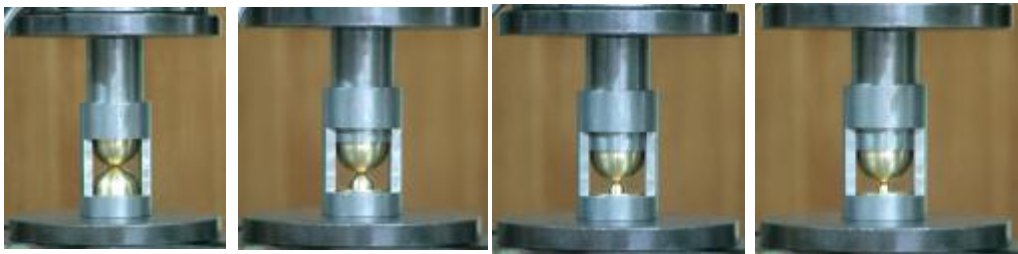
**Figure A1:** The arrangement of the specimens in the tensile tester.

The hemisphere specimens were made from brass with mechanical properties  $H = 0.31$  GPa,  $E = 96$  GPa, and  $\nu = 0.3$  respectively. The radius of the hemisphere was varied as follows: 17.5, 8.75, 5.84, 4.38, 3.5, 2.92 and 2.5 mm. The hemisphere specimens and the couples formed are depicted in Figs. A2 and A3.

After the experiments, the plastic deformation of a hemisphere specimen was measured using a micrometre. The measurement process can be seen in Fig. A4. Then the plastic deformation of each hemisphere was recorded and presented in a table and a curve as shown in Fig. 3.5(a) and (b), for a load of 8000 N and 11000 N, respectively.



**Figure A2:** Hemisphere specimens with different radii.



**1:1**

**2:1**

**3:1**

**4:1**



**5:1**

**6:1**

**7:1**

**Figure A3:** Hemispherical specimen couples.



**Figure A4:** Measuring the plastic deformation using a micrometre.

## A.2 Numerical investigation

The numerical investigation employs finite element software, ABAQUS, where the contact model and the refined mesh is shown in Fig. A5 (a) and (b), respectively.

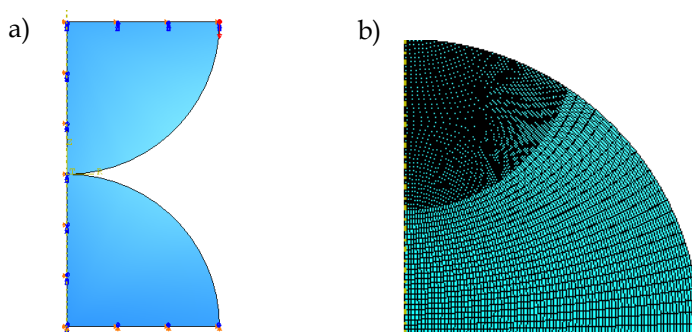


**Figure A5:** (a) contact model and (b) the refined mesh of the hemisphere.

The dimensions, the ratio of the radii, the contact load and the mechanical properties used are given in the previous section. Single static contact was applied on the couples and the contact load is positioned on the upper hemisphere. An FE

simulation is depicted in Fig. A6. The plastic deformation was determined as shown in Fig. A7. The results of the plastic deformation are presented in Fig. 3.5 (a) and (b).

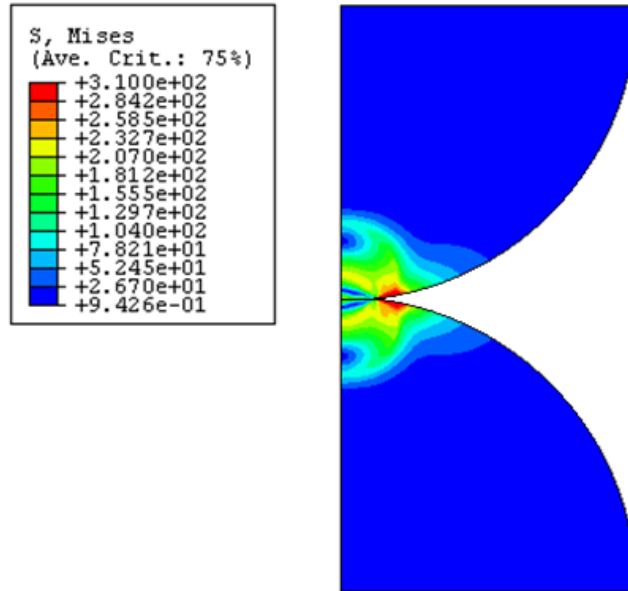


**Figure A6:** The results of the finite element analysis of static contact, stress values are given in MPa.

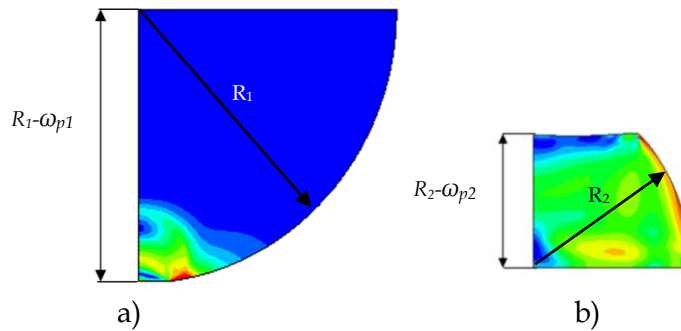


**Figure A7:** The measurement of the plastic deformation for the upper hemisphere (a) and lower hemisphere (b).



## Appendix B

# Modelling and Validation of the Real Rough Surface Contact Using Finite Element Analysis

A method for modelling a real rough surface using finite element analysis (FEA) is proposed. Figure B1 depicts the three steps of the real rough surface modelling in FEA. First, the real rough surface topography is measured by means of, for instance, an interference microscope, as shown in Fig. B2. The height  $h(x, y)$  of the surface topography contains a collection of asperities in the form of coordinate nodals.

In the second step, the coordinate nodals are processed by using CAD software. An automatic approach is used in connecting the nodes in the CAD software for generating the rough surface. A substrate is constructed below the rough surface to model the thickness of the rough surface specimen. The rough surface model is saved using the Initial Graphics Exchange Specification (IGES) format.

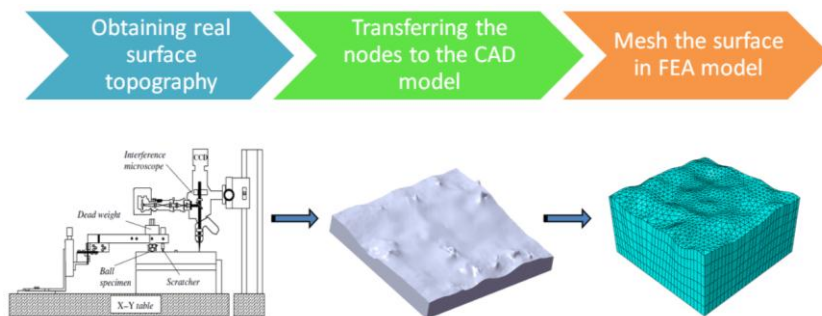


**Figure B1:** The proposed method in determining a real rough surface for finite element analysis.

In the third step, the rough surface model in IGES format is opened in Computer Aided Engineering (CAE) software and meshed to divide the surface into finite elements.



**Figure B2:** Interference microscope (Micromap) for measuring the topography of a real rough surface.

In order to check the accuracy of the transferring process of the surface topography from the real rough surface to the FE model, the results of an experiment and the FEA of the normal static contact are compared. The work of Jamari [1] is used to make the comparison with the present real rough surface FE model.

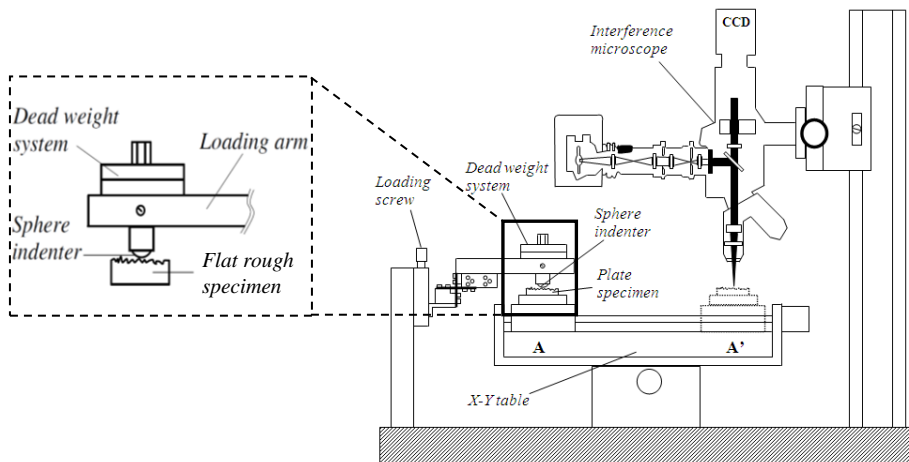


**Figure B3.** The measurement set-up for conducting normal indentation and measuring the initial and deformed real rough surface, after Jamari [1].

Jamari [1] reported experiments of the deterministic contact of a rough surface by employing normal indentation of a hard and smooth hemisphere on a deformable nominally rough flat. A hardened steel sphere ( $H = 7.5$  GPa,  $E = 210$  GPa and  $\nu = 0.3$ ) with a diameter of 10 mm was used as hard indenter specimen. An aluminium rough plate ( $H = 0.24$  GPa,  $E = 75.2$  GPa, and  $\nu = 0.34$ ) was used as deformable flat. The set-up of the experiments is depicted in Fig. B3. A contact load of 1 N was applied to the loading arm (as shown in the zoom window in Fig. B3). The normal indentation to the rough surface specimen takes place at position A. The plastic deformation is then captured, after the specimen is translated to position A', using the interference microscope.

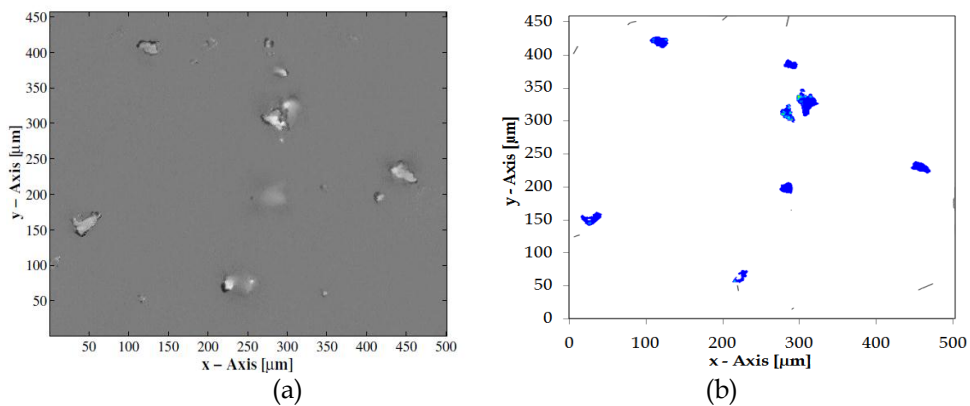


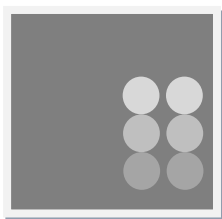
**Figure B4.** The comparison of the measured and calculated contact area: measured contact area [1] (a), and contact area prediction using finite element analysis (b).

In the present validation, the nodal coordinate of the undeformed rough surface specimen is transferred to the FE Software, as described before, to perform the finite element simulation. The contact area of the finite element simulation is captured and compared with the experimental results [1], as depicted in Fig. B4 (a and b). Comparing the experimental results and the finite element analysis shows that a good agreement is found.

## References

- [1] Jamari, 2006, *Running-in of Rolling Contacts*, Ph.D. Thesis, University of Twente, Enschede, The Netherlands.





## List of Publications

---

### Journal papers

Ismail, R., Saputra, E., Tauviqirrahman, M., Jamari, J. and Schipper, D.J., 2013 "Modeling of Repeated Rolling Contact on Rough Surface: Surface Topographical Change," *Advanced Materials Science and Technology*, accepted.

Ismail, R., Tauviqirrahman, M., Jamari and Schipper, D.J., 2013, "A Finite Element Analysis of Running-in of a Rigid Ball Rolling on a Rough Surface", *Tribology International*, submitted.

Ismail, R., Tauviqirrahman, M., Jamari and Schipper, D.J., 2013, "A Systematic Finite Element Analysis to Characterize Running-in of Sliding Contacts", *Wear*, submitted.

Ismail, R., Tauviqirrahman, M., Jamari and Schipper, D.J., 2013, "Finite element analysis of wear prediction in rolling-sliding contacts," *Proceedings of the IMechE, Part J: Journal of Engineering Tribology*, submitted.

### Book chapter

Ismail, R., Tauviqirrahman, M., Jamari and Schipper, D.J., 2011, "Topographical Change of Engineering Surface Due to Running-in of Rolling Contacts," in *New Tribological Way* (Ed: Ghrib, T.), InTech, Vienna, Austria, pp. 131-152.

**International proceedings**

Ismail, R., Tauviqirrahman, M., Saputra, E., Jamari, J. and Schipper, D.J., 2013 "Modeling of repeated rolling contact of rigid ball on rough surface: residual stress and plastic strain analysis," *Procedia Engineering*, submitted.

Ismail, R., Tauviqirrahman, M., Jamari and Schipper, D.J., 2011 "The Observation of The Steady State Phase on Rolling Contact Using Finite Element Analysis," *American Institute of Physics (AIP) Conference Proceeding*, vol. 1415, pp. 136-139.

Ismail, R., Tauviqirrahman, M., Jamari and Schipper, D.J., 2010, "Two-dimensional Finite Element Analysis on Running-in of Elastic-Plastic Rolling Contact", *American Institute of Physics (AIP) Conference Proceedings*, vol. 1325, pp. 190-193.

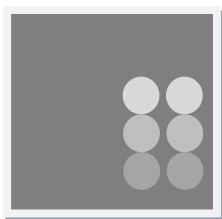
Ismail, R., Tauviqirrahman, M., Jamari and Schipper, D.J., 2009, "New Material Development for Surface Layer and Surface Technology in Tribology Science to Improve Energy Efficiency," *American Institute of Physics (AIP) Conference Proceedings*, vol. 1169, pp. 214-221.

**National proceedings**

Ismail, R., Tauviqirrahman, M., Jamari and Schipper, D.J., 2011, "Prediction of the Running-in Phase on Rolling-sliding Contact," *Proceeding of International Conference and Exhibition Sustainable Energy and Advanced Material (IC-SEAM), Surakarta, Indonesia*, pp. 304-311.

Ismail, R., Tauviqirrahman, M., Jamari and Schipper, D.J., 2011, "The Investigation of Ploughing Friction Coefficient: Analytical and Numerical Solution", *The International Conference on Natural Sciences (ICONS) 2011, Malang, Indonesia*, (Ed: Scheer, H.) pp. 95-101.

Ismail, R., Tauviqirrahman, M., Jamari and Schipper, D.J., 2010, "Elastic-plastic Deformation of a Rough Surface Due to Repeated Rolling Contact," *5<sup>th</sup> Kentingan Physics Forum (KPF) - The International Conference on Physics and Its Applications, Surakarta, Indonesia*, (Ed: Purnama, B.) pp. 49-52.



## Acknowledgement

---

Conducting any research is not possible without the help of other people, and in this respect my research is no exception. There is a long list of people who I want to express my sincere thanks to those who have contributed in accomplishing the research reported in this thesis. This thesis could not have been completed without their help and support, for which I am very grateful.

First of all, I am greatly indebted to my promoter and assistance promoter, Prof. Schipper and Dr. Jamari for the opportunity to conduct the research, as well as their dedication in guiding, supporting and encouraging during the entire PhD project. I would like to thank them for sharing their ideas and knowledge and also their generosity. They supported me throughout the whole process of my study, ranging from their brilliant inspirations, valuable comments/suggestions and abundant research supports which helped me to finish PhD project. I might not have survived my study and would not have finished my research without their help and support.

I would like to acknowledge the graduation committee members: G.P.M.R. Dewulf, D.J. Schipper, Jamari, L.A.M. van Dongen, T. Tinga, P. De Baets and R.P.B.J. Dollevoet, for reading my final thesis draft and subsequently giving me their valuable advice and suggestions to improve the quality of my thesis.

I am grateful to M. Tauviquirrahman for his big contribution in arranging the scientific results more nicely; for Eko Saputra and Fanni Fattah for their unlimited supports and enormous energy in collecting the simulation and numerical data; and all members and former members of Lab EDT Group, University of Diponegoro for their contribution to carry out my PhD research project: Pak Sugiyanto, Pak Budi Setiyana, Pak Muchammad, Pak Imam Syafaat, Fadely, Indra, Khafidh, Rachmat, Imam, Khoironi, Yanto, Handu, Apri, Kurniawan, Yudo, Tomi, Susetyo, Sumarjito, Zainal, Bambang Singgih, Arta, Sugeng, Adib, Iwan, Arden, Agus, Trisno and also the other (former) members of

Lab EDT Group whom I cannot name one by one. Without their support and contribution, I would found more difficulties in conducting my research.

I would also like to thank Siti Nur Hidayah and Belinda for their help with many administrative matters. I owe a special thanks to Adib for a nice design of my thesis cover.

And last, but certainly not least to my big families. I am greatly indebted to my father and mother for becoming my inspiration and motivation during my whole life; to my lovely wife Hanna Lestari and my lovely daughters: Nadha and Nora, for their invaluable love, patience, support and prayer during my busy days, months and years; for Helmy Ismail and Hanie Amalia for their unconditional love and supports; and also for my families in Lombok: Papi, Mami, Afif, Nanda and Tika for their prayers and never ending loves. Their presence always brings happiness and harmony in my life and gives me abundant energy to finish this research and get my diploma.